Thermally Efficient Linear Motor Analysis & Design

by

Michael Kevin Liebman

A.B., Physics (1996)
Princeton University

Submitted to the Department of Mechanical Engineering
in partial fulfillment of the requirements for the degree of

Master of Science in Mechanical Engineering

at the

MASSACHUSETTS INSTITUTE OF TECHNOLOGY

February 1998

Author .....

Department of Mechanical Engineering
January 16, 1998

Certified by .....

David L. Trumper
Rockwell International Asssociate Professor of Mechanical Engineering
Thesis Supervisor

Accepted by .....

Ain A. Sonin
Chairman, Departmental Committee on Graduate Students

Thermally Efficient Linear Motor Analysis & Design

by

Michael Kevin Liebman

Submitted to the Department of Mechanical Engineering
on January 16, 1998, in partial fulfillment of the
requirements for the degree of
Master of Science in Mechanical Engineering

Abstract

We present the analysis and design of a high force per unit volume linear motor for use in machine tools. The motor is the first to incorporate coils wound with separated end-turns so that each layer of a coil can be directly cooled. Oil flows through the gaps in the end-turns on both sides of a coil to remove heat. A current of 1.6 A causes a 100°C temperature rise in a free convection-cooled coil; it takes a current of 9.0 A to cause the same temperature rise with our cooling technique. Thus our design allows nearly 6 times higher force in steady state and dissipates 32 times as much heat. We also investigate a second cooling scheme where we insert a comb-shaped piece of copper into the separated end-turn coil. Thermal analyses corroborated by experimental results are presented for both techniques.

We describe the construction of a prototype synchronous linear motor consisting of a moving coil assembly in a U-shaped magnet channel. We derive magnetic field solutions and force relations for this linear motor. The motor has a force constant of 35.3 N/A_{rms} and a peak magnetic field of 0.75 T. At a force of 259 N, it dissipates 730 W with a peak current density of 3.47×10^7 A/m^2 in the wire. We implement a digital lead-lag controlled positioner driven by this linear motor with a 100 Hz crossover frequency.

Thesis Supervisor: David L. Trumper
Title: Rockwell International Asssociate Professor of Mechanical Engineering

Acknowledgments

I was extremely fortunate to have many brilliant and knowledgeable people help me in numerous aspects of this research. Most important was Professor David Trumper, my thesis advisor. He has guided me throughout this year and a half, pointing me in new directions all the time. His enthusiasm for the project has been highly contagious, and he was always a source of stimulating ideas.

I am grateful to Anwar Chitayat, Founder and CEO of Anorad Corporation, for meeting with me on many occasions. His experience in linear motors and his innovative ideas proved invaluable during the course of this research. Our partnership with Anorad not only provided funding for this research, but allowed me access to their knowledgeable staff and advanced manufacturing techniques.

I especially thank Fred Sommerhalter, R&D Engineer, Linear Motor Development at Anorad, for his numerous contributions to the project. He did a fabulous job machining the prototype motor parts and resolving a host of manufacturing challenges. His design ideas and practical wizardry were vital to this project's success.

Now that Won-jong Kim has graduated, I realize more than ever how much he helped me during my first year. He was always eager to speak with me and taught me a lot about motors and electromagnetics. I thank Fred Cote for making the MIT machine shop a pleasure to work in. He especially helped me fabricate the comb cooling prototype.

Pradeep Subrahmanyan was always available for questions and discussions. We took apart many motors together and often debated electromagnetics issues. His help with the controls was much appreciated. I learned something new from Paul Konkola every time we had a discussion comparing our two stages. I am also indebted to Steve Ludwick and David Ma for helping me with a wide variety of mechanical issues. I thank everyone in the Precision Motion Control Lab for their daily ideas, suggestions, and time-saving tips.

This research was funded by Anorad Corporation and a Starr Foundation Fellowship grant to the author.

For Mom, Dad, and Judith

Contents

List of Figures

List of Tables

Chapter 1

Introduction

This thesis presents the design of high power density linear motors. We achieve high power density by developing advanced coil cooling techniques which remove heat directly from each layer of the motor coils. Our coil design has separated end-turns so that each layer of the coil is accessible to the cooling medium. We built a prototype linear motor in which these coils are cooled directly by oil circulated through the end-turns. In order to put this work in context, the next section reviews linear motor applications, history, and conventional cooling techniques. Following that, we present a summary of the accomplishments of this thesis.

1.1 Background

Machine designers are increasingly using linear motors in high performance machine tools. Linear motors provide higher speeds and forces, smoother motion, and better accuracy than conventional actuators such as ballscrews [9, 5, 7]. Even at high speeds, they do not generate wear particles and are therefore suitable for clean room transportation and inspection applications. They are also used in high speed machining centers in the automotive and aerospace industries.

In the automotive industry, for example, Ford has deployed high speed, flexible linear motor driven machines in its Dearborn engine plant [29, 36]. These machines were developed from 1988–1991 through a collaboration between Anorad Corp., a

linear motor company, and Ingersoll Rand, a machine tool manufacturer. Low volume production began in 1996, and the high-speed machining line makes 4.6-L V8 engine blocks for Ford's F-Series trucks. Drilling rates have increased from 12 inches per minute to 250, and boring speed has gone up from 32 inches per minute to 300 since these new machines were used. The high velocity, linear motor machines can also be easily reprogrammed to create other parts unlike conventional transfer line machines. In the aerospace industry, British Aerospace PLC is interested in machining pieces for airplane wings from aluminum blocks 3 m high by 20 m long [36]. This requires a linear motor with 20 m of travel.

Linear motors have been around since the turn of the century. One of the first traceable patents is on a shuttle propulsion linear motor (1895) by the Jacquard and Electric Shuttle Company [1]. This reluctance motor consists of a series of electromagnets that pulled an iron shuttle across the loom [22]. Many interesting primitive linear electric machines were developed in the first half of the twentieth century. By the 1960's, notable theoretical designs and prototypes were developed, especially for linear induction motors. During the 1970's and 1980's there were large efforts to develop high speed trains propelled by linear motors and possibly suspended by magnetic fields (MAGLEV). An excellent book by Laithwaite [22] presents these machines and the history of linear motors. Despite this long history, their existence has not been well-known in the machine tool industry until the last two decades. Recent advances in rare-earth permanent magnet technology [23] and digital controllers have made linear motors more powerful and popular than ever before.

1.1.1 Problem Statement

Today, one of the biggest obstacles to increased linear motor performance and more widespread usage is the thermal limit [3, 9]. Linear motors contain electric coils which produce heat when a current flows through them. This heat must be dissipated efficiently so that the motor does not get excessively hot. Motors are rated for the highest continuous current they can withstand while maintaining an acceptable temperature level. This maximum current limits the maximum force that a given motor

can produce. A machine tool designer who requires more force must select a bigger motor or use multiple motors. In either case, the machine tool will end up being bulkier and will take up more expensive space on the factory floor.

Hence, we wish to maximize the force per unit volume of motor. We have two means at our disposal to effect this improvement in a linear motor. First, we can increase the magnetic field strength—either through better magnetic materials or a clever magnet array design. In our motor, we use Neodymium-Iron-Boron rare-earth magnets with a remanence of 1.2 T. Although we considered alternative magnet arrays such as those developed by Halbach [13, 14, 15], we stuck with a conventional N-S magnet array. Second, we can increase the current limit by improved cooling of the motor coils. This is what we pursue in this thesis: Our goal is to push the thermal limit in linear motors as far as possible.

Besides increasing the force per unit volume of motor, a thermally efficient motor has other advantages. It will run cooler than less thermally efficient motors while producing the same force. This is advantageous for two reasons. First, since the coil resistance increases with temperature, it is more efficient to operate a motor at lower temperatures. Second, the motor will have a longer life if run at a lower temperature. This is because insulation materials degrade faster at high temperatures. A rule of thumb is that every 10°C rise in temperature halves the insulation lifetime [24]. Thus, improved motor thermal efficiency allows for increased power efficiency, increased maximum motor force, decreased size, or a combination of these.

1.1.2 Conventional Solutions

Many strategies have been developed to cool motors. The simplest, of course, is to let the surrounding air freely convect away the heat. In fact, this is how the vast majority of motors are cooled. Often fins are added to improve this free convection by increasing the surface area exposed to air. Forced convection of air directly by the coils or fins improves the heat transfer out of a motor. This is usually accomplished with a radial fan which blows air on the end-turns and along the coil [24]. Conventional motors also conduct heat into the iron core where it is convected away.

Some specialized cooling schemes have been developed which use inert gas or water filled jackets to remove heat from a heat-sink which is in contact with the coil. For example, Chitayat uses a serpentine cooling coil placed near the electrical coils to remove heat [6].

A review of heat transfer as it pertains to motor cooling techniques can be found in the *Handbook of Electric Motors* [24]. Kostikov et al. [21] numerically investigate heat tranfer and the temperature rise in motor windings. They find that increased internal air circulation and reduced insulation thickness do not substantially improve heat transfer; however, reducing the thickness of air interlayers in the slot insulation, and increasing the thermal conductivity of the coil impregnant do improve the heat transfer significantly. Dias et al. [28] present a finite element transient thermal analysis of an induction motor with a closed air ventilation scheme.

1.2 Thesis Overview

1.2.1 Separated End-Turn Coil

In this thesis, we present two cooling techniques which push the thermal limit in linear motors. They both depend on a special coil design such as that shown in Figure 1-1. This coil is named a "separated end-turn coil" because it has gaps in its end-turns. These gaps allow each layer of the coil to be directly cooled; this is what makes cooling techniques based on this type of coil so effective.

1.2.2 Direct Liquid Cooling

The first cooling technique explored in this thesis is direct liquid cooling of the separated end-turn coil. Oil is directly flowed through the gaps in the coil's end-turns. We built a prototype permanent magnet, synchronous motor which incorporates this direct oil cooling. It is shown in Figure 1-2. A current of 1.6 A causes a steady-state 100°C temperature rise in a free convection-cooled coil like the one shown in Figure 1-1; it takes a current of 9.0 A to cause the same temperature rise with room

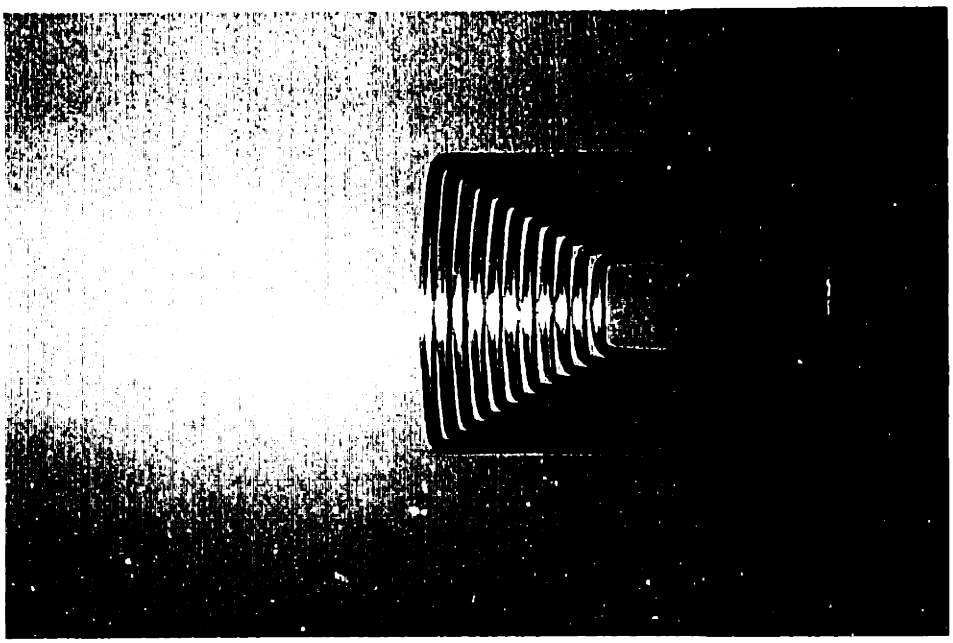

Figure 1-1: One half of our separated end-turn coil design is shown. The coil consists of 22 layers which are separated into 11 groups of two at both end-turns. Grouping them in twos cut down the end-turn size while still allowing each layer to be directly cooled.

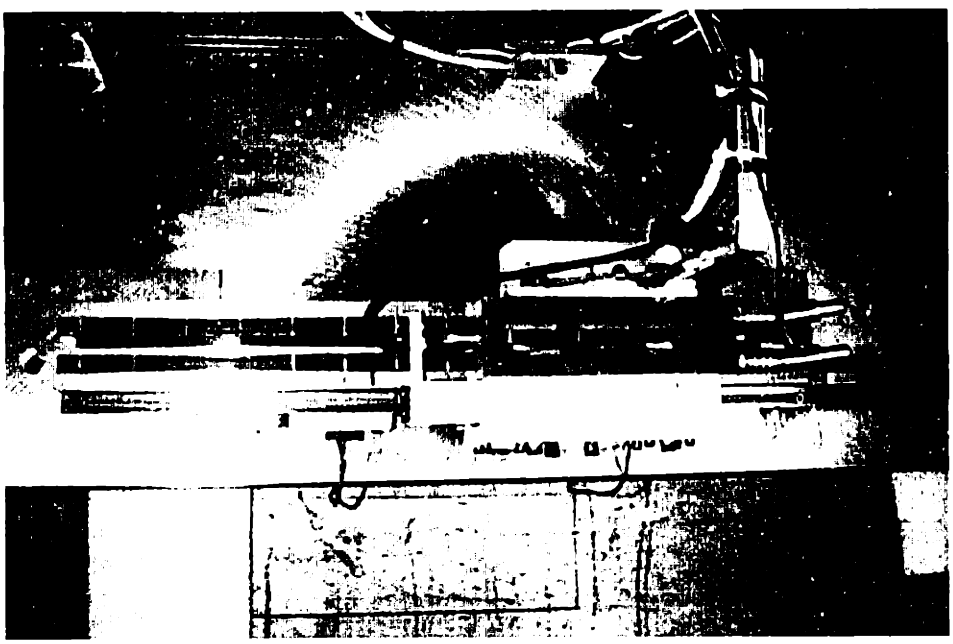

Figure 1-2: A top view of our prototype motor is shown. The moving coil assembly rides inside a stationary U-shaped magnet channel. The upper housing of the three coils contains baffles which direct the oil through the coils' separated end-turns which are shown in Figure 1-1.

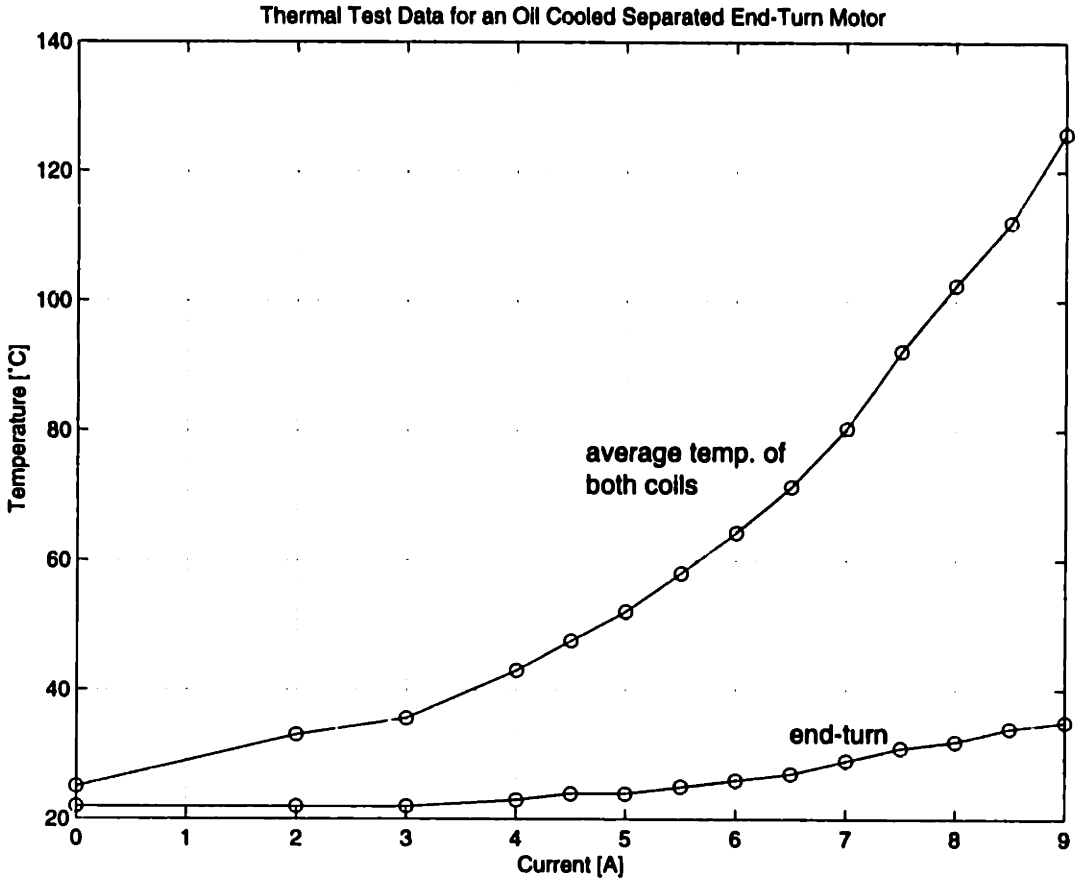

Figure 1-3: A DC current was applied across two of the three coils in our motor while oil circulated through the end-turns at a flow rate of 0.3 gpm. The average temperature of the two coils is plotted versus current. Also shown is the temperature at the middle of the end-turn. When uncooled, this same coil heats up to 125°C everywhere with only 1.6 A.

temperature oil flowing through the end-turns at the modest rate of one-third gallon per minute. Thus, our design allows nearly 6 times higher force in steady-state and dissipates 32 times as much heat. The associated thermal test data is plotted in Figure 1-3. Notice that at a current of 2.0 A, the average temperature rise in the oil-cooled motor is only 8°C, whereas the air-cooled motor would overheat at this current. Furthermore, an oil-cooled coil cools down much faster than a free convection-cooled coil. A conventional coil stays hot for 30 minutes after the current is turned off; with oil cooling, the hot spot temperature falls from 130°C to 44°C in 30 seconds. The coil's thermal time constant is approximately 60 times faster than

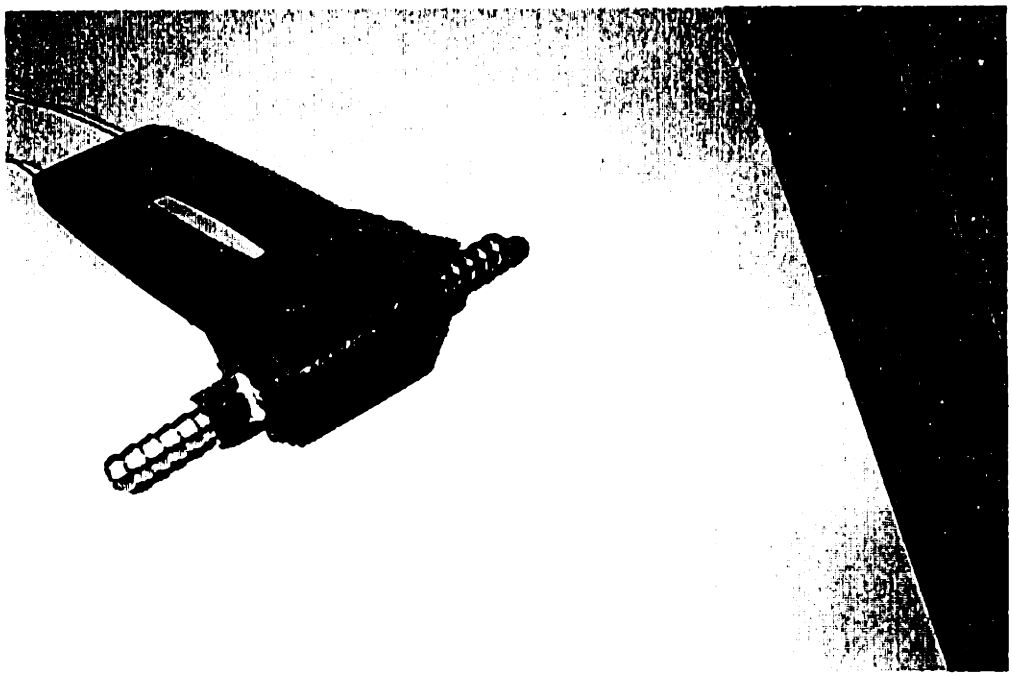

Figure 1-4: The prototype comb carries heat out of a separated end-turn coil via copper shims placed in gaps in the end-turns. The heat is then transferred to the copper block and removed by flowing water.

a free convection-cooled coil and approximately 20 times faster than a conventional coil with air blowing on it.

1.2.3 Comb Cooling

The second cooling technique developed in this thesis is called "comb-cooling" because a comb-shaped piece of copper is placed in the separated end-turns. A picture of a prototype comb is shown in Figure 1-4. The heat generated in the coil leaves the end-turns and flows down the copper fingers to the base. From there, it is removed by flowing water. The advantages of this technique are that we can use water instead of oil since the liquid does not contact the coils directly. The water circulation system is simpler than the direct oil cooling and similar to those already in use. It is also easier to prevent leaks in this approach. For our first test of comb-cooling, we only implemented the comb on one end-turn of the coil as shown in Figure 1-4. This first prototype was crude to ease the fabrication process: The fingers were much thinner

than the gaps in the end-turns, and the epoxy used to fill the voids between the fingers and coil had a low thermal conductivity. Nonetheless, this crude comb allowed 2.4 times the current of a free convection cooled coil. With a better comb, we predict that this technique would allow 4.7 times the current of a free convection cooled coil and dissipate 22 times the heat.

1.3 Thesis Organization

Chapter 2 presents the continuum electromechanical analysis for our linear motor. Although our U-shaped motor has no iron behind the coils, by symmetry, our analysis also applies to single-sided motors with iron behind the magnets and coils. Experimental force test data is presented and found to agree well with the theoretical prediction. Chapter 3 discusses the different coil designs and magnet arrays we considered for our prototype motor. Next, in chapter 4, we explain the thermal analysis for an oil-cooled separated end-turn coil which is our selected coil design and cooling scheme. Chapter 5 shows experimental results which corroborate the thermal model of the previous chapter. We describe the fabrication of our prototype motor and show many pictures of it in Chapter 6. Chapter 7 explains the controller design for our prototype motor and shows its performance. The thermal model, fabrication, and experimental results for our comb-cooling prototype are given in Chapter 8. Chapter 9 contains conclusions and suggestions for further work. Appendix A contains the Maple code used in the electromechanical analysis of Chapter 2.

Chapter 2

Electromechanical Analysis

This chapter presents the continuum electromechanical analysis of our linear motor. We use the analytical framework of Melcher [25] in which layers of electromagnetic material such as magnets, air gap, and coils are described by transfer relations. Prior analyses have investigated ironless linear motors with a variety of magnet arrays [20, 33, 34]. This type of detailed analysis provides a wealth of information for optimization and design of linear motors and has been used for several projects designed in our lab. One result of this type of analysis is that the power optimal coil thickness for an ironless stator in a single-sided motor is approximately $l/5$ where l is the magnet pitch. There is some confusion in the industry about the definition of magnet pitch. For example, for a N-S magnet array, some vendors define the magnet pitch as the length of a single N or S magnet. In theoretical work, it is more useful to define the magnet pitch as the periodicity length of the array and thus the length of both a N and S magnet. This is the definition we use in this thesis. The analysis presented in this chapter is modified from [33] to include an iron backing behind both the magnet array and the coils. The transfer relation formulation is solved symbolically with the help of Maple [35, 17], a popular computer algebra program. The most exciting result of this computation is that the power optimal coil thickness for a single-sided linear motor with iron backing behind the magnets and the coils is approximately $l/10$.

It turns out that we ended up choosing a different motor geometry without iron behind the coils for the experimental prototype in this thesis. The new motor ge-

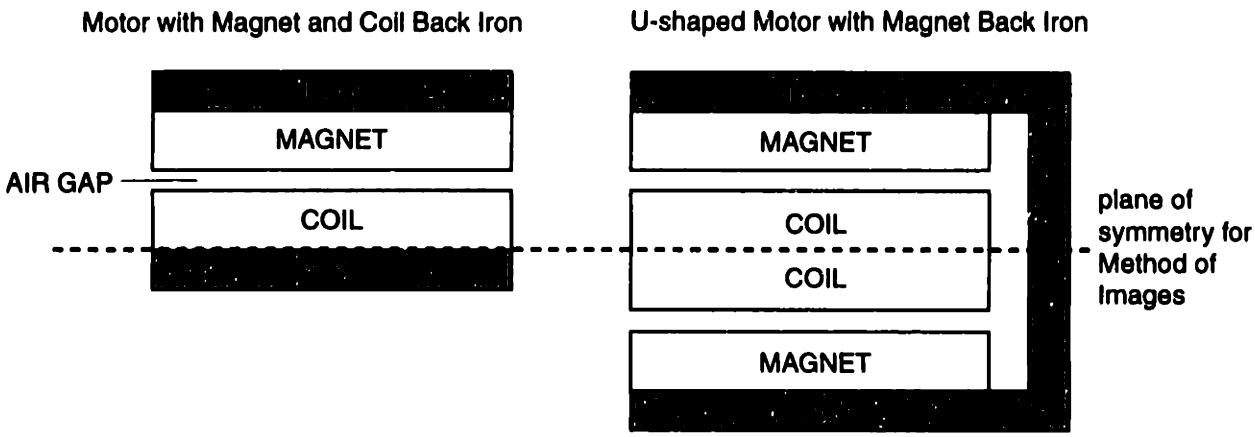

Figure 2-1: The analysis of this chapter was developed for the motor on the left with magnet and coil back iron. Due to the symmetry between this motor and the U-shaped motor geometry on the right, the analysis applies to U-shaped motors as well.

ometry is a classic U-shaped channel with magnets on both sides of the coil and a U-shaped iron backing behind the magnets. The old and new motor geometries are shown in Figure 2-1. Fortunately, the method of images allows these two quite different structures to be analyzed with the same electromechanical analysis. For the case of our U-shaped motor, a plane of symmetry cuts through the middle of the coil (Figure 2-1). According to the method of images, the magnetic fields produced above this plane of symmetry are the same as those produced in a geometry which is the same above the plane of symmetry but has iron below. Thus the power optimal coil thickness for the U-shaped motor is twice that of the single-sided motor, or $l/5$. The coil thickness of our prototype was chosen to be the same as existing motors to ease the fabrication and facilitate the comparison between the motors. The optimal coil thickness for our motor is approximately twice as thick as the coil we used. This is not as bad as it sounds, however, because the power vs. coil thickness curve is relatively flat near the minimum. In the next section we present the details of the motor continuum electromechanics.

2.1 Magnetoquasistatics and Fourier Series Notation

A permanent magnet motor is a magnetoquasistatic (MQS) system [16]. Under this approximation Maxwell's Equations for the magnetic field intensity H, magnetic flux density B, electric displacement D, and electric field E are:

$$\nabla \times H = J_f \tag{2.1}$$

$$\nabla \cdot B = 0 \tag{2.2}$$

$$\nabla \times E = -\frac{\partial B}{\partial t} \tag{2.3}$$

where J_f is the free current density and M is the magnetization. We also have continuity of free charge,

$$\nabla \cdot J_f = 0, \tag{2.4}$$

and a constitutive law relating magnetization M, field intensity H, and flux density B,

$$B = \mu_0(H + M). \tag{2.5}$$

We assume that the system is periodic and represent the periodic fields in our problem with Fourier series. We follow Melcher's notation [25] for a field quantity Φ:

$$\Phi(z,t) = \sum_{n=-\infty}^{\infty} \tilde{\Phi}_n(t) e^{-jk_n z} \tag{2.6}$$

where

$$k_n = \frac{2\pi n}{l} \tag{2.7}$$

for a field whose period is l. Further, γ_n is defined as

$$\gamma_n \equiv |k_n|. \tag{2.8}$$

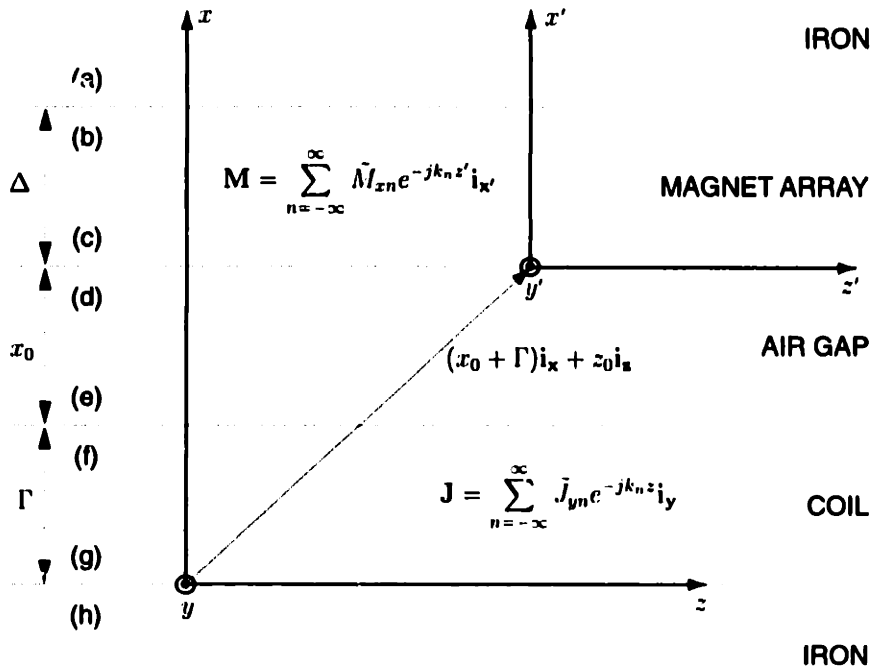

Figure 2-2: Here are the five layers used in the continuum electromechanical analysis of our linear motor. The Fourier expansions for the magnetization and current density are given. Also note the two coordinate systems and the layer thicknesses, Γ, x_0, and Δ. The primed frame moves with the magnet array.

2.2 Transfer Relations and Boundary Conditions

A cross-sectional model of our linear motor is shown in Figure 2-2. The three middle layers represent the magnet array, air gap, and coils of the linear motor. In previous analyses [33, 34, 20] the outer two layers are semi-infinite free space since the authors are modeling ironless motors. Here, we model a motor with iron layers behind the magnets and behind the coils. We make a common engineering approximation that the iron layers have infinite permeability, $\mu \rightarrow \infty$. In this limit the thickness of the iron layer does not affect the analysis so we can model the thickness as semi-infinite. In the real design this will be a good approximation for the magnetic back iron as long as we make the iron layer thick enough to avoid saturation. It is interesting to note that for the coil back iron which models the symmetry of the problem (Figure 2-1), the condition $\mu \rightarrow \infty$ is not an approximation but is in fact exact. This is because physically there is no coil back iron; we include this layer so that we need only analyze

half of a symmetric structure. We saw that this conclusion followed from the Method of Images (Figure 2-1).

The upper and lower sides of the boundaries are labeled with the letters (a) through (h). The first step of our analysis involves finding the vector potential A_y and the magnetic field intensity H_z at the top and bottom of each surface. From these surface variables we will see that we can find the field distributions everywhere. Thus we have sixteen unknowns and will need sixteen simultaneous linear equations to solve the problem. Melcher's transfer relations describe the fields within the layers. They relate the H_z's and A_y's for the two edges of a layer via two coupled equations. The semi-infinite layers provide only one equation each. This gives us eight equations. Four more equations come from jump conditions for A_y across the four boundaries (separating the five layers). An additional four equations come from jump conditions on H_z across the four boundaries.

Our ultimate goal is to find $\tilde{H}^d_{zn}$ and $\tilde{H}^d_{xn}$ so that we can evaluate the stress tensor along this plane to find an expression for the force produced on the magnets by the motor. In order to simplify the analysis, we solve the layer problem first for the fields due to the magnet and then for the fields due to the coils. These two solutions can then be superposed because the problem is linear. The primed coordinate frame shown in Figure 2-2 contains the magnet array and moves relative to the coils thus allowing motion between the two parts of the motor.

2.2.1 Field Solutions for Magnets

We follow previous convention and use a superscript S to denote the field due to the coils only (which are part of the stator in the original analyses). Likewise a superscript of M will denote a field due only to the magnets. In this section we solve for the fields due to the magnets alone. These fields are denoted by a left superscript M, e.g. ${}^{M}\tilde{H}^a_{zn}$.

2.2.1.1 Transfer Relations

Due to the semi-infinite plane of material at boundary (a) with $\mu \rightarrow \infty$ we have

$$^{M}\tilde{H}^{a}_{zn} = 0. \tag{2.9}$$

As given in [20, 33], transfer relations for the magnet region are

$$\begin{bmatrix} ^{M}\tilde{H}^{b}_{zn} \\ ^{M}\tilde{H}^{c}_{zn} \end{bmatrix} = \frac{k_n}{\mu_0} \begin{bmatrix} -\coth(k\Delta) & \frac{1}{\sinh(k\Delta)} \\ -\frac{1}{\sinh(k\Delta)} & \coth(k\Delta) \end{bmatrix} \begin{bmatrix} ^{M}\tilde{A}^{b}_{yn} \\ ^{M}\tilde{A}^{c}_{yn} \end{bmatrix} + \begin{bmatrix} \frac{\cosh(k_n\Delta)-1}{\sinh(k_n\Delta)} \\ -\frac{\cosh(k_n\Delta)-1}{\sinh(k_n\Delta)} \end{bmatrix} j\mu_0\tilde{M}_{xn}. \tag{2.10}$$

The air gap transfer relations are

$$\begin{bmatrix} ^{M}\tilde{H}^{d}_{zn} \\ ^{M}\tilde{H}^{e}_{zn} \end{bmatrix} = \frac{k_n}{\mu_0} \begin{bmatrix} -\coth(kx_0) & \frac{1}{\sinh(kx_0)} \\ -\frac{1}{\sinh(kx_0)} & \coth(kx_0) \end{bmatrix} \begin{bmatrix} ^{M}\tilde{A}^{d}_{yn} \\ ^{M}\tilde{A}^{e}_{yn} \end{bmatrix}. \tag{2.11}$$

The transfer relations for the current carrying layer assuming zero current density are

$$\begin{bmatrix} ^{M}\tilde{H}^{f}_{zn} \\ ^{M}\tilde{H}^{g}_{zn} \end{bmatrix} = \frac{k_n}{\mu_0} \begin{bmatrix} -\coth(k\Gamma) & \frac{1}{\sinh(k\Gamma)} \\ -\frac{1}{\sinh(k\Gamma)} & \coth(k\Gamma) \end{bmatrix} \begin{bmatrix} ^{M}\tilde{A}^{f}_{yn} \\ ^{M}\tilde{A}^{g}_{yn} \end{bmatrix}. \tag{2.12}$$

We have left out the source term for the current here since this part of the analysis is only concerned with the fields caused by the magnet. The relation for the bottom $\mu \rightarrow \infty$ material is

$$^{M}\tilde{H}^{h}_{zn} = 0. \tag{2.13}$$

2.2.1.2 Continuity of Magnetic Vector Potential

Since there are no impulsive fields, the magnetic vector potential is continuous everywhere. This gives us the following four trivial equations,

$$\begin{aligned} {}^{M}\tilde{A}^{a}_{yn} &= {}^{M}\tilde{A}^{b}_{yn}, \\ {}^{M}\tilde{A}^{c}_{yn} &= {}^{M}\tilde{A}^{d}_{yn}, \\ {}^{M}\tilde{A}^{e}_{yn} &= {}^{M}\tilde{A}^{f}_{yn}, \\ {}^{M}\tilde{A}^{g}_{yn} &= {}^{M}\tilde{A}^{h}_{yn}. \end{aligned} \tag{2.14}$$

2.2.1.3 Jump Conditions

In this analysis we consider only a N-S magnet array such that $\tilde{M}_{zn} = 0$. Under this condition the parallel component of the magnetic field intensity is continuous across boundaries since we have no equivalent surface currents representing the termination of horizontal magnetization. Again this gives us a set of trivial equations,

$$\begin{aligned} {}^{M}\tilde{H}^{a}_{zn} &= {}^{M}\tilde{H}^{b}_{zn}, \\ {}^{M}\tilde{H}^{c}_{zn} &= {}^{M}\tilde{H}^{d}_{zn}, \\ {}^{M}\tilde{H}^{e}_{zn} &= {}^{M}\tilde{H}^{f}_{zn}, \\ {}^{M}\tilde{H}^{g}_{zn} &= {}^{M}\tilde{H}^{h}_{zn}. \end{aligned} \tag{2.15}$$

2.2.1.4 Solutions

The solution of the above sixteen equations is carried out in the software package Maple [17, 35]. We only need expressions for $\tilde{H}^{d}_{zn}$ and $\tilde{H}^{d}_{xn}$ to calculate the stress tensor at surface (d). $\tilde{H}^{d}_{zn}$ is one of the sixteen variables we have solved for, and $\tilde{H}^{d}_{xn}$ is directly related to $\tilde{A}^{d}_{yn}$ which is one of the sixteen variables. This relationship comes from the definition $\mathbf{B} = \nabla \times \mathbf{A}$ and from the fact that in this type of problem $\mathbf{A}$ has only a y-directed component, from which it follows that:

$$H_{xn} = -\frac{1}{\mu_0}\frac{\partial}{\partial z}A_{yn} \tag{2.16}$$

and thus

$$\tilde{H}_{xn} = \frac{jk_n}{\mu_0}\tilde{A}_{yn}. \tag{2.17}$$

Omitting the intermediate details (see Appendix A), the solutions for the complex amplitudes of the field quantities at surface (d) due to the magnet array are:

$${}^{M}\tilde{H}^{d}_{zn} = \left(\frac{j\tilde{M}_{vn}}{2}\right)\left(\frac{e^{2k_n g} + e^{2k_n \Delta} - e^{2k_n(\Delta+g)} - 1}{e^{2k_n(\Delta+g)} - 1}\right) \tag{2.18}$$

$${}^{M}\tilde{H}^{d}_{xn} = \left(-\frac{\coth(kg)\tilde{M}_{vn}}{2}\right)\left(\frac{e^{2k_n g} + e^{2k_n \Delta} - e^{2k_n(\Delta+g)} - 1}{e^{2k_n(\Delta+g)} - 1}\right), \tag{2.19}$$

where $g \equiv x_0 + \Gamma$ is the gap between the magnets and stator back iron.

The Fourier components of the vertical magnetization for a magnet array are given by

$$\tilde{M}_{vn} = \frac{1}{l}\int_0^l M_v e^{jk_n z'} dz'. \tag{2.20}$$

For a N-S magnet array, the fundamental Fourier coefficients of $\tilde{M}_{vn}$ for the square wave representing the magnetization are

$$\begin{aligned} \tilde{M}_{v1} &= \frac{2}{\pi}M_0 j \\ \tilde{M}_{v-1} &= -\frac{2}{\pi}M_0 j, \end{aligned} \tag{2.21}$$

where $\mu_0 M_0$ is the remanence of the permanent magnets.

2.2.2 Field Solutions for Coils

In this section we solve for the fields due to the coils alone with the permanent magnets removed. These quantities are indicated with a left superscript S, e.g., ${}^{S}\tilde{H}^{a}_{zn}$.

2.2.2.1 Transfer Relations

For a semi-infinite plane of material with $\mu \to \infty$ we have

$${}^{S}\tilde{H}^{a}_{zn} = 0. \tag{2.22}$$

The transfer relations for the magnet region are given in [33],

$$\begin{bmatrix} {}^{S}\tilde{H}^{b}_{zn} \\ {}^{S}\tilde{H}^{c}_{zn} \end{bmatrix} = \frac{k_n}{\mu_0} \begin{bmatrix} -\coth(k\Delta) & \frac{1}{\sinh(k\Delta)} \\ -\frac{1}{\sinh(k\Delta)} & \coth(k\Delta) \end{bmatrix} \begin{bmatrix} {}^{S}\tilde{A}^{b}_{yn} \\ {}^{S}\tilde{A}^{c}_{yn} \end{bmatrix}. \tag{2.23}$$

Note that we have omitted the permanent magnet source term since in this part of the problem we are only finding the fields due to the coils. The air gap transfer relations are

$$\begin{bmatrix} {}^{S}\tilde{H}^{d}_{zn} \\ {}^{S}\tilde{H}^{e}_{zn} \end{bmatrix} = \frac{k_n}{\mu_0} \begin{bmatrix} -\coth(kx_0) & \frac{1}{\sinh(kx_0)} \\ -\frac{1}{\sinh(kx_0)} & \coth(kx_0) \end{bmatrix} \begin{bmatrix} {}^{S}\tilde{A}^{d}_{yn} \\ {}^{S}\tilde{A}^{e}_{yn} \end{bmatrix}. \tag{2.24}$$

The transfer relations for the current carrying layer are

$$\begin{bmatrix} {}^{S}\tilde{H}^{f}_{zn} \\ {}^{S}\tilde{H}^{g}_{zn} \end{bmatrix} = \frac{k_n}{\mu_0} \begin{bmatrix} -\coth(k\Gamma) & \frac{1}{\sinh(k\Gamma)} \\ -\frac{1}{\sinh(k\Gamma)} & \coth(k\Gamma) \end{bmatrix} \begin{bmatrix} {}^{S}\tilde{A}^{f}_{yn} \\ {}^{S}\tilde{A}^{g}_{yn} \end{bmatrix} + \begin{bmatrix} \frac{\cosh(k_n\Gamma)-1}{\sinh(k_n\Gamma)} \\ -\frac{\cosh(k_n\Gamma)-1}{\sinh(k_n\Gamma)} \end{bmatrix} \frac{\mu_0}{k_n} \tilde{J}_{yn}. \tag{2.25}$$

The relation for the bottom $\mu \to \infty$ material is

$${}^{S}\tilde{H}^{h}_{zn} = 0. \tag{2.26}$$

2.2.2.2 Continuity of Magnetic Vector Potential

These are the same as in the permanent magnet case, i.e.,

$$\begin{aligned} {}^{S}\tilde{A}^{a}_{yn} &= {}^{S}\tilde{A}^{b}_{yn} \\ {}^{S}\tilde{A}^{c}_{yn} &= {}^{S}\tilde{A}^{d}_{yn} \\ {}^{S}\tilde{A}^{e}_{yn} &= {}^{S}\tilde{A}^{f}_{yn} \\ {}^{S}\tilde{A}^{g}_{yn} &= {}^{S}\tilde{A}^{h}_{yn} \end{aligned}. \tag{2.27}$$

2.2.2.3 Jump Conditions

These are the same as in the permanent magnet case, i.e.,

$$\begin{aligned} {}^{s}\tilde{H}^{a}_{zn} &= {}^{s}\tilde{H}^{b}_{zn} \\ {}^{s}\tilde{H}^{c}_{zn} &= {}^{s}\tilde{H}^{d}_{zn} \\ {}^{s}\tilde{H}^{e}_{zn} &= {}^{s}\tilde{H}^{f}_{zn} \\ {}^{s}\tilde{H}^{g}_{zn} &= {}^{s}\tilde{H}^{h}_{zn} \end{aligned} \quad . \tag{2.28}$$

2.2.2.4 Solutions

The sixteen unknowns are found by the computer algebra program Maple [35, 17]. Section A.2 of Appendix A presents this calculation. We are only interested in finding ${}^{s}\tilde{H}^{d}_{zn}$ and ${}^{s}\tilde{H}^{d}_{xn}$. The first coefficient is one of our unknowns, and after some simplification can be solved for as

$${}^{s}\tilde{H}^{d}_{zn} = \left(\frac{-\tilde{J}_{yn}}{2k_n}\right)\left(\frac{(e^{2k_n\Gamma}-1)(e^{2k_n\Delta}-1)e^{k_n x_0}}{e^{2k_n(\Gamma+\Delta+x_0)}-1}\right) \text{ (iron)}. \tag{2.29}$$

For comparison, we provide the value of this same parameter found in previous (ironless) analyses [33, 34]:

$${}^{s}\tilde{H}^{d}_{zn} = \left(\frac{-\tilde{J}_{yn}}{2\gamma_n}\right) e^{-\gamma_n x_0}(1-e^{-\gamma_n\Gamma}) \text{ (ironless)}. \tag{2.30}$$

The easiest way to see that these two expressions are in fact quite similar is to note that for typical values of Γ, Δ, and x_0, and specializing to $n > 0$, the approximation, $e^{2k_n(\Gamma+\Delta+x_0)} \gg 1$, holds. Recall that $\gamma_n = |k_n|$ so for $n > 0$ we have $\gamma_n = k_n$. We can then (temporarily) ignore the 1 in the denominator of equation (2.29) using our approximation. We now have

$${}^{s}\tilde{H}^{d}_{zn} = \left(\frac{-\tilde{J}_{yn}}{2k_n}\right) e^{-k_n x_0}(1-e^{-2k_n\Gamma})(1-e^{-2k_n\Delta}) \text{ (iron, approximate, } n>0) \tag{2.31}$$

which when compared with the ironless case (2.30) gives us a preview of the differences we will find between the solutions with and without iron. In particular, we note:

1. The $e^{-k_n x_0}$ dependence is recovered in the approximation.

2. The term $(1-e^{-2k_n\Gamma})$ is similar to the Γ term in the ironless case, but note that Γ is now replaced by 2Γ. Recall that our final result will be that the optimal layer thickness is half of the ironless case ($l/10$ versus $l/5$); this shows why this result holds.

3. There is a new dependence on Δ in the term, $(1-e^{-2k_n\Delta})$, not found in the ironless case. This makes sense because the distance to the iron layer behind the magnets should matter. In the ironless case, there is only non-magnetic material above the coils so this distance is irrelevant.

4. The stator-driven fields are larger with the back iron because $e^{-2k_n\Gamma} < e^{-k_n\Gamma}$ and $e^{-2k_n\Delta} < e^{-k_n\Delta}$.

We can next find $\tilde{H}^d_{xn}$ by applying equation (2.17) yielding

$$ {}^{S}\tilde{H}^d_{xn} = \left(\frac{j\tilde{J}_{yn}}{2k_n}\right)\frac{(e^{2k_n\Gamma}-1)(e^{2k_n\Delta}+1)e^{k_n x_0}}{e^{2k_n(\Gamma+\Delta+x_0)}-1}. \tag{2.32} $$

2.3 Total Fields

We can now superpose equations (2.18) and (2.29) for ${}^{M}\tilde{H}^d_{zn}$ and ${}^{S}\tilde{H}^d_{zn}$ to yield the combined field due to magnet array and stator, $\tilde{H}^d_{zn}$. Likewise, equations (2.19) and (2.32) for ${}^{M}\tilde{H}^d_{xn}$ and ${}^{S}\tilde{H}^d_{xn}$ are combined to yield $\tilde{H}^d_{xn}$. For convenience, we consider the superposed field to be stationary in the magnet frame. Thus, we must use $z = z_0 + z'$ for the stator fields which results in a multiplicative term of $e^{-jk_n z_0}$ in these terms. The total fields at boundary (d) are thus

$$ \begin{aligned} \tilde{H}^d_{zn} &= \left(\frac{j\tilde{M}_{vn}}{2}\right)\left(\frac{e^{2k_n(\Gamma+x_0)}+e^{2k_n\Delta}-e^{2k_n(\Gamma+\Delta+x_0)}-1}{e^{2k_n(\Gamma+\Delta+x_0)}-1}\right) \\ &\quad + \left(\frac{-\tilde{J}_{yn}}{2k_n}\right)\left(\frac{(e^{2k_n\Gamma}-1)e^{k_n x_0}}{e^{2k_n(\Gamma+\Delta+x_0)}-1}\right)(e^{2k_n\Delta}-1)e^{-jk_n z_0} \end{aligned} \tag{2.33} $$

$$\tilde{H}^d_{xn} = \left(-\frac{\coth(k_n(\Gamma+x_0))\tilde{M}_{yn}}{2}\right)\left(\frac{e^{2k_n(\Gamma+x_0)}+e^{2k_n\Delta}-e^{2k_n(\Gamma+\Delta+x_0)}-1}{e^{2k_n(\Gamma+\Delta+x_0)}-1}\right)$$
$$+\left(\frac{j\tilde{J}_{yn}}{2k_n}\right)\left(\frac{(e^{2k_n\Gamma}-1)e^{k_n x_0}}{e^{2k_n(\Gamma+\Delta+x_0)}-1}\right)(e^{2k_n\Delta}+1)e^{-jk_n z_0}. \quad (2.34)$$

2.4 Motor Force via Maxwell Stress Tensor

Now we are ready to use the Maxwell stress tensor to find the motor force. The theory underlying this analysis is given in [25]. The force F_i in the ith direction on a material is

$$F_i = \oint_S T_{ij} n_j da \quad (2.35)$$

where n_j is the jth component of the normal vector to the surface S which is being integrated over. The Maxwell stress tensor T_{ij} is given by

$$T_{ij} = \mu H_i H_j - \frac{\mu}{2}\delta_{ij}\sum_k H_k H_k, \quad (2.36)$$

where δ_{ij} is the Kronecker delta[1]. We enclose the magnet array in an imaginary box with one side at surface (d) where we have just calculated the fields and the opposite side at infinity where the fields are zero as shown in Figure 2-3. The edges of the box are chosen to include an integral number of magnet periods so that by symmetry the stresses along these sides cancel. The surface integral thus simplifies to evaluating the spatial average of the stress tensor at surface (d) and multiplying by the area A:

$$F_z = -A\mu_0\langle T^d_{xz}\rangle_z = -A\mu_0\langle H^d_x H^d_z\rangle_z, \quad (2.37)$$

where $\langle\cdot\rangle$ denotes a spatial average in z. We thus need to calculate

$$F_z = -A\mu_0(\tilde{H}^d_{x(-1)}\tilde{H}^{d*}_{z(-1)} + \tilde{H}^d_{x(1)}\tilde{H}^{d*}_{z(1)}) \quad (2.38)$$

[1] $\delta_{ij} = \begin{cases} 1, & i=j \\ 0, & i\neq j \end{cases}$

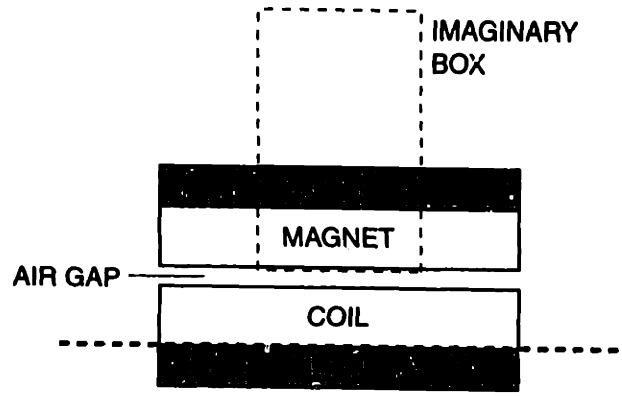

Figure 2-3: We calculate the forces on this imaginary box. From our analysis we know the fields for the side of the box in the air gap. The opposite side is at inifinity where the fields are zero. The remaining two edges of the box enclose an integral number of magnet periods so that by symmetry the stresses along these sides cancel.

where we have used the spatial averaging theorem [25],

$$\left\langle \sum_{n=-\infty}^{\infty} \tilde{A}_n e^{-jk_n z} \sum_{m=-\infty}^{\infty} \tilde{B}_m e^{-jk_m z} \right\rangle_z = \sum_{n=-\infty}^{\infty} \tilde{A}_n \tilde{B}_{-n} = \sum_{n=-\infty}^{\infty} \tilde{A}_n \tilde{B}_n^*. \tag{2.39}$$

We assume a sinusoidal current density with a period l in the coils. Although we do not actually have a sinusoidal excitation, this fundamental harmonic approximates the real distribution and allows the force solution to be written down in a simple analytical form. For a pure sinusoidal excitation, all components $\tilde{J}_{yn}$ are zero except for the fundamental components, $n = \pm 1$:

$$\begin{aligned} \tilde{J}_{y1} &= J_a + jJ_b \\ \tilde{J}_{y-1} &= J_a - jJ_b. \end{aligned} \tag{2.40}$$

Here, $2J_a$ and $2J_b$ are the peak current densities for the two sinusoidally distributed phases.

We substitute for $\tilde{H}^d_{zn}$ and $\tilde{H}^d_{xn}$ in equation (2.38) using equations (2.33), (2.34), (2.40), and (2.21). A considerable amount of algebra using Maple [35, 17] yields (see

Appendix A)

$$F_z = \mu_0 M_0 \frac{wl^2}{\pi^2} \left[\frac{e^{\gamma x_0}(e^{2\gamma\Delta} - 1)(e^{2\gamma\Gamma} - 1)}{e^{2\gamma(\Delta+\Gamma+x_0)} - 1} \right] (J_a \cos\gamma z_0 + J_b \sin\gamma z_0). \tag{2.41}$$

This equation is the key result of this chapter. It predicts the force per spatial wavelength produced by a motor with iron behind the magnets and coils, and with a sinusoidally distributed stator winding. This result is an extension of the results in [33, 34] which accounts for the back iron. Our analysis was for a N-S magnet array, but a simple adjustment of equation (2.21) will allow for other arrays such as the Halbach configuration. For comparison, we repeat—in a suggestive form—the solution for the ironless case with a Halbach magnet array which has appeared in several papers [33, 34]:

$$F_z = \mu M_0 \frac{\sqrt{2} wl^2}{\pi^2} \left[(1 - e^{-\gamma\Gamma})(1 - e^{-\gamma\Delta}) e^{-\gamma x_0} \right] (J_a \cos\gamma z_0 + J_b \sin\gamma z_0). \tag{2.42}$$

Some comments are in order:

- The $\sqrt{2}$ in equation (2.42) is there since this equation applies to a motor using a Halbach magnet array. For ironless motors, the Halbach magnet array produces a field that is $\sqrt{2}$ times stronger than a conventional N-S magnet array. Had a normal N-S array been used in that computation, the $\sqrt{2}$ would not appear. A comparison of four magnet arrays—regular N-S, four block Halbach, ideal Halbach, and vertical sinusoidal—is done in a paper by Trumper et. al. [34]. Note well, however, that in the case of a motor with iron (2.41) the substitution of a Halbach array for a N-S array will *not* improve the force by a factor of $\sqrt{2}$. The improvement will be much less. An intuitive explanation for this is that the magnetic back iron is placed on the low-field side of the Halbach array and thus affects the field less than for a N-S array. John Ofori offers another intuitive explanation for the effects of back iron on magnet arrays using the Method of Images [27].

  This leads to the following pedantic point. The proper way to compare equa-

tions (2.41) and (2.42) is by removing the $\sqrt{2}$ from the second equation thus converting a Halbach ironless motor into a N-S ironless motor. It would be incorrect, albeit algebraically the same, to add a $\sqrt{2}$ to the first equation in a mistaken attempt to convert a N-S iron-backed motor into a Halbach iron-backed motor.

- It is illuminating to examine the limit where $e^{2\gamma(\Delta+\Gamma+x_0)} \gg 1$. For our motor, we have $\gamma = 2\pi/l = 2\pi/(60 \text{ mm})$, $\Delta = 11.43$ mm, $\Gamma = 3.81$ mm, $x_0 = 1.02$ mm yielding $e^{2\gamma(\Delta+\Gamma+x_0)} = 30.1$. In this case, $e^{2\gamma(\Delta+\Gamma+x_0)} \gg 1$ is a very good approximation.

  Assuming that our parameters are such that the limit $e^{2\gamma(\Delta+\Gamma+x_0)} \gg 1$ holds, we have $e^{2\gamma(\Delta+\Gamma+x_0)} - 1 \approx e^{2\gamma(\Delta+\Gamma+x_0)}$ in the denominator of equation (2.41). Under this approximation, the equation simplifies to

$$F_z = \mu M_0 \frac{wl^2}{\pi^2} \left[(1 - e^{-2\gamma\Gamma})(1 - e^{-2\gamma\Delta})e^{-\gamma x_0}\right] (J_a \cos\gamma z_0 + J_b \sin\gamma z_0). \quad (2.43)$$

  Equations (2.43) and (2.42) for the iron-backed motor and the ironless motor, respectively, are quite similar. Apart from the $\sqrt{2}$, which was discussed previously, they can be made identical by the following equalities:

$$\Gamma_{ironless} = 2\Gamma_{iron} \quad (2.44)$$

$$\Delta_{ironless} = 2\Delta_{iron} \quad (2.45)$$

  The advantages of an iron-backed motor are clear: We can achieve the same force in an iron-backed motor with half the magnets and half the coil thickness as compared with an ironless motor. This result is reasonable since an iron layer behind a magnet produces the image of that magnet, thus effectively doubling its size. The same is true for the coil. Remember that this result is only strictly true when the limit $e^{2\gamma(\Delta+\Gamma+x_0)} \gg 1$ holds, as will be the case in practical implementations.

l	Magnet Pitch	60.0	mm
Δ	Magnet Thickness	11.43	mm
Γ	Coil Half-Thickness[2]	3.81	mm
x_0	Gap between magnets and coil	1.02	mm
w	Width of active part of motor	49.4	mm
$\mu_0 M$	Magnet Remanence	1.25	T

Table 2.1: Prototype Motor Parameters

- In an ironless motor, the force equation for F_x is similar to the equation for F_z (2.42) and the two are often written in matrix form. For a motor containing iron, the F_x force is quite different from the F_z force. In fact, F_x has a term proportional to J^2 and one proportional to J. Since F_x is nonlinear in J, it cannot be written in matrix form.

2.5 Force Constant Calculation

We want to calculate the force constant of our motor using equation (2.41). Table 2.1 summarizes the motor parameters. It is tricky to calculate J_a for our motor. This is because there are gaps between the coils and the periodicity of the coils is not the same as for the magnets (Figure 2-4). We calculate the actual current density of the coils driven by terminal current I as

$$J = \frac{(242 \text{ turns})I}{(11.84 \text{ mm})(7.62 \text{ mm})} = (2.68 \times 10^6)I \tag{2.46}$$

and compensate for the gaps by considering the three coils to be folded back into one magnetic period even though they are spread over two. Note here that the full coil thickness of 7.62 mm is used. The terms in equation (2.41) are next evaluated:

$$\gamma = \frac{2\pi}{l} = 104.7, \tag{2.47}$$

[2]The coil thickness listed here is 1/2 the actual coil thickness. The coil itself is 2 × 3.81 mm = 7.62 mm thick, but since our analysis is based on a half-model, we list here the coil half-thickness. See Figure 2-1.

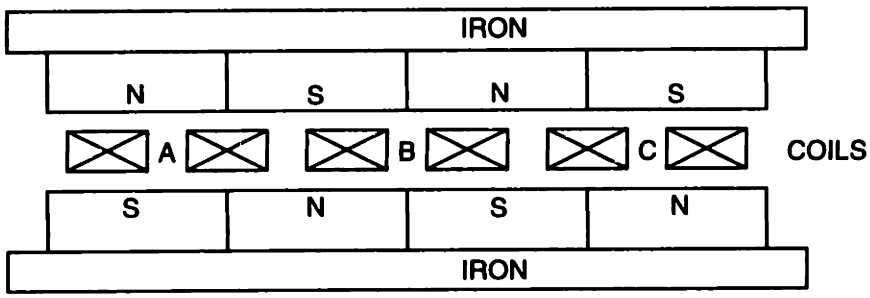

Figure 2-4: A cross-section of the motor shows that the period of the coils is different from the period of the magnet array. There are three coils for every two magnet pitch lengths.

$$\mu_0 M \frac{wl^2}{\pi^2} = 2.25 \times 10^{-5}, \tag{2.48}$$

$$e^{\gamma x_0} = 1.11, \tag{2.49}$$

$$e^{2\gamma\Delta} - 1 = 10.96 - 1 = 9.96, \tag{2.50}$$

$$e^{2\gamma\Gamma} - 1 = 2.22 - 1 = 1.22, \tag{2.51}$$

$$e^{2\gamma(\Delta+\Gamma+x_0)} - 1 = 30.13 - 1 = 29.13. \tag{2.52}$$

The motor commutation laws are

$$J_a = \frac{J}{2}\cos\gamma z_0 \tag{2.53}$$

$$J_b = \frac{J}{2}\sin\gamma z_0. \tag{2.54}$$

Thus, the term, $(J_a \cos\gamma z_0 + J_b \sin\gamma z_0)$, is equivalent to half the peak current, $J/2$, when the motor is commutated properly. Since we want the motor constant in terms of rms current rather than peak current, we must add a factor of $\sqrt{2}$. We therefore multiply J in equation (2.46) by $\sqrt{2}/2$ and substitute it for the term, $(J_a \cos\gamma z_0 + J_b \sin\gamma z_0)$, in order to get the force per rms current. The result is a predicted motor force constant, K_f, of

$$K_f = 39.69 \ \frac{\mathrm{N}}{\mathrm{A_{rms}}}. \tag{2.55}$$

This agrees quite well with the experimentally determined value of

$$K_f = 35.3\frac{\mathrm{N}}{\mathrm{A_{rms}}}. \tag{2.56}$$

A description of the experimental tests used to measure the force constant is given in section 2.7.

2.6 Power Optimal Coil Thickness

2.6.1 Analytical Results

In this section, we derive an expression for the power dissipation in the motor as a function of the various motor parameters. We can invert equation (2.41) to yield the commutation law for our motor. We then can calculate the power dissipation using an average value of J^2/σ [34]. We introduce the variables N_s for the number of spatial periods l of the coils and N_m for the number of spatial periods l of the magnets which interact with the coils. The power dissipation P_t for the motor with iron is thereby found to be

$$P_t = \frac{(3)2N_s\pi^4\Gamma}{N_m^2\sigma(\mu_0 M_0)^2 w l^3}\left[\frac{e^{2\gamma(\Delta+\Gamma+x_0)}-1}{e^{\gamma x_0}(e^{2\gamma\Delta}-1)(e^{2\gamma\Gamma}-1)}\right]^2 F_z^2. \tag{2.57}$$

For comparison, we repeat the result from [34] for the ironless motor as well:

$$P_t = \frac{(3)N_s\pi^4\Gamma}{N_m^2\sigma(\mu_0 M_0)^2 w l^3}\left[\frac{e^{2\gamma x_0}}{(1-e^{-\gamma\Gamma})^2(1-e^{-\gamma\Delta})^2}\right] F_z^2. \tag{2.58}$$

The factor of three in equations (2.57) and (2.58) is added in the original analysis by Trumper, Williams, and Nguyen [34] to account for non-idealities in the packing factor of the windings, winding length in the end-turns, and fringing fields.

We next attempt to find the power optimal thickness of the coils by setting $\partial P_t/\partial\Gamma = 0$. In the ironless case (2.58), this derivative involves only the parameter l (via $\gamma = 2\pi/l$) and Γ. The physics is different for the motor with iron; the

derivative involves x_0 and Δ as well as l and Γ. We will see that this dependence is small in many practical cases, but it is interesting that the power optimal thickness depends on new variables—the magnet thickness and air gap—in the motor with iron.

We now apply the same approximation, $e^{2\gamma(\Delta+\Gamma+x_0)} \gg 1$, that we used previously (in section 2.4). We find that this approximation eliminates the x_0 and Δ dependence just mentioned. That is, pulling out the term which depends on Γ gives

$$P_t(\Gamma) \propto \Gamma \frac{1}{(1-e^{-2\gamma\Gamma})^2}. \tag{2.59}$$

For comparison, the result in the ironless case is [34]:

$$P_t(\Gamma) \propto \Gamma \frac{1}{(1-e^{-\gamma\Gamma})^2}. \tag{2.60}$$

The difference between the expressions for the iron-backed and ironless cases is a factor of 2 in front of the Γ in the exponent. Setting $\partial P_t/\partial\Gamma = 0$ yields a transcendental equation whose solution is $2\gamma\Gamma \approx 1.25$, or

$$\Gamma_{optimal} \approx \frac{l}{10}. \tag{2.61}$$

This is the result we alluded to at the beginning of the chapter. The power optimal coil thickness for an iron-backed motor is half that of an equivalent ironless motor.

Although we have found the optimal thickness, it is important to realize that the power vs. coil thickness plot is very flat near this minimum. Figure 2-5 shows this curve for our motor parameters which are given in Table 2.1. The power is normalized to 1.0 for the minimum power dissipation. This minimum occurs at a coil half-thickness of 5.57 mm which is very close to the $l/10 = 6.0$ mm approximation. It is marked by an "X" on the plot. The coil half-thickness of our motor is marked with an "O." Even though it is smaller than optimum at 3.81 mm, the total power dissipation is only 5% higher than the minimum. This is perfectly acceptable.

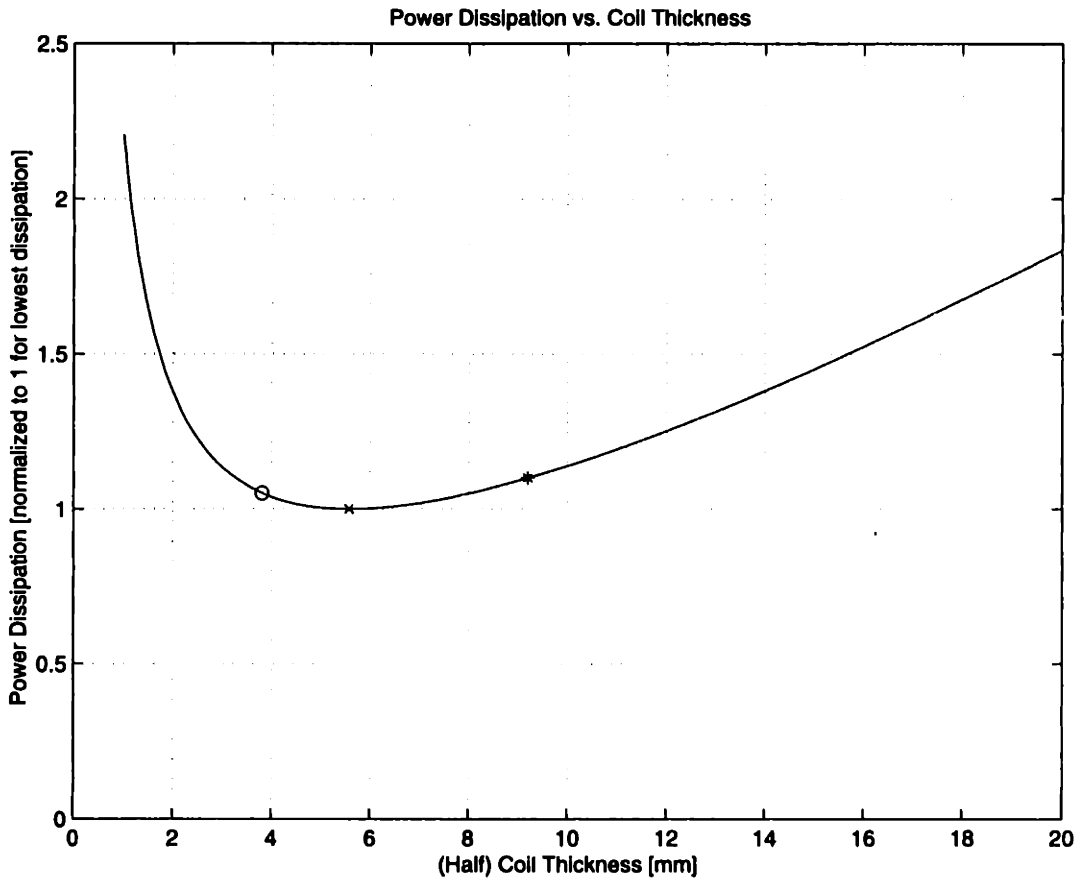

Figure 2-5: The power dissipated as a function of coil half-thickness is plotted. The power is normalized to 1.0 for the minimum power dissipation. This minimum occurs at a coil half-thickness of 5.57 mm and is marked by an X. The operating point of our motor is marked by an O. A thick coil which dissipates 10% more power than the minimum power level is marked by a *.

2.6.2 Coil Thickness Selection

While the power optimal result of Figure 2-5 is important, one misses a lot of design alternatives by focusing solely on this single value. The most useful way to think about this is to define a tolerance on the power dissipated. For example, we might consider coil thicknesses that dissipate no more than 10% more than the minimum power dissipation level. In our motor design that translates into an acceptable coil half-thickness range from 3.27–9.2 mm. Note that the acceptable range is quite large. In conventional coil designs, we have already shown that the temperature difference across the coil goes as the thickness squared. Thus, one would want to choose the thinnest half-coil, in this case, 3.27 cm.

In our separated end-turn cooling scheme, however, coil thickness is largely irrelevant. Now, we want to choose the thickest coil in our acceptable range defined by power dissipation. We do this because Figure 2-5 is a plot of power dissipated for the same force. If we are producing the same force with a thicker coil, the current density must be smaller than it would be for a thin coil. Hence, we can probably increase the current density in the thicker coil until we again reach the limit of our cooling system. This results in a much greater thermally-limited force (on the order of double) for only a slight increase in the volume of our motor. The thick coil case is marked with a "*" in Figure 2-5.

2.7 Force Constant Measurements

We now look at three different experimental ways to determine our motor's force constant. These include looking at the back EMF, measuring the force when a DC current flows through two phases, and measuring the force when a three phase amplifier is commanded to provide a constant force.

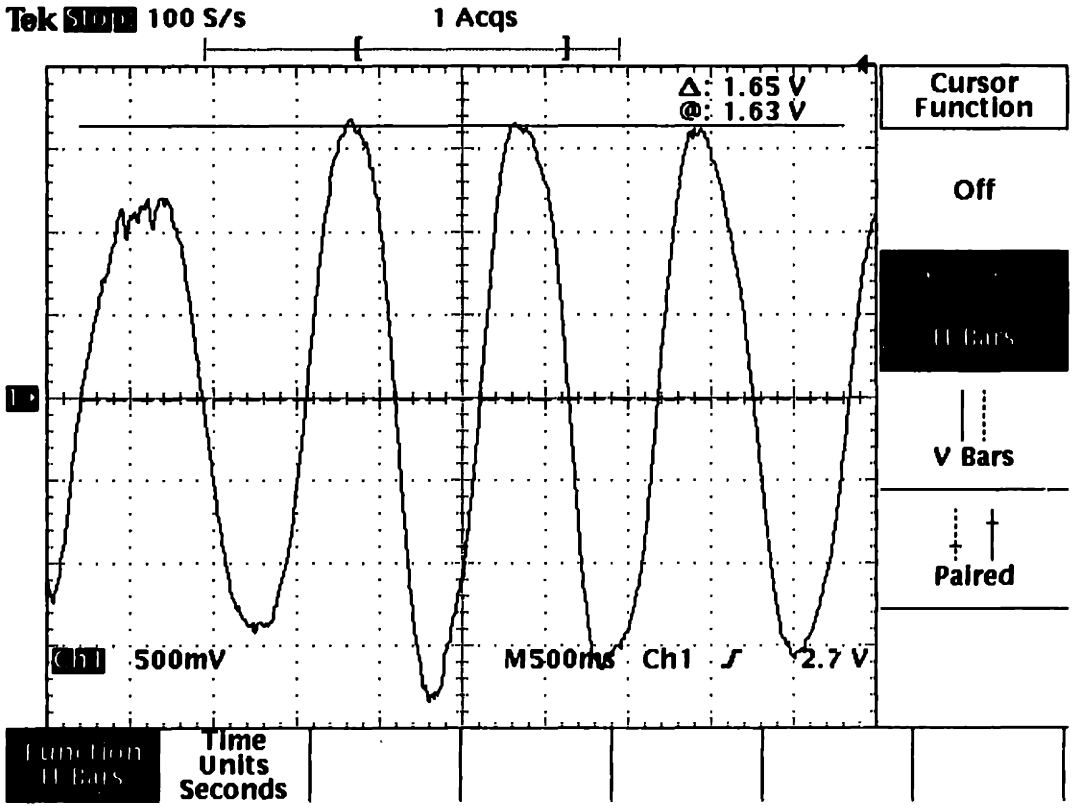

Figure 2-6: The phase-to-phase back EMF waveform shown is generated when the linear motor is moved by hand at a near-constant velocity.

2.7.1 Back EMF

The easiest force constant test is to look at a motor's back EMF. The back EMF waveform generated when the motor is moved by hand at a near-constant velocity is shown in Figure 2-6. The velocity can be found by measuring the period of the central cycles of the back EMF, $\tau = 1.05$ s, and knowing the wavelength of the magnet array, $l = 60$ mm. The zero-to-peak voltage is seen to be 1.65 V. Thus, the phase-to-neutral back EMF motor constant is

$$K_e = \frac{\frac{1.65}{\sqrt{2}\sqrt{3}}\text{V}}{0.0571 \text{ m/s}} = 11.80 \frac{\text{V}_{\text{rms}}}{\text{m/s}}, \tag{2.62}$$

where the factor of $\sqrt{3}$ converts from phase-to-phase to phase-to-neutral voltage and the factor of $\sqrt{2}$ converts from peak to rms voltage. In SI units, the force constant is equal to the back EMF constant, so the three phase force constant is three times the

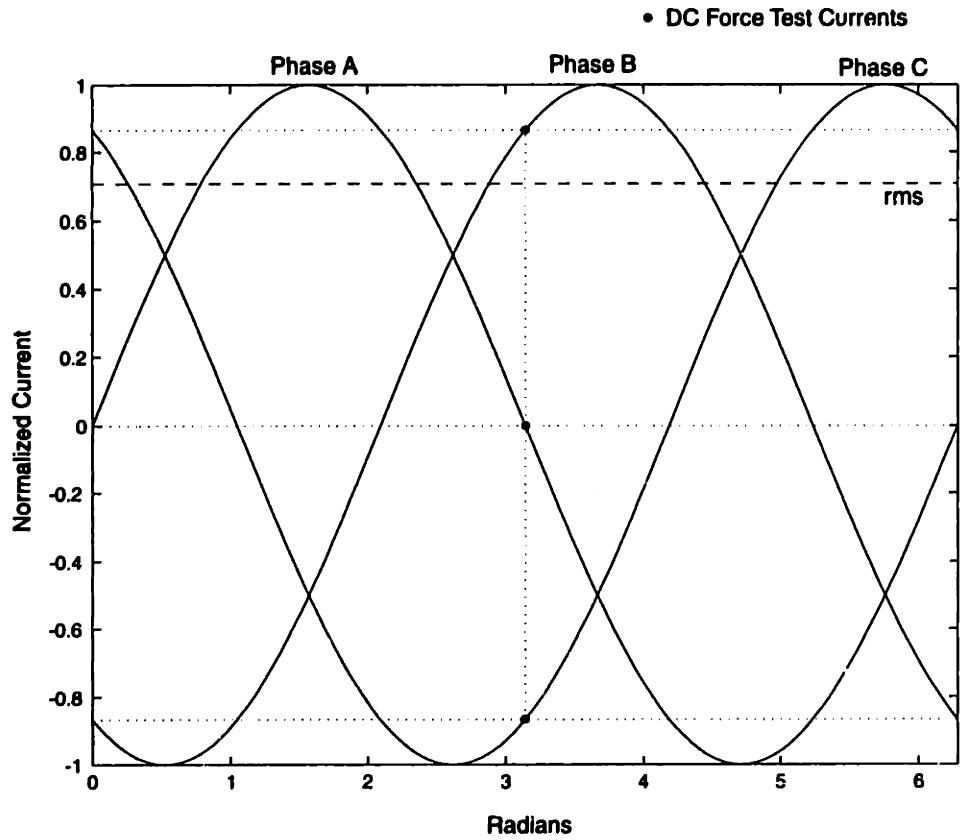

Figure 2-7: Balanced three phase currents are shown. A DC current applied across motor phases BC is shown by the dots. Note that phases B and C have equal but opposite currents while phase A has no current. The rms value of the three phase currents is less than the DC current applied by a factor of $\sqrt{2}/\sqrt{3} = 0.816$.

phase-to-neutral back EMF constant,

$$K_f = 3K_e = 35.4 \frac{\mathrm{N}}{\mathrm{A_{rms}}}. \tag{2.63}$$

2.7.2 DC Current Force Test

This method uses a DC current applied across two motor phases to measure the force constant. The reason why this works is illustrated in Figure 2-7. We see from Figure 2-7 that the DC current is equivalent to $\sqrt{3}/2$ of the peak current. Also, the rms current is $1/\sqrt{2}$ of the peak current. Therefore, a factor of $\sqrt{2}/\sqrt{3} = 0.816$ will convert the DC amps into a 3-phase rms value. The 3-phase rms value is just the rms

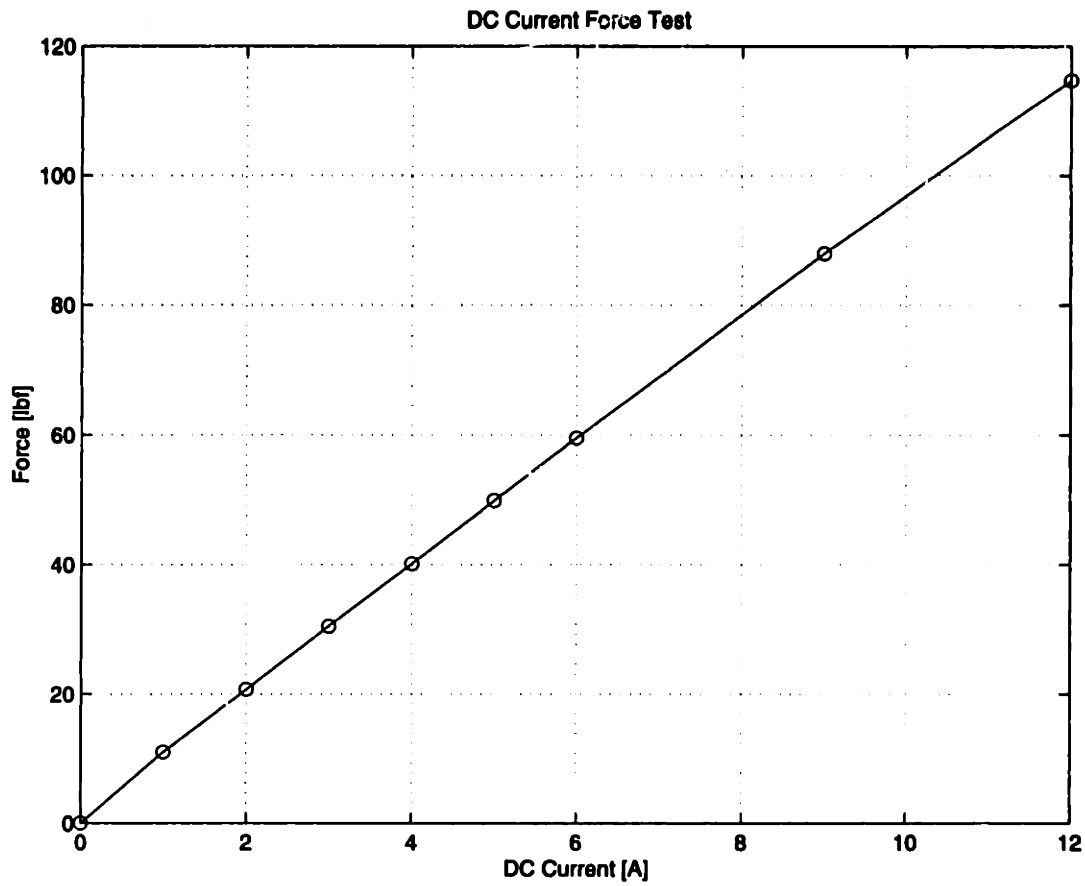

Figure 2-8: The results of a DC current force test are shown.

value of the individual currents.

The DC current force test is conducted as follows. A small DC current is passed through the two phases, and the motor quickly moves to a detent position with no resulting net force. Then the coil assembly is moved one-quarter motor pitch length to a position of maximum force. A load cell is used to measure the force when the coil is in this position with a DC current excitation in two phases. The results of this force test are shown in Figure 2-8. The force is quite linear as we expect, and the slope of the force vs. current plot is the force constant,

$$K_f = 9.7 \frac{\text{lbf}}{\text{A}_{\text{DC}}} = 35.2 \frac{\text{N}}{\text{A}_{\text{rms}}}, \tag{2.64}$$

where we have multiplied by the conversion factor $\sqrt{2}/\sqrt{3}$ to convert DC amps into

amps rms, as explained above.

2.7.3 Alternate Force Test

It should also be possible to measure the force constant in a commutated motor with Hall effect feedback just by measuring the force when a constant current is commanded to the 3-phase motor drive electronics. The *ABS I* pin on the Anorad sine hall amplifier [2] provides a measure of the amplifier's rms current output at any given time. A model 9212 Kistler Load Cell is used to measure force. This piezoelectric device produces 51.85 pC per 1 lbf and has a load capacity of 5000 lbf. A Kistler Dual Mode Amplifier with a long time constant was used to measure the charge produced by the load cell. The load cell is mounted to the backside of one of the L-shaped hard stops which is turned around for the force test. The load cell is fixtured to this stop via a double-ended screw. The setup for the force test is shown in Figure 2-9. The results of this force test are shown in Figure 2-10. Again, the data is linear and yields a force constant,

$$K_f = 7.56 \frac{\text{lbf}}{\text{A}_{\text{rms}}} = 33.6 \frac{\text{N}}{\text{A}_{\text{rms}}}, \tag{2.65}$$

which is very close to the ones calculated by the other methods.

The values of K_f computed by the back EMF, DC current force test, and alternate force test are 35.4, 35.2, and 33.6 N/A_{rms}. All three tests are in excellent agreement and close to the analytical value of 39.69 N/A_{rms}. With a solid analytical and experimental understanding of the motor electromechanics in hand, we turn, in the next chapter, to the motor configuration design issues.

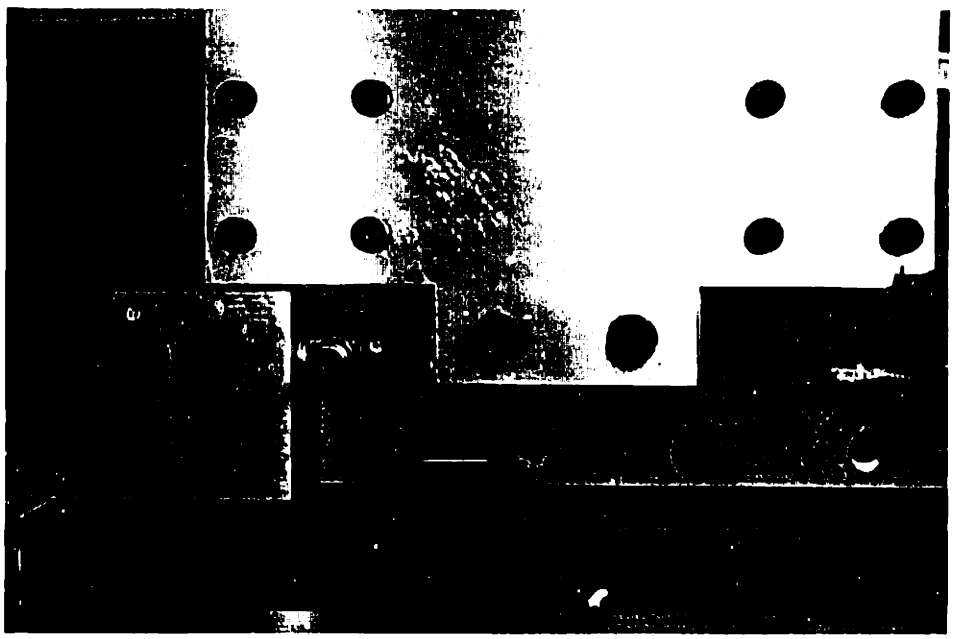

Figure 2-9: The setup for using the Kistler piezoelectric load cell is shown. The load cell is securely fastened to the back of a hard stop that has been temporarily turned around. The other side of the load cell has a silicon carbide hemisphere screwed into it. The removable motor stop is placed next to the hemisphere and pushes on it during the force test.

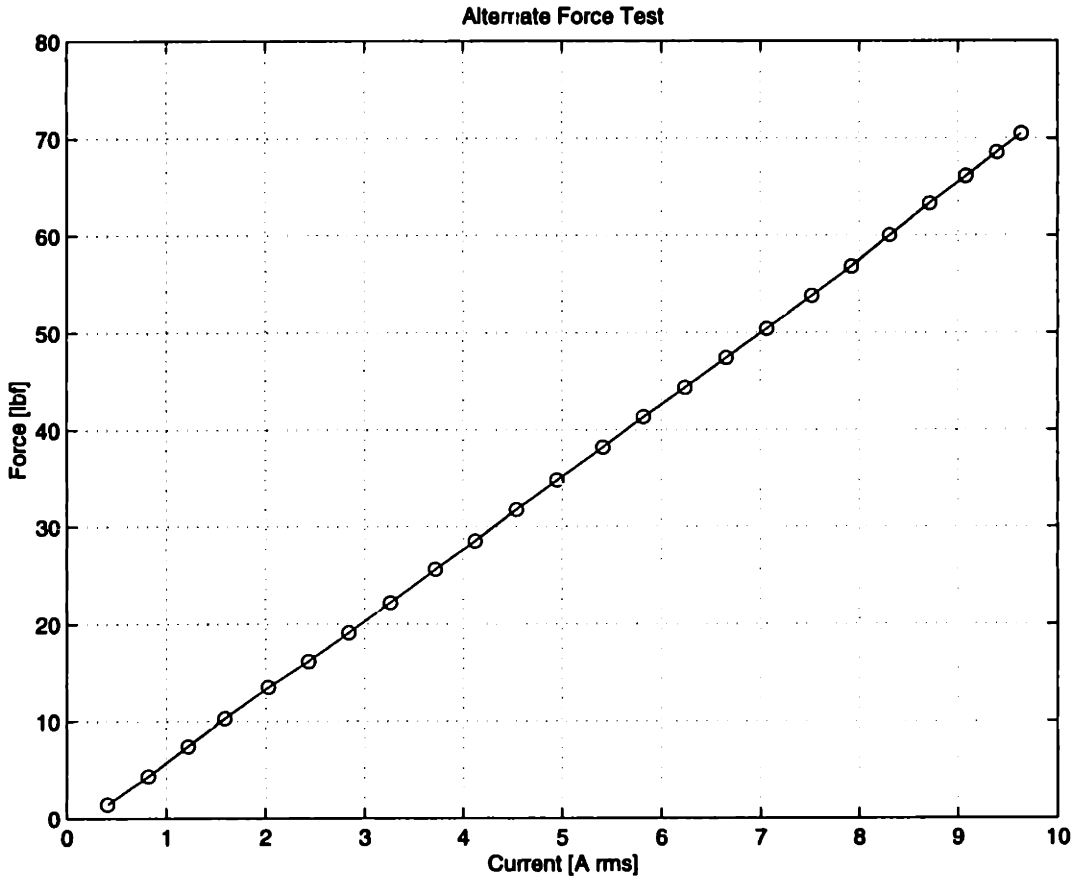

Figure 2-10: The results of a force test performed with a sine hall amplifier commutating the motor are shown.

Chapter 3

Conceptual Designs

This chapter presents a number of design ideas for the coils and magnet array. Significant insight can be gained by considering the relative advantages and disadvantages of the various designs. Some designs that were not chosen for our prototype motor may be useful in other applications with different performance goals.

3.1 Coil Design

A surface-wound permanent magnet motor produces force when current flows through a wire in a magnetic field. A coil of wire is an efficient way of grouping many turns of wire in a motor. Coils generate heat when current flows through them since they have some finite resistance. This effect is known as Joule or I^2R heating, where I [A] is the current flowing through the coil, R [Ω] is its resistance, and I^2R is the power dissipated. The resulting heating imposes a practical limit on the amount of current which can flow through a coil before a motor exceeds its operating temperature limit. A coil which can withstand a higher current before becoming unacceptably hot results in a motor capable of producing more force for the same volume of motor.

A good coil design will incorporate a cooling method which allows the coil to attain high current densities J [A/m^2] before getting too hot. We first present a list of functional requirements for our thermally efficient coil. Then we examine traditional coils and some cooling techniques that have been used with them. From

this discussion we develop a key rule in thermally-efficient coil design: It is difficult to cool through multiple layers of wire. This leads us to consider edgewound and flatwound coil designs. These are both viable designs that are useful under certain conditions. Next we introduce the separated end-turn coil which is the design we eventually chose for our linear motor. These special coils can be cooled through the length of the windings via direct liquid cooling or through a technique named "comb" cooling. We have adopted the direct liquid cooling technique in our prototype motor, but the comb cooling method also delivers promising results.

3.1.1 Functional Requirements

We would like our coil designs to achieve the following goals:

- Current density for the wire cross-section greater than 10^7 A/m^2 and as high as possible.[1] Other motors usually operate at a thermally-limited current density of about 5×10^6 A/m^2. Force is proportional to current density, but the heat generated is proportional to current density squared.

- Coil half-thickness greater than 3 mm. The optimum coil thickness depends mainly on the magnet pitch. For our magnet pitch, a coil half-thickness below 3 mm would cause the motor to be unacceptably power inefficient. With conventional cooling techniques, it is harder to cool a thicker coil because the heat has to cross more layers to reach the surface. With our cooling technique, each turn of the coil is in direct contact with the coolant so the coil thickness is not a problem.

- Maximum average temperature rise of 100°C. Depending on the grade of magnets used, this limit can be higher or lower. There is a distinction between average temperature rise in a coil as measured by the terminal resistance increase and the temperature rise as a function of position within the coil.

[1] Eventually, we must consider the possibility of demagnetizing the magnets if the currents get too high.

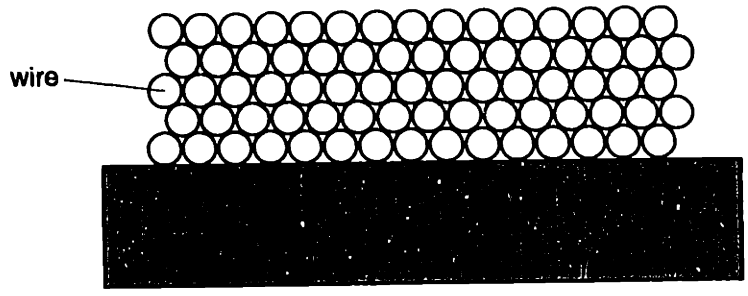

Figure 3-1: Here is a cross-section of a conventional coil wound with round magnet wire. Notice the pockets of air surrounding the wires and the limited contact area between them.

- Easy to manufacture and implement. No matter how well a design performs, it won't be useful if we can't make it affordably and easily.
- Compatible with iron core motors as well as epoxy core U-channel motors.

3.1.2 Conventional Coil

Here we consider a conventional coil of wire consisting of several layers of circular magnet wire. Such coils are commonly cooled either by surrounding air, cooling from the center [4], or cooling from an end-turn. In all of these methods and other common ones, the cooling medium only directly contacts the outermost or innermost layer of wires in the coil. The heat generated by the many interior layers of the coil cannot easily escape. It must travel across layers of the coil until it reaches the cooling medium. The thermal resistance across coil layers is often substantial, leading to unacceptably high temperature gradients in the coil [4].

Figure 3-1 shows a cross-section of a conventional coil surface wound on a backing layer. The air voids between layers in a coil are good thermal insulators. Often there is little contact area between the cylindrical wires stacked in a coil. These factors tend to make the thermal resistance across coil layers the dominant resistance in coils. A significant improvement in thermal conductivity can be obtained by impregnating the coil with a thermally conductive epoxy or varnish. The epoxy also gives strength to the coil and can protect the coil from dirt and nicks. The thermal conductivity

of these epoxies and varnishes is much better than air but well below that of copper. Ofori-Tenkorang [27] models the ensemble of epoxy with wires in it with one effective thermal conductivity. It is then straightforward to use finite-element analysis or simple thermal equations to analyze the temperature distributions. The difficulty lies in computing an accurate effective value. Torquato and Lado [32] compute upper and lower bounds on the effective conductivity of a composite material with randomly distributed cylindrical wires. At volume fractions of 90% copper, the upper bound is more than ten times greater than the lower bound. This leaves a lot of uncertainty in the value of this crucial parameter. Berhan [4] experimentally measured the effective thermal conductivity for an unpotted coil and found it to be very small. Instead of using a composite thermal conductivity, we focus on the limiting thermal conductivity—caused by either air gaps or epoxy—and separate the coil into layers, as the thermal resistance across coil layers is the biggest problem in conventional coils.

3.1.2.1 Layered Thermal Model

In this section, we develop a generic model for conventional coils where the thermal resistance between layers is the dominant factor. Our model makes the following assumptions:

- The heat flow is one dimensional.
- The thermal resistance within a layer is negligible. This is a very good assumption because copper has a high thermal conductivity. Thus, each layer has a uniform temperature.
- The low thermal conductivities of the wire insulation and epoxy in between the wires are lumped into an average thermal resistance R [K/W] which exists between coil layers.
- We do not model radiation or convection—only conduction.

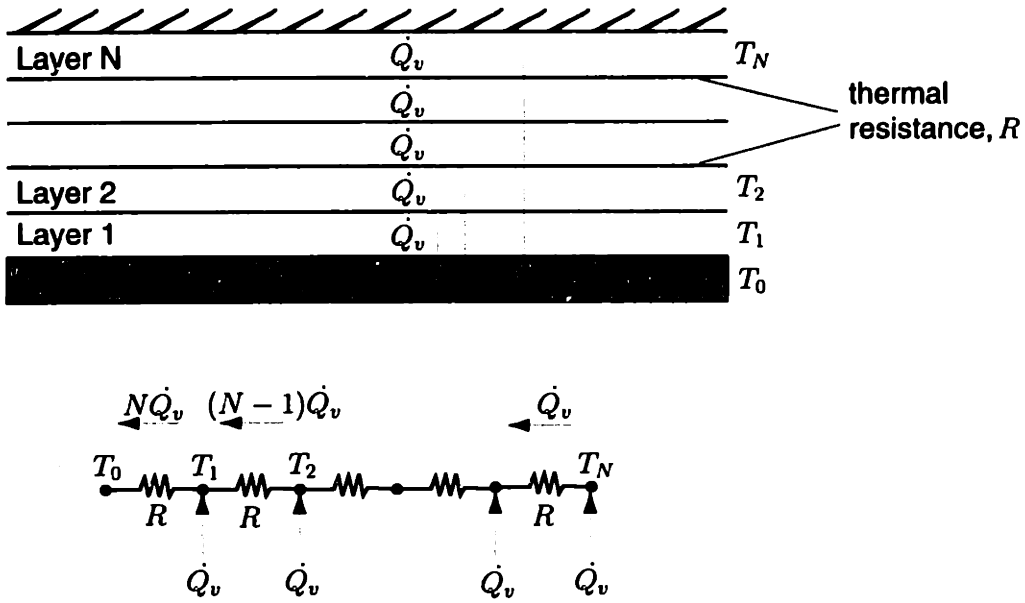

Figure 3-2: Conventional cooling techniques can be modeled as cooling a stack of coil layers. Each layer internally generates heat at a rate $\dot{Q}_v$ and is separated from its neighbors by a thermal resistance R. The top surface is adiabatic and all heat must flow toward the bottom marked "COOLING." An equivalent resistor model of the heat flow is also shown.

- We assume the top layer is adiabatic. In reality there may be some heat loss via natural convection and radiation, but the conduction heat flow will be the dominant mode of heat removal.

All of the conventional cooling techniques can be modeled in one dimension as shown in Figure 3-2. Each of N layers generates heat at a rate $\dot{Q}_v$ [W] due to Joule heating. The subscript v signifies that the heat is generated in the volume of the layer. Each layer is separated from its neighbors by a thermal resistance R [K/W]. All heat is conducted to the side marked "COOLING." Thus, the heat $\dot{Q}_v$ generated in layer N flows across thermal resistance R to layer $N-1$. This heat and the heat generated in layer $N-1$, a total of $2\dot{Q}_v$ now flows across thermal resistance R to layer $N-2$, and so forth until the heat generated in all N layers, $N\dot{Q}_v$, flows across the last layer to the cooling medium at temperature T_0. This reasoning yields a set

of equations describing the temperature differences across each layer,

$$\begin{aligned} T_1 &= T_0 + N\dot{Q}_v R \\ T_2 &= T_1 + (N-1)\dot{Q}_v R \\ &\vdots \\ T_N &= T_{N-1} + \dot{Q}_v R, \end{aligned} \tag{3.1}$$

which can be solved as

$$T_N = T_0 + \dot{Q}_v R\left(\frac{N^2+N}{2}\right). \tag{3.2}$$

Equation (3.2) shows that the temperature difference across N layers goes as N^2+N for a given inter-layer thermal resistance R and heat generation rate per layer $\dot{Q}_v$. We see that the temperature difference across the coil thus varies quadratically with the number of layers in the coil. It also varies quadratically with the current I since $\dot{Q}_v \propto I^2$.

This simple analysis provides the basis for all the designs which follow. Namely, *it is hard to cool through multiple layers of wire.* One improvement is to use a larger gauge wire, e. g. use 17 gauge instead of 23 gauge. This will cut down the number of layers and therefore increase the maximum current density for a given temperature rise. The drawback to this solution is that it requires a high-current power amplifier to maintain the same current density as before in the larger cross-section wire. Besides, this is only a partial solution because even if we can use a larger gauge wire, we still are cooling through many layers.

We really want to cool each layer of the coil directly. The following designs present different ways of doing just that.

3.1.3 Edgewound Coil

An edgewound coil is made from wire of rectangular cross-section wound on its short side in a single layer as shown in Figure 3-3. The thermal advantage of such a coil is clear in light of the previous section: there is only one layer. The backing plate

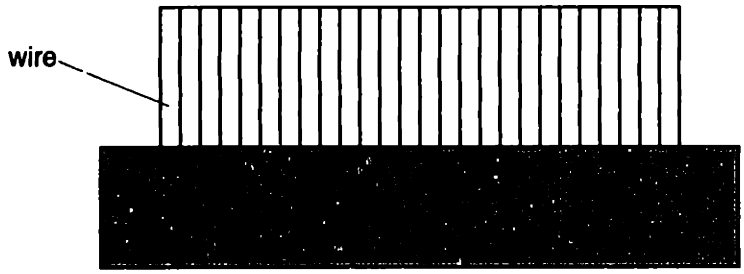

Figure 3-3: Here is a cross-section of an edgewound coil wound with rectangular cross-section magnet wire. Each wire directly touches the backing plate.

can absorb heat directly from each turn of the coil, and the surface area available for this transfer is large. The thermal resistance of copper through the cross-section of the wire is negligible compared to the thermal resistance of the insulation between the wire and the stator. Thus, we have a fixed thermal resistance R no matter how thick t the coil is. The heat generated for a fixed current density will depend only on the volume of the coil, i.e., linearly on the thickness t. Since $\Delta T = \dot{Q}_v R$, we have $\Delta T \propto t$. This is a significant improvement over the conventional coil of the previous section where we concluded that $\Delta T \propto N^2$ or since the number of layers N is directly proportional to the thickness, $\Delta T \propto t^2$.

Unfortunately edgewound coils have some disadvantages:

- Several wire vendors quote a maximum ratio for the long to short side of the cross-section as 10:1. Thus, the cross-sectional area becomes quite large for coil thicknesses greater than 3 mm. In order to attain high current densities in these large cross-section wires, we need expensive high-current power amplifiers.

- It is not easy to wind edge-wound coils. Only certain wire winders have experience winding them. Also, special attention must be given to running the wire leads as they are rectangular.

- It is more difficult to obtain edgewound wires than regular round ones because they are typically custom-made. For full-scale production, this would probably not pose a problem, but it is difficult to find suppliers for prototype windings at affordable prices.

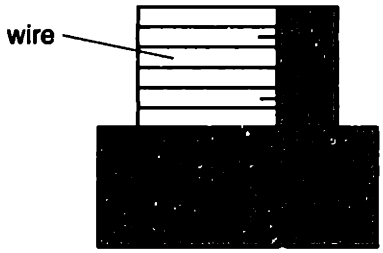

Figure 3-4: A cross-section of a flatwound coil is shown. Each layer can be directly cooled from the side as shown.

While we did not adopt such a coil, edge-wound coils should certainly be considered for applications with coil thicknesses under 3 mm.

3.1.4 Flatwound Coil

A flatwound coil is made of the same rectangular wire used for an edgewound coil but is wound on the long, flat side rather than the edge. Thus a flatwound coil will have many layers since each layer is thin. In order to efficiently cool such a coil we would *not* want to cool through all these layers. However, we can cool each layer directly from the side as shown in Figure 3-4. The idea is the same as for an edge-wound coil except that now we are cooling from the side of the coil rather than from the inside.

A practical implementation of this type of cooling is the "staircase" cooling scheme shown in Figure 3-5. The end-turns of several flatwound coils are staggered such that each one is in contact with a "step" on the staircase-shaped piece of metal which is itself directly cooled. Such a staircase should be made of copper so that its thermal expansion matches that of the coils to which it is attached.

The disadvantages associated with flatwound coils are similar to those just mentioned for edgewound coils, in that they require high-current power amplifiers, and the wire is more difficult to obtain. It is, however, easier to wind flatwound coils than edge-wound coils since the wire is not standing on end.

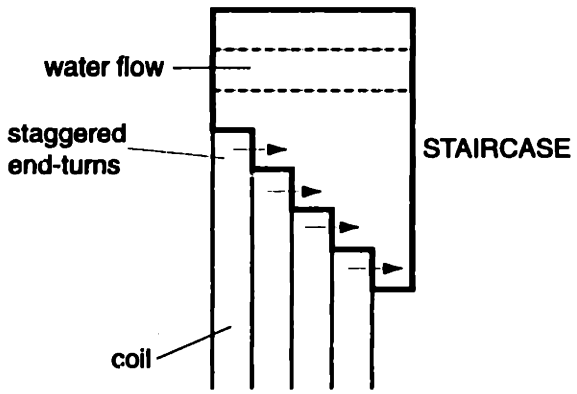

Figure 3-5: The staircase cooling scheme removes heat from the sides of the end-turns of flatwound coils. The coils are staggered so that each wire makes contact with the staircase shaped piece of copper.

3.1.5 Separated End-Turn Coil

We now return to thinking about conventional coils wound with round magnet wire. We must find a way to cool each layer of the coil directly. In order to do this, we must have access to each layer. This can be accomplished by leaving gaps between the end-turns of the coil as was shown in Figure 1-1. We have labeled this new type of coil design a "separated end-turn coil." The long section of the coil is a conventional compact arrangement of circular wires and is used to produce force in the motor. The end-turns are separated into individual layers so that each can be directly cooled. These special coils are fabricated by sticking pins into the bobbin during the winding process. These pins separate successive end-turn layers from each other with a small air gap.

There are two main methods by which a separated end-turn coil can be cooled. The first consists of flowing liquid directly through the gaps in the end-turns. Thus, the end-turns lose heat via forced convection of a fluid such as air, water, or oil. The second method consists of inserting copper shims into the gaps in the end turns and cooling these shims. Here we focus on the direct liquid cooling of the separated end-turns. The second method is presented in detail in Chapter 8.

3.1.5.1 Choice of Coolant

We can flow either water or oil past the end-turns. From a thermal point of view, water is the clear winner. It has twice the heat capacity of oil and 4.5 times the thermal conductivity. The higher heat capacity of water means that a water-cooled coil needs only half the flowrate of coolant as an oil-cooled coil to carry away the same amount of heat at a given temperature rise. The higher thermal conductivity of water means that the convective heat transfer from the end-turns to the liquid will be better, resulting in a smaller temperature rise in the end-turns. Also, water is less viscous than oil so it is easier to develop a turbulent flow which has improved heat transfer over a laminar flow. Despite these advantages, we have chosen oil for our prototype because of the hazards of running water directly over electrical coils. Over time, water can seep into pinholes in the coil insulation creating corrosion or a short circuit. This is unacceptable in a motor, so we are forced to use oil instead. For some initial tests, we use water as a coolant because it is easier to work with.

3.1.5.2 Coil Sizing

In section 4.1.1 the detailed thermal model for a separated end-turn coil is presented. Here we want to develop an intuitive feel for the coil design. A key point in the thermal model is dividing the temperature rise in the coil into two parts. The first part deals with the temperature rise from the cooled end-turns to the main working part of the coil. The second part looks at the temperature rise from the coolant liquid to the end-turns. We have a lot of control over the second temperature rise: We can adjust the length of the end-turns, the number of end-turns, the gaps between the end-turns, the type of coolant, and the velocity of coolant. The temperature rise from the end-turns to the middle of the coil is essentially fixed by the current density and the length of the coil. Thus, if our coil is too long, it won't matter that we have an efficient cooling system on the end-turns, because the temperature rise along the coil will be too large.

3.1.5.3 Gap Size

The size of the gap between separated end-turns is a critical design parameter. We consider three issues below:

1. If the gap is too large, the end-turns are larger and thus become a significant part of the length of the coil. This is bad because power dissipated in the end-turns does not generate a corresponding force. Also, a larger gap increases the length of the outer coils which thereby increases the temperature differences along the coil.

2. Although it may seem counterintuitive, a smaller gap increases the heat transfer from the end-turns to the coolant. Tube flows have a velocity boundary layer in which the velocity varies from the fast freestream velocity to zero velocity for the fluid in contact with the tube wall. Likewise, a thermal boundary layer exists in tube flows where the temperature varies from the free-stream temperature to the wall temperature [18]. At the wall, there is no fluid motion so the rate of heat transfer between the wall and fluid is governed by conduction and depends on the temperature gradient at the wall, $\partial T/\partial y|_{y=0}$, where y measures distance perpendicular to the wall surface. As the thermal boundary layer grows, this gradient decreases, and the heat transfer decreases. The flow is said to be fully thermally developed when the thermal boundary layer thickness equals half the diameter of the tube. A smaller diameter tube forces the thermal boundary layer to be smaller which makes the temperature gradient $\partial T/\partial y|_{y=0}$ larger, and this increases the heat transfer.

3. We need to have a certain flow-rate of liquid through the end-turns to carry away all the heat generated in the coil. If we make the end-turn gaps very small, we will be required to have a much higher pressure to achieve the same flowrate. We have a Poiseuille flow in this region, and the pressure is inversely proportional to the fourth power of the gap.

Issues 1 and 2 argue for the smallest gap size possible to keep the end-turns small and improve heat transfer. Issue 3 places a limit on the smallest size gap because we simply won't be able to pump enough coolant through it with a normal pump. Because we have 22 layers in the coil in the prototype motor, issue 1 was a potential problem even with a small gap size. We realized that we could further reduce the size of the end-turns by separating the layers into groups of twos. This still allowed each wire to touch the coolant (groups of threes would not work since it would bury the middle layer) and yet decreases the size of the end-turns.

3.1.5.4 Single vs. Double Sided Cooling

A single sided separated end-turn coil has one end-turn normal (packed tight) and one end-turn separated as shown in Figure 3-6. A double sided coil has both end-turns separated. Cooling from both sides is often much better than cooling from only one. The level of improvement depends on whether the temperature difference is mostly along the length of the coil or across the end-turns. In the limiting case where most of the temperature drop occurs along the length of the coil, double-sided cooling doubles the current which can be put through the coil for the same total temperature rise. Our coil geometry is close to this condition so we designed for double-sided cooling.

3.2 Magnet Array Design

3.2.1 Ironless Magnet Arrays

We considered five different magnet arrays for our motor which are shown in Figure 3-7. Magnet array (A) is the conventional N-S array without back iron. It produces the same magnetic field on both sides which can be a problem when the motor is used in a machine tool. Array (B) is a four-block Halbach array which has a strong and weak side. The strong side has a magnetic field that is $\sqrt{2}$ times stronger than a conventional N-S array. This array is useful since the field inside the motor is strengthened resulting in increased force, and the field outside the motor is reduced.

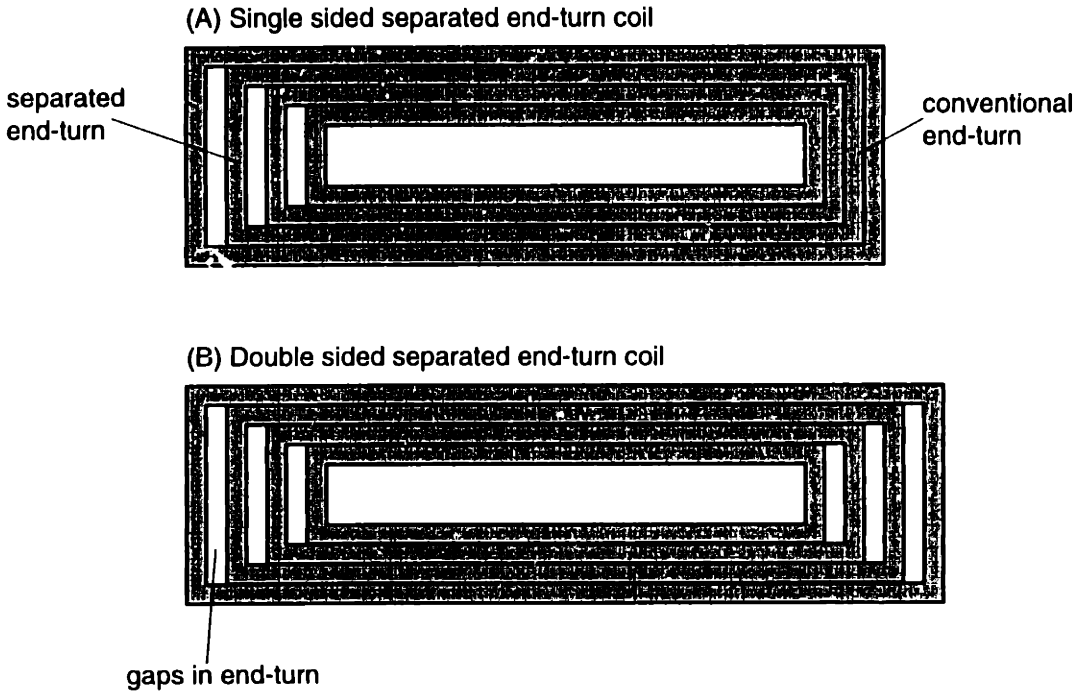

Figure 3-6: A single-sided separated end-turn coil has one end-turn packed tight and one end-turn eparated. A double-sided separated end-turn coil has both end-turns separated.

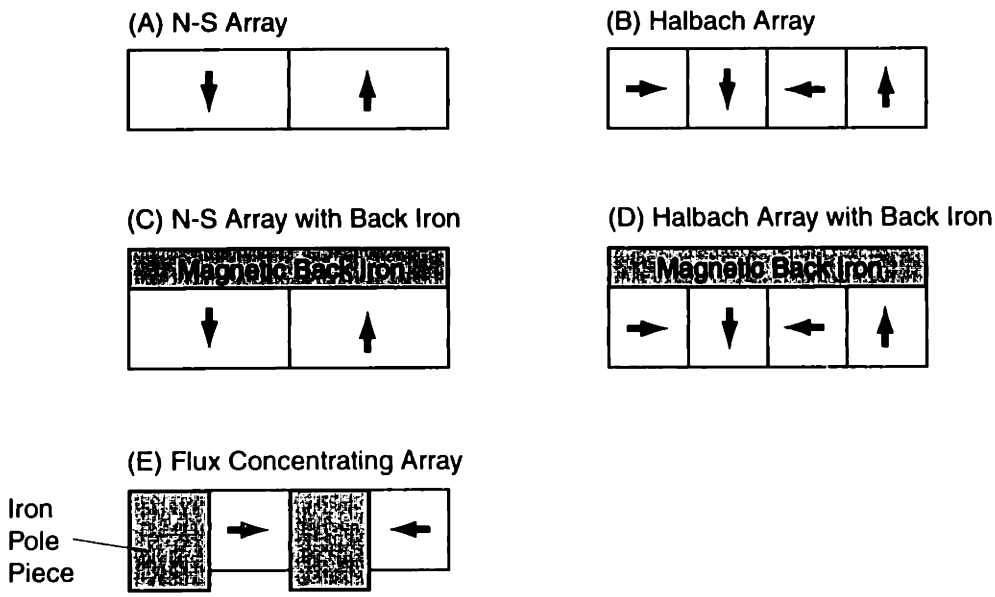

Figure 3-7: Five different magnet arrays are shown.

It has successfully been used in linear motors built by Kim [20] and Williams [37]. Its main disadvantage is that it is more difficult to fabricate than conventional N-S arrays [4]. The ironless Halbach array always produces a stronger magnetic field than the ironless N-S array. Halbach arrays also produce less force ripple than N-S arrays since they don't have third harmonics on the strong side.

3.2.2 Magnet Arrays with Back Iron

Next we consider arrays (C) and (D) which are the same as arrays (A) and (B) except for the addition of magnetic back iron. The iron behind the conventional N-S array (C) has the same effect as doubling the thickness of the magnets. It will have the biggest effect on the force when the magnet array is thin and less effect when the magnets are thick. It is not as straightforward to predict the benefit of placing iron behind a Halbach array such as array (D). The magnets with magnetization perpendicular to the iron backing will be doubled just like before. However, magnets with magnetization parallel to the iron backing will have their mirror image pointing opposite from the actual magnet. The iron backing acts to reduce the motor force for these parallel magnets. Thus, adding iron is good for normal magnets and bad for parallel ones. The effect of adding iron to a Halbach array therefore depends strongly on its thickness. It will not help much for thin arrays but will improve thicker arrays. John Ofori-Tenkorang examined these issues in his thesis and found that for thin arrays an iron-backed N-S array can actually be better than an iron-backed Halbach array [27]. For a typical linear motor size, the iron-backed Halbach array (D) offered only a 20% improvement in field strength over the iron-backed N-S array (C). We therefore decided to use the iron-backed N-S array since it is easier to fabricate.

3.2.3 Flux Concentrating Magnet Array

The fifth array (E) is different from the first four because it contains iron pole pieces as part of the array. The magnetic flux from the parallel magnets is channeled through the pole pieces across the coils to the coil back iron. It can be modeled as a magnetic

circuit [10]. The name, "flux concentrating," comes from the fact that the magnetic field generated outside the array can be made larger than the remanence of the permanent magnet by making the area of the pole piece much smaller than the contact area between the pole piece and magnet.[2] While this array can produce high magnetic fields with narrow pole pieces, these fields exist only under the pole pieces which is a fraction of the coil volume. We want to optimize the force produced and this requires consideration of the amount of coil exposed to the magnetic field. When this is done, using a magnetic circuit analysis and $\mathbf{F} = \mathbf{J} \times \mathbf{B}$ force calculation, the optimal result is that the pole piece should take up half the magnet array (as shown in Figure 3-7. This design produces less force than the iron-backed arrays (C) and (D) but more force than the ironless arrays (A) and (B). It has two main advantages over the other arrays:

1. The iron pole pieces can be shaped much more easily than magnets can be. For example, a tubular magnet array was fabricated in a octahedral pattern by Berhan [4] to approximate a circular magnet. It would be much easier to make a piece of iron with a circular hole in it to achieve the ideal fit.

2. The flux concentrating array has the highest force per volume of magnets compared with the other four arrays we are considering: it has half the magnets of the other arrays but produces more than half the force that they do.

With the coil and magnet design options expressed, in the next chapter we turn our attention to modeling the coil thermal performance.

[2]The field also depends on the ratio of the length of the magnet to the gap between the pole piece and coil back iron.

Chapter 4

Thermal Model

This chapter presents the thermal model used to analyze and design the liquid cooled separated end-turn coils in our motor. After the model is described, we illustrate its use with a detailed example. We recommend Mills's book on heat transfer [26] for the reader who wants to add a basic heat transfer text to his library. It contains the essential theory and complete reference tables listing material properties. Another popular book is written by Incropera and DeWitt [18].

4.1 Liquid Cooled Separated End-Turn Coil

A schematic of the final coil design is shown in Figure 4-1. The most important feature of this coil is its separated end-turns. By leaving gaps between the end-turns, we can directly cool each layer of the coil. This has strong advantages over conventional

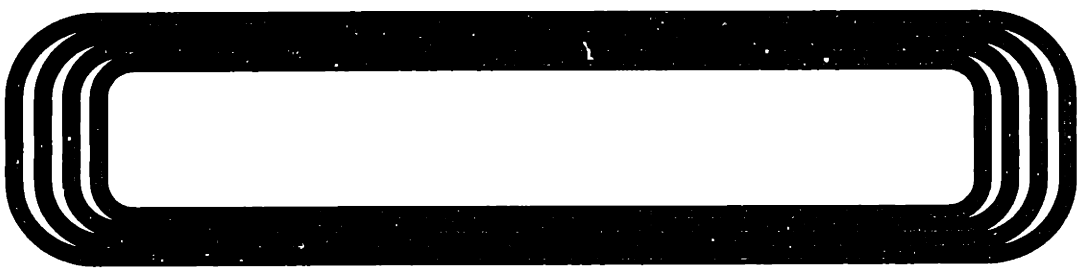

Figure 4-1: A schematic of the final coil design is shown. Cooling fluid flows into the page through the separated end-turns.

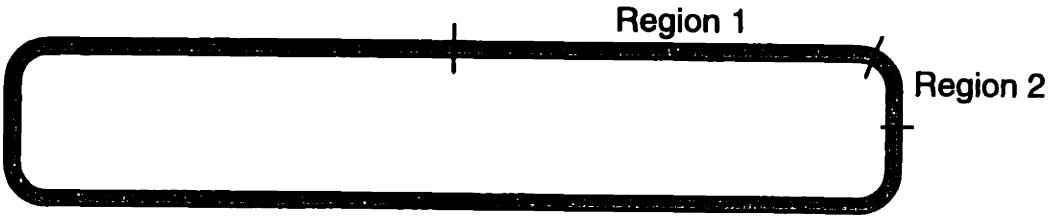

Figure 4-2: A single layer of a coil cooled on both end-turns is shown. The coil can be broken into symmetric quarters. A quarter coil is further divided into two regions as shown. In Region 1 there is only Joule heating. In Region 2 there is convective cooling by a liquid flowing across the end-turns in addition to Joule heating.

cooling schemes in which only the outermost layers are cooled. In these conventional schemes, the thermal resistance between coil layers is substantial, and this leads to a large temperature gradient across the coil layers. In our design we remove the heat from each layer directly and are no longer limited by the large inter-layer thermal resistance.

In this chapter we develop the thermal model for a separated end-turn coil. Separated end-turn coils can be wound easily by placing pins into the bobbin between coil layers during winding. The cooling fluid flows into the page through the channels in the end-turns shown in Figure 4-1. Thus each wire of each layer is in contact with the flowing cooling liquid at the end-turns.

4.1.1 Thermal Model

A single layer of the separated end-turn coil is shown in Figure 4-2. Both end-turns are cooled, and symmetry thus allows us to consider one-quarter of the coil. The endpoints of this quarter coil segment are located at the middle of the long side of the coil and at the middle of the end-turn. The first endpoint is the hottest point on the coil and the second is the coolest; both are adiabatic (no heat flow through them) due to the symmetrical geometry of the coil and applied boundary conditions.

Heat is generated uniformly in the coil by Joule heating. In our one-dimensional thermal model this heat flows along the coil until it reaches the end turn. At the end turn, the heat is conducted through the coatings on the wire and convected away

by flowing liquid. In reality, there are several additional paths by which the heat can escape, but these are negligible compared to the dominant path we have just identified. In all cases these additional paths aid in the removal of heat so we are being conservative with our model by considering only the primary path—the removal of heat via the end-turns.

The quarter coil can be divided into two regions as shown in Figure 4-2:

- Region 1—Joule Heating.

  The left boundary is adiabatic and all the heat generated must flow towards Region 2.

- Region 2—Fin with Joule Heating.

  At the top boundary all the heat from Region 1 flows into Region 2. The bottom boundary is adiabatic. At the edges of Region 2 heat is convected away by flowing liquid.

The thermal model we are developing for a coil cooled on both end-turns is equally applicable to a coil cooled on only one end-turn. In this case, the coil divides into symmetric halves rather than quarters. Each half can further be broken into a Region 1 and a Region 2. Region 2 is the same size for coils cooled on either one or both ends. However, Region 1 is much longer—approximately double—for the coil cooled on only one side and extends to the middle of the opposite uncooled end-turn of the coil, which is the hot point.

We next look at theoretical predictions for the temperature distribution in each region.

4.1.2 Region 1 – Joule Heating

4.1.2.1 Simplified Model

In this section, we look at the temperature profile along a wire with Joule heating. Specifically, we consider a wire of length L in which one end is adiabatic and the other

end is held at a fixed temperature T_0. This model corresponds to Region 1 in Figure 4-2. This is a one-dimensional heat transfer problem: We assume the temperature variation across the wire cross-section is negligible, and the only variation occurs along the length of the wire. We neglect any convection or radiation from the edges of the wire in Region 1. Typically, a wire in Region 1 is surrounded by a densely packed array of other wires so this is a good approximation. The force produced by the motor is due to the Lorentz force between the magnets and the current flowing in Region 1 but not Region 2 (the end-turns of the coil).

We assume that the thermal conductivity k and the electrical conductivity σ of the wire are constant. For copper, the thermal conductivity hardly depends on temperature, but the electrical conductivity decreases significantly (approximately 25% for a 100°C rise). In the next section we will incorporate the temperature dependence of the electrical conductivity, but we will treat it here as a constant.

A diagram of the wire is shown in Figure 4-3. We consider a differential element of width Δx located a distance x from the left-hand side. The heat flux at a distance x is $q(x)$ [W/m^2]. We use Mills's notation [26] for the internal heat generation $\dot{Q}_v'''$ [W/m^3] in the wire. The subscript v indicates that the heat is generated inside a volume, and the triple prime indicates that it is per unit volume (per length cubed). The total heat generated in a volume V is $\dot{Q}_v = \int_V \dot{Q}_v''' dV$. The internal heat generation in a volume of wire due to Joule heating is

$$\dot{Q}_v''' = \frac{J^2}{\sigma} \tag{4.1}$$

where J [A/m^2] is the current density in the wire. The boundary conditions are as follows:

1. Constant Temperature: $T(x = 0) = T_0$
2. Adiabatic: $q(x = L) = -k \left.\frac{dT}{dx}\right|_{x=L} = 0$

We have used Fourier's Law in boundary condition number two.

There must be an energy balance for each differential element along the wire in

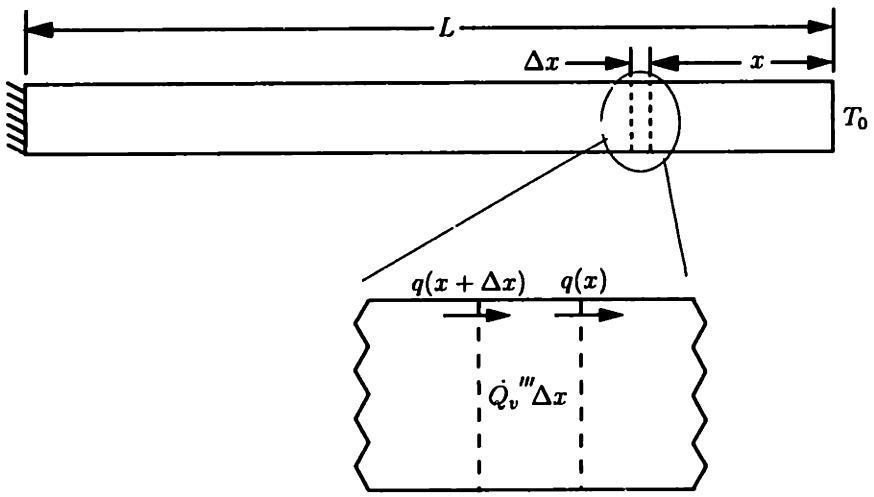

Figure 4-3: A one-dimensional heat conduction problem with Joule heating is shown. The energy balance for a differential element is depicted.

Figure 4-3. This equation expresses the energy balance per unit cross-sectional area of the wire:

$$q|_x - q|_{x+\Delta x} + \dot{Q}_v''' \Delta x = 0 \tag{4.2}$$

By dividing equation (4.2) by Δx and taking the limit as $\Delta x \rightarrow 0$ we arrive at a differential equation for the heat flux. We can then substitute for the heat flux using Fourier's Law, $q = -k\frac{dT}{dx}$, to arrive at the governing differential equation for the temperature variation:

$$\frac{d^2T}{dx^2} + \frac{\dot{Q}_v'''}{k} = 0 \tag{4.3}$$

The solution to equation (4.3) subject to the boundary conditions is:

$$T = \frac{-\dot{Q}_v'''}{2k}x^2 + \frac{\dot{Q}_v''' L}{k}x + T_0 \tag{4.4}$$

We see that the temperature distribution along the coil is parabolic. The maximum temperature occurs at the adiabatic end. It is useful to have an expression for this

maximum temperature, which is

$$T(L) = \frac{\dot{Q}_v''' L^2}{2k} + T_0. \tag{4.5}$$

Equation (4.5) gives us a scaling law for the maximum temperature rise in Region 1. The maximum temperature is proportional to the rate of Joule heating, $\dot{Q}_v'''$, or equivalently to the current density squared. The maximum temperature also depends quadratically on the length of Region 1, L. This imposes a practical limit on the length of the coil for a given current density.

We next plot these results for typical values. First, we use equation (4.4) to plot the temperature distribution in Region 1 where the wire has Joule heating and heat flows toward one end. Below is a summary of some typical parameters:

- Our wire is 23-gauge copper magnet wire; it has a copper cross-sectional area $A = 2.59 \times 10^{-7}$ m^2.
- We consider a length $L = 5$ cm of wire.
- We will evaluate the temperature distribution at different currents. A current $I = 2.59$ A in this wire corresponds to a current density of $J = 1.0 \times 10^7$ A/m^2. All our current densities are given for a single wire. The current density averaged over a region of wires will be somewhat less, due to the finite packing efficiency of round wires.
- We use the standard electrical and thermal conductivities of copper; i. e., $\sigma = 5.6 \times 10^7$ $1/(\Omega \cdot \mathrm{m})$ and $k = 401$ W/(m $\cdot$ K).

A plot of the temperature rise along the wire for different currents $I = 2, 4, 6, 8$ A is shown in Figure 4-4. Note that the rate of change of temperature with position decreases near the hot section of the coil so that it is easy to measure the maximum coil temperature without requiring an accurate position measurement. For example, a thermocouple placed approximately in the center of a length of wire cooled on both end-turns will measure the maximum temperature accurately even if it is slightly off-center.

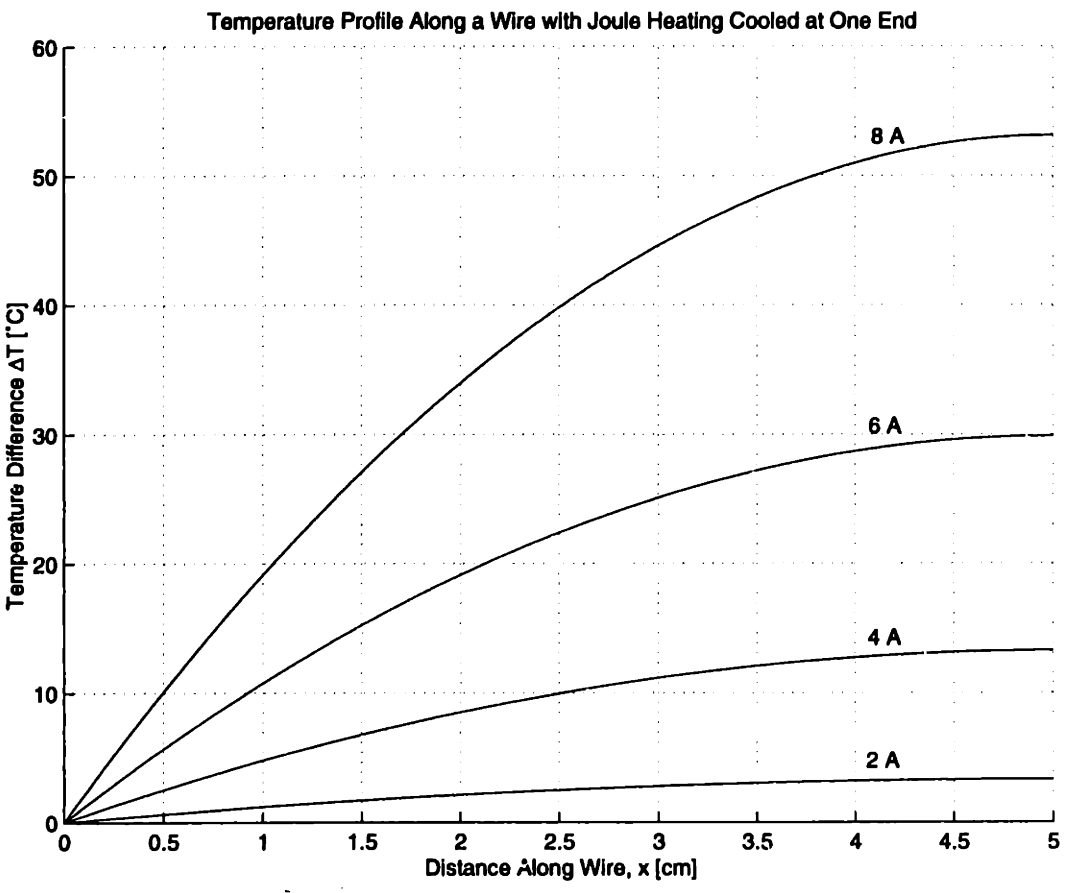

Figure 4-4: The temperature distributions along a 5 cm long piece of 23 gauge copper wire cooled at one end are shown for different currents. The temperature rise is parabolic with distance along the coil and scales as the square of current.

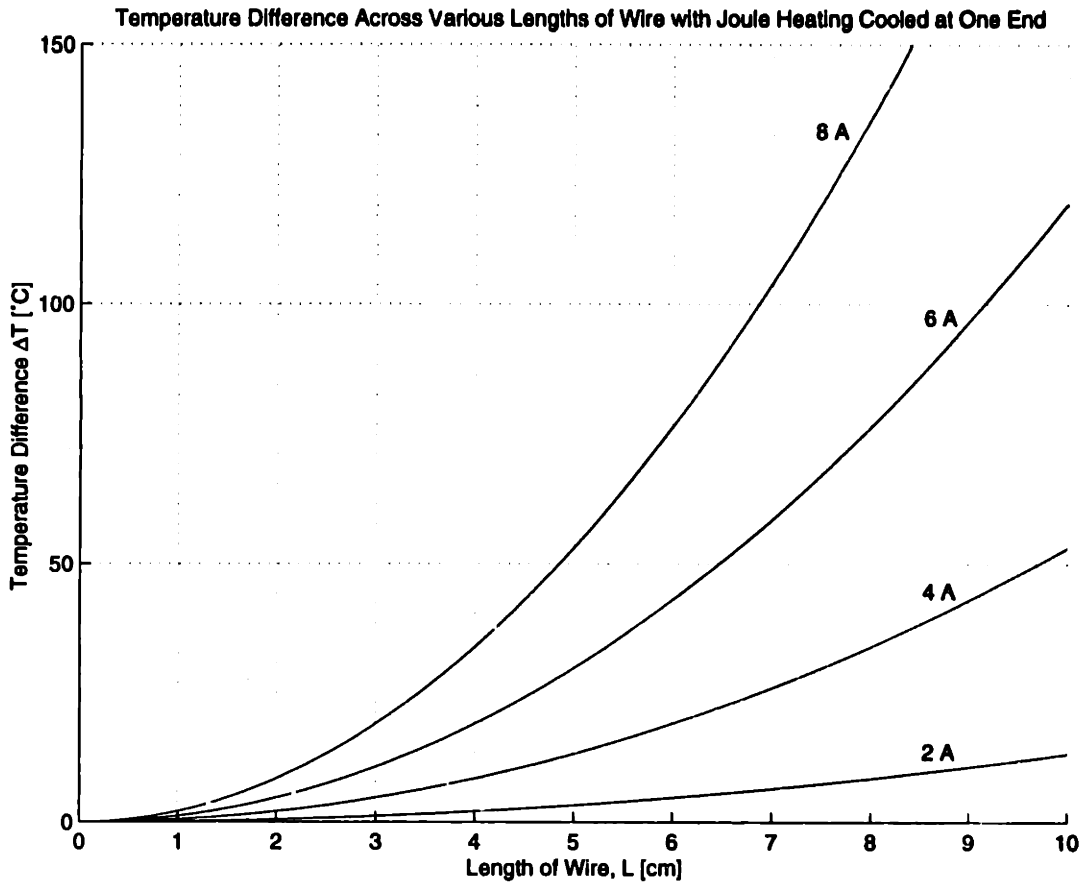

Figure 4-5: The maximum temperature rise along the coil ($x = L$) is plotted as a function of the length of 23 gauge wire for different currents. This is a plot of equation (4.5).

Figure 4-5 contains additional useful design information. It shows the maximum temperature rise, $T(x = L)$, for different currents as a function of the length of the wire. For any cooling scheme where the heat must travel along the wire before being removed, this figure is applicable and imposes a limit on the length of wire or current that can be used. For example, consider a coil approximately 10 cm long which will be cooled on one end-turn. If we are designing for a total 100°C temperature rise, we will be limited to roughly 5 A assuming we have a negligible temperature rise at the end-turn. In reality this will not be negligible, and a balanced design might allow half the temperature rise to occur at the end-turn and half to occur along the wire. For an allowed 50°C temperature rise we can only pump 4 A through the coil. Next, consider that we want to design a coil to withstand high currents such as 8 A. It is

clear that our 10 cm long coil cooled at one end will definitely not work. Instead, we might consider cooling the coil at both ends. This changes the effective length, L, from 10 cm to 5 cm. As we can see from Figure 4-5 this results in an acceptable hot spot temperature rise of 50°C.

4.1.2.2 Temperature Dependent Electrical Conductivity

Next, we repeat the analysis of the previous section while allowing for a temperature dependent electrical conductivity, $\sigma(T)$. Typically, this temperature dependence is expressed in terms of resistance which is inversely proportional to $\sigma(T)$. The resistance $R(T)$ of copper at a temperature T is often approximated by a linear function of temperature:

$$R(T) = R_1[1 + \alpha_1(T - T_1)] \tag{4.6}$$

R_1 is the resistance at a reference temperature T_1 often taken to be 25°C. The temperature coefficient of resistance for copper is $\alpha_1 = 0.00385$ [K^{-1}]. The boundary conditions on the wire are the same as before—constant temperature T_0 on one end and adiabatic on the other. The generalized version of equation (4.3) for a temperature dependent electrical conductivity is

$$\frac{d^2T}{dx^2} + \frac{J^2}{k\sigma(T)} = 0. \tag{4.7}$$

We can substitute for $\sigma(T)$ using equation (4.6). Next we make the change of variables $T' \equiv T - T_1$ so that T' is the temperature difference with respect to the reference temperature, T_1. The resulting equation is

$$\frac{d^2T'}{dx^2} + \frac{J^2\alpha_1}{\sigma_1 k}T' + \frac{J^2}{\sigma_1 k} = 0 \tag{4.8}$$

where σ_1 is the electrical conductivity at the reference temperature T_1. For $T_1 = 25$°C, $\sigma_1 = 5.6 \times 10^7$ $(\Omega \cdot \mathrm{m})^{-1}$. The first and third terms of this equation are identical to the two terms in equation (4.3). The second term is new and contains the effect of the temperature dependent electrical conductivity. Next we solve this second-order

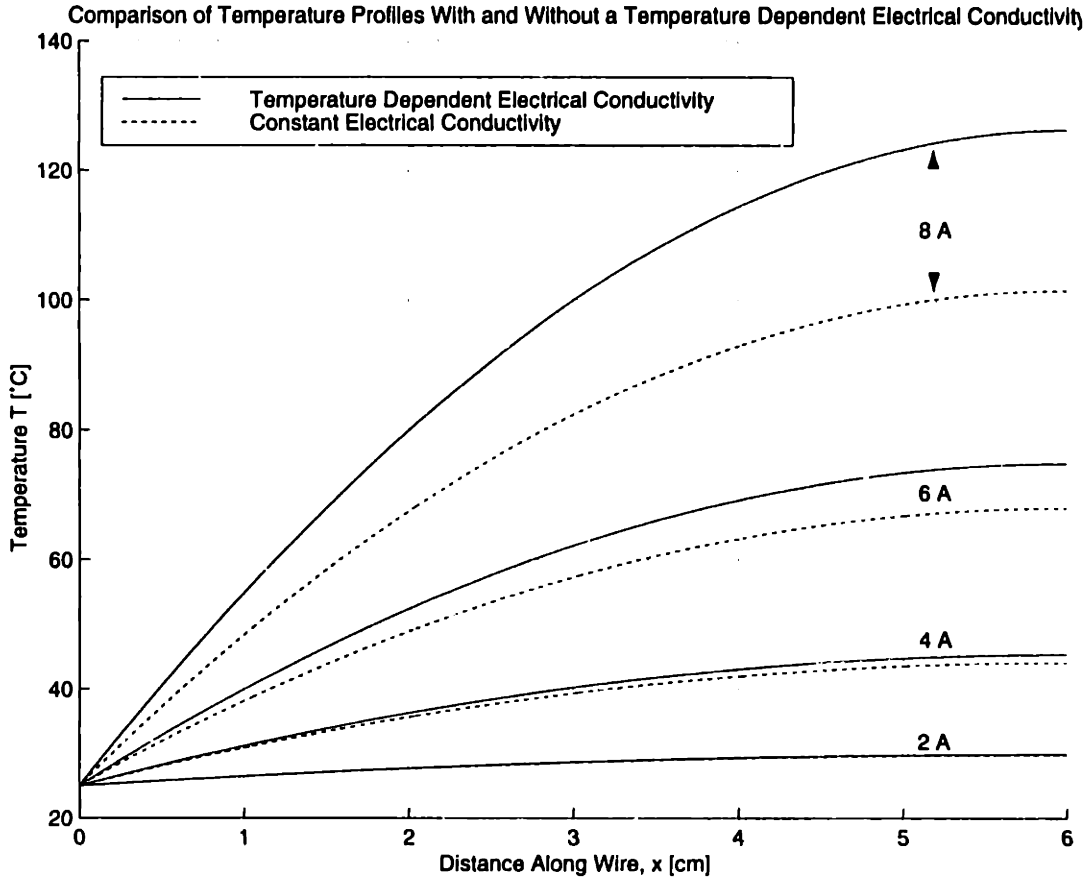

Figure 4-6: The temperature profiles along a wire are plotted including the effect of a temperature dependent electrical conductivity and are compared to profiles ignoring this effect. Notice that the difference between the two methods is insignificant for low temperature rises but becomes important for large temperature rises.

differential equation subject to the boundary conditions. We define the parameter $\gamma \equiv \frac{J^2}{\sigma_1 k}$ and change variables back to absolute temperature, $T = T' + T_1$. The solution of equation (4.8) is

$$T(x) = \left(\frac{T_0 - T_1 + \frac{1}{\alpha_1}}{\cos(\sqrt{\alpha_1 \gamma} L)} \right) \cos(\sqrt{\alpha_1 \gamma}(x - L)) - \frac{1}{\alpha_1} + T_1 \qquad (4.9)$$

Although this looks quite different from the solution when σ is independent of temperature, we will show that in fact the two solutions are quite similar and that this solution approaches the previous one in the limit where $\alpha_1 \to 0$.

Figure 4-6 compares the temperature distributions predicted by equation (4.9) and

equation (4.4) which respectively include and ignore the temperature dependence of the electrical conductivity, σ. We plot the two temperature profiles for four different currents. The difference between the two solutions is significant for coils at high temperatures. High currents correspond to high temperatures, but it is the temperature, not the current which determines the accuracy of the simpler method. We see that for the 2 A and 4 A cases, we expect temperature rises under 30°C for a 6 cm piece of 23 gauge copper wire. Both equations predict essentially the same temperature variation over the wire in these cases. This is to be expected when the overall temperature rise is small because the temperature dependent electrical conductivity $\sigma(T)$ is still close to its original value. In the 6 A case there is a difference between the two temperature profiles. As expected, the one which accounts for $\sigma(T)$ gets hotter since the hot resistance is higher, and more heat is dissipated than would be expected with a constant cold resistance. In the 8 A case, the constant cold resistance profile predicts a maximum temperature of 102°C while the profile accounting for the increase in resistance predicts a maximum temperature of 126°C. We conclude that the simpler constant cold resistance equation (4.4) can be used accurately when the maximum temperature is below 50°C. Above this temperature (or a temperature rise with respect to ambient of 25°C) it is best to use equation (4.9).

4.1.3 Region 2 – End-Turn Model

4.1.3.1 Lumped Model

Depending on the coil geometry and the cooling method, it may be reasonable to model the end-turn of the coil as a piece of copper at a constant temperature. This is called a lumped model since the variation in temperature along the end-turn is neglected. The following section will do a more exact analysis by allowing for this variation with a standard fin model. The lumped model will be applicable when the temperature difference from the end-turn to the cooling medium is much greater than any temperature variation along the wire.

In the lumped case, we have a simple conduction problem. We know the amount

of power which must travel from the end-turn to the cooling medium and want to determine the temperature rise ΔT. This amount of power $\dot{Q}$ is just the total amount produced by Joule heating in the entire coil. We can approximate the thermal resistance from the coil to the cooling medium as a series of thermal resistances. These include the conduction resistances of the coil insulation and epoxy potting material and the convection resistance to the coolant. The combination of these resistances, R_{tot}, can be used to predict ΔT via the well-known relationship $\Delta T = \dot{Q} R_{tot}$ which is analogous to Ohm's Law. We will also use R_{tot} in the fin analysis.

4.1.3.2 Fin with Joule Heating

If there is a significant temperature variation along the end-turn, we can no longer get accurate results with the lumped model just presented. (We certainly will not be able to predict the temperature variation since a lumped model by definition assumes the end-turn will be at a constant temperature.) The fin approximation allows for temperature variation along the wire but assumes that the temperature variation across the wire cross-section is negligible. This is an assumption we also made for the Region 1 calculation.

Half of an end-turn looks like a standard fin: The side connected to Region 1 has a constant heat flux, the middle of the end-turn is adiabatic by symmetry, and the edges of the end-turn lose heat via convection. In addition, we have internal heat generation everywhere, and an energy balance similar to the one shown in Figure 4-3 yields:

$$A_c\, q|_x - A_c\, q|_{x+\Delta x} - h\mathcal{P}\Delta x(T - T_\infty) + \dot{Q}_v''' A_c \Delta x = 0 \qquad (4.10)$$

A_c [m^2] is the cross-sectional area, $\mathcal{P}$ [m] is the perimeter of the wire, h [W/m^2·K] is the average heat transfer coefficient, T [K] is the temperature at position x along the fin, and T_∞ [K] is the temperature of the cooling fluid. The standard convection equation relates these last three variables to the heat flux: q [W/m^2] $= h(T - T_\infty)$. The average heat transfer coefficient h normally specifies the heat transfer due to convection alone. Here we can generalize h to include conduction through layers of

insulation and epoxy and then convection. This is possible since the thermal resistance is $R = 1/Ah$ where A is the area exposed to convection. Our previous R_{tot} is thus related to h.

As is customary, we define the fin parameter m by

$$m^2 = \frac{h\mathcal{P}}{A_c k}. \tag{4.11}$$

The differential equation corresponding to equation (4.10) is

$$\frac{d^2T}{dx^2} - m^2(T - T_\infty) = -\frac{\dot{Q}_v'''}{k}. \tag{4.12}$$

The solution to this equation subject to our boundary conditions

1. Adiabatic: $q(x = 0) = 0$
2. Constant heat flow $q_0 > 0$ into end-turn from rest of coil: $q(x = L) = -q_0$

is

$$T(x) - T_\infty = \frac{q_0}{km\,\sinh(mL)}\cosh(mx) + \frac{\dot{Q}_v'''}{km^2}. \tag{4.13}$$

Figure 4-8 on page 98 shows a plot of this equation for one set of parameters. The detailed example leading up to this plot follows in the next section.

4.2 Detailed Thermal Calculations

This section describes the complete thermal model for a liquid cooled separated end-turn coil. It incorporates many of the ideas developed thus far and shows how they all fit together into an engineering model. An example of practical interest is interweaved with the equations to show how they are applied and to give a feel for the numbers involved. The example chosen is to predict the temperature rise and heat flow in our prototype motor with separated end-turn coils and oil cooling. Many pieces of this analysis will be applicable more generally for other types of coils and cooling schemes.

4.2.1 Problem Statement

We first describe our sample problem. Our prototype motor uses coils with separated end-turns on both sides. A picture of one such coil is shown in Figure 6-3. The coils are made of 23 A.W.G. copper magnet wire and contain 22 layers with 11 turns per layer for a total of 242 turns. The twenty-two layers are separated into eleven groups of two on the end-turns. The gaps between these eleven groups are equal to one wire diameter (0.025″). We would like to apply our previous quarter coil model and identify Regions 1 and 2 (Figure 4-2). Unfortunately, the lengths of these Regions change significantly over the different layers. Thus, for parts of the analysis we must restrict our attention to one layer at a time. Figure 4-7 shows the lengths of Regions 1 and 2 associated with different layers. We choose to look at the outermost layer in this example since we can place thermocouples on it and obtain experimental data for comparison. This poses one problem, however, as the outermost layer has a significantly longer area exposed to oil cooling than all the other layers do. This occurs because the sides of the coil's end-turns are cooled as shown in Figure 4-7. Thus, it is tricky to decide where to locate the breakpoint between Region 1 and Region 2 in the outermost layer. Here we choose an average of Region 1 and Region 2 lengths, L and l_c respectively, over the outermost two layers. This is somewhat arbitrary but is justified by the fact that heat transfer between two adjacent layers is good. In any case, the procedure is unchanged and the breakpoint between the Region 1 and Region 2 sections is very clear for all the inner layers. The only reason we tackle this calculation for the outermost layer is that we can readily compare it to experimental data. One thermocouple is placed at the center of the end-turn for the outermost layer and another is placed at center of the side of the coil (the hotspot for the outermost layer).

The three motor coils are connected in a wye. We apply a DC current of 7 A across two coils and leave the third unconnected. Mobiltherm 603 oil flows through the top end-turns and then through the bottom end-turns of each coil before returning to the cooling tank and pump. Thermocouples measure the oil temperature before and

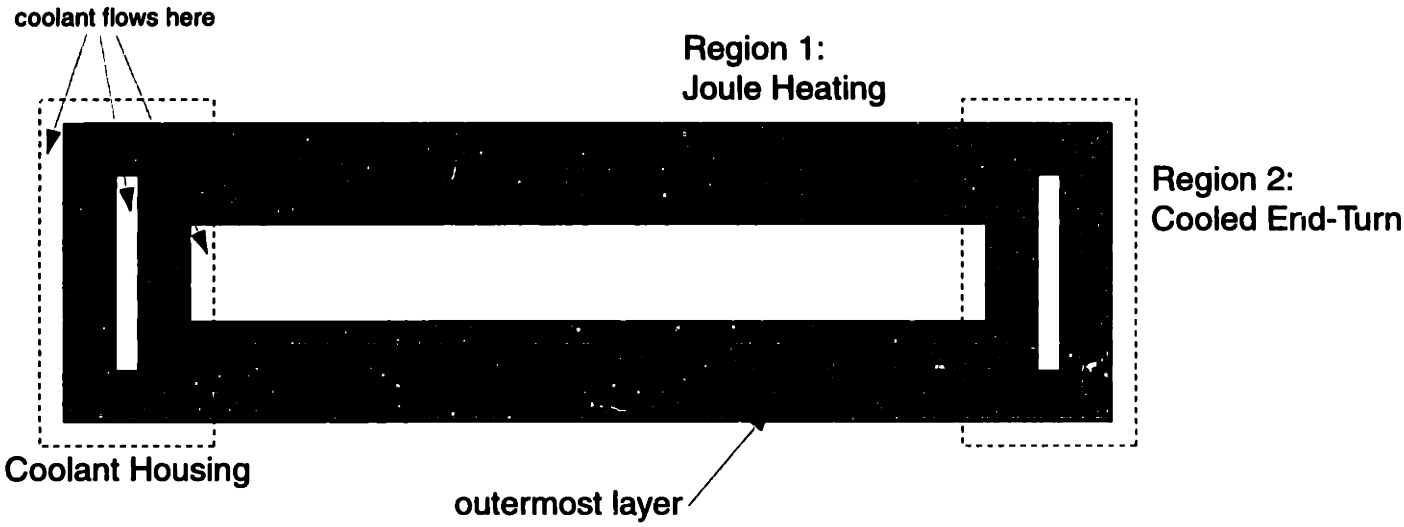

Figure 4-7: A schematic of a four layer coil with separated end-turns is shown. Coolant flows through the gaps in the end-turns and is contained by the coolant housing. Note that the lengths of Regions 1 and 2 change from layer to layer. Also note that the outermost layer is the only one which is cooled on the sides of the end-turn. This causes the outermost layer to have a much longer Region 2 than any other layer.

after passing through the motor.

The following variables are used in the calculation. Values given are specific to this example problem:

Symbol	Description	Value	Units
N_l	Number of layers of wire in coil	22	layers
N_t	Number of turns per layer	11	turns/layer
N	Total number of turns in coil	242	turns
g	Gap between separated end-turns	0.635	mm
n	Number of coils	2	coils
L	Length of Region 1 for the outer layer of coil	4.0	cm
l_c	Length of Region 2 for the outer layer of coil	3.0	cm
w	Width of coil	7.62	mm
Q	Volume flow rate of oil	0.37	gpm
		$= 2.334 \times 10^{-5}$	m^3/s
I	DC current applied to coils	7.00	A

The following material properties are also used:

Copper	σ	Electrical Conductivity	5.6×10^7	$(\Omega \cdot m)^{-1}$
	k_{Cu}	Thermal Conductivity	401	W/(m·K)
Mobiltherm 603 Oil	ρ	Density	820	kg/m^3
	c_p	Specific Heat	1892.5	J/(kg·K)
	k_{oil}	Thermal Conductivity	0.132	W/(m·K)
	ν	Kinematic Viscosity	4.40×10^{-5}	m^2/s
	Pr	Prandtl Number	517	

4.2.2 End-turn (Region 2) Calculations

The temperature distribution along the end-turn is given by equation (4.13) derived earlier for a fin with Joule heating. In order to use this equation we will need h which is included in the variable m (4.11). The heat transfer coefficient h includes

Material	Thickness, t [mm]	Thermal Cond. k [W/(m·K)]	$\hat{R}$ [K·m^2/W]
Polyester Insulation	0.025	0.24	1.0×10^{-4}
Epoxy Bond	0.015	0.17	8.8×10^{-5}
TOTAL			1.88×10^{-4}

Table 4.1: Calculation of Unit Conduction Resistance. Thermal conductivities are from Mills [26].

the effects of conduction resistance through the wire insulation layers and convection resistance of the flowing oil. The convection heat transfer coefficient h_c only includes the effects of convection resistance to the flowing oil. The calculation of h is the hardest part of the thermal model to accurately predict based only on theory. The quantity h depends, in a complex way, on the geometrical configuration, surface characteristics, and solid and fluid parameters. Expressions for h are determined using dimensional analysis and experimental data, and h is inversely proportional to the thermal resistance. We first calculate the thermal resistance due to conduction across insulation layers. Second, we use an empirical formula to find h_c, and thus, the convection resistance. Finally, we combine these two thermal resistances in series and use the total resistance to give us h.

4.2.2.1 Conduction Resistance

The thermal resistance R [K/W] across a material of thickness t [m], thermal conductivity k [W/(m·K)], and area A [m^2] is given by $R = t/kA$. We will find it more convenient to use the unit thermal resistance $\hat{R}$ [K·m^2/W] given by $\hat{R} = t/k$. Table 4.1 shows the calculation of the unit conduction resistance due to the polyester insulation and epoxy bond layers coating the bare copper wire. These thicknesses are typical for bondable polyester-imide magnet wire as specified by the MWS Wire Catalog [19]. We find that

$$\hat{R}_{conduction} = 1.88 \times 10^{-4} \text{ K} \cdot \text{m}^2/\text{W} \tag{4.14}$$

4.2.2.2 Convection Resistance

The unit thermal resistance for convection is given by $\hat{R} = 1/h_c$ where h_c [W/(m^2·K)] is the average convection heat transfer coefficient. Our task now is to estimate h_c. This can be done by calculating the dimensionless Nusselt number, Nu, using the appropriate empirical formula. Before we can select the appropriate one, we must examine the oil flow in more detail. We model the gap in the end-turns as a rectangular duct through which the oil flows.

We first calculate the hydraulic diameter, D_H, which is an effective diameter for non-cylindrical tubes:

$$D_H = \frac{4A_c}{\mathcal{P}} = \frac{4g(2l_c)}{2(g+2l_c)} \approx 2g = 1.27 \text{ mm} \tag{4.15}$$

where A_c and $\mathcal{P}$ are the cross-sectional area and wetted perimeter of the duct respectively. In our case the duct is a rectangle with dimensions $2l_c$ by g. Next, we calculate the velocity, v, of the oil through the gaps in the end-turn.

$$v = \frac{Q}{A} = 0.144 \text{ m/s} \tag{4.16}$$

where $Q = 0.37$ gpm $= 2.334 \times 10^{-5}$ m$^3/s$ is the volume flowrate and $A = 1.626 \times 10^{-4}$ m^2 is the cumulative area of all the gaps in an end-turn. Next we calculate the Reynolds Number Re_{D_H}:

$$Re_{D_H} = \frac{vD_H}{\nu} = 4.16 \tag{4.17}$$

For an internal tube flow between parallel plates like the one considered here, flows with $Re < 2800$ are considered laminar.[1] Our oil flow is laminar as would be expected. Tube flows with $Re > 10,000$ are turbulent. If we considered water cooling instead of oil coiling, we would be closer to turbulence which is usually associated with improved heat transfer.

The Nusselt number for a duct flow depends on the geometry of the duct and the

[1] In a cylindrical duct, transition to turbulence usually is quoted at $Re_D \approx 2300$.

boundary conditions applied. The cross-section of our duct is a very long and thin rectangle which approximates two infinitely long parallel plates. The Nusselt number for a parallel plate duct flow with constant wall heat flux is 8.24. However, the Nusselt number and heat transfer coefficient h will be higher if the flow is not fully thermally developed. Heat transfer is increased when a flow is not fully thermally developed because the temperature gradient from the bulk fluid to the wall occurs over a shorter distance than the radius of the duct. The laminar thermal entry length, x_{e_t} is given by

$$x_{e_t} \approx 0.03 Re_{D_H} D_H Pr = 82 \text{ mm}, \tag{4.18}$$

which is significantly greater than the width of our coils, $w = 7.62$ mm. Thus, we should use an average Nusselt number that takes into account the thermal entry length. An average Nusselt number for isothermal parallel plates of length w (our coil width) is given in [8]

$$\overline{Nu}_{D_H} = 7.54 + \frac{0.03(D_H/w)Re_{D_H}Pr}{1 + 0.016[(D_H/w)Re_{D_H}Pr]^{2/3}} = 13.5. \tag{4.19}$$

Even though we do not have isothermal boundary conditions, this should still be a reasonable approximation. Note that a different Nusselt number equation might apply in the case of air or water cooling since the Re and Pr would be different in those cases, and the flow might not even be laminar.

The dimensionless Nusselt number is always related to h_c by the equation,

$$Nu_{D_H} = \frac{h_c D_H}{k_{oil}}. \tag{4.20}$$

Solving for h_c, we obtain

$$h_c = 1403 \text{ W}/(\text{m}^2 \cdot \text{K}) \tag{4.21}$$

which gives us

$$\hat{R}_{convection} = \frac{1}{h_c} = 7.12 \times 10^{-4} \text{ K} \cdot \text{m}^2/\text{W} \tag{4.22}$$

4.2.2.3 Total Resistance

The total unit resistance $\hat{R}_{tot}$ due to conduction and convection is just the sum of the individual resistances,

$$\hat{R}_{tot} = \hat{R}_{conduction} + \hat{R}_{convection} = 1.88 \times 10^{-4} + 7.12 \times 10^{-4} = 9.00 \times 10^{-4}\ \mathrm{K \cdot m^2/W} \tag{4.23}$$

It is interesting to compare the magnitude of these two resistance components. We cannot lower the conduction resistance unless we obtain wire with thinner insulation and bond coatings. Our design can however affect the magnitude of the convection resistance. From equation (4.23) we see that the convection resistance is larger than the conduction resistance by a factor of approximately four. The best we could hope for in a design is that the convection resistance be less than the conduction resistance. Once this occurs, further reduction in convection resistance is useless as the heat transfer is governed by the conduction resistance. Here we are not in this regime, but the convection resistance is the same order as the conduction resistance. The heat transfer coefficient is

$$h = \frac{1}{\hat{R}_{tot}} = 1111\ \mathrm{W/(m^2 \cdot K)}. \tag{4.24}$$

4.2.2.4 Fin Calculation

The current density J is given by

$$J = \frac{I}{A} = \frac{7\ \mathrm{A}}{2.59 \times 10^{-7}\ \mathrm{m^2}} = 2.70 \times 10^7\ \mathrm{A/m^2} \tag{4.25}$$

where A is the cross-sectional area of a 23 gauge wire. The internal heat generation in our wire is

$$\dot{Q}_v''' = \frac{J^2}{\sigma} = 1.30 \times 10^7 \frac{\mathrm{W}}{\mathrm{m^3}}. \tag{4.26}$$

When we solved the fin with Joule heating problem, one boundary condition was a constant heat flow of q_0 into the end-turn from the rest of the coil. We are now in a position to calculate q_0 which is just the heat generated in Region 1 of the coil. We

calculate this for the outermost layer of the coil which has $L = 0.04$ m:

$$q_0 = \dot{Q}_v''' L = 5.20 \times 10^5 \frac{\mathrm{W}}{\mathrm{m}^2}. \tag{4.27}$$

Next, we solve for the fin parameter m^2 using h. The perimeter $\mathcal{P}$ of the fin is the length exposed to coolant. In our calculation we are considering only one wire, so $\mathcal{P}$ can be approximated by the diameter of the wire, $\mathcal{P} = 0.635$ mm. The fin parameter m is

$$m^2 = \frac{h\mathcal{P}}{A_c k_{Cu}} = 6793. \tag{4.28}$$

Now we have calculated all the parameters we need to use equation (4.13) to find the temperature distribution along Region 2 for the outermost layer. This distribution is plotted in Figure 4-8. Note that the middle of the end-turn is 7.4°C above the oil temperature and the temperature rise over the length of the end-turn is 13.3°C.

Experimentally, we found the center of the end-turn to be 27°C under the conditions we have been considering while the oil inlet temperature was 20.5°C. This yields an experimental temperature difference of 6.5°C which agrees well with the calculated value of 7.4°C.

4.2.3 Region 1 Calculations

It now remains to calculate the temperature rise over Region 1. We use equation (4.9) which incorporates the temperature dependence of the electrical conductivity of copper into the calculation. We use the results of the previous section to find the temperature, T_0, at the location separating Regions 1 and 2.

$$T_0 = T_{oil} + \Delta T_{Region\ 2} = 20.5 + 20.7 = 41.2°\mathrm{C} \tag{4.29}$$

T_{oil} is the oil inlet temperature and $\Delta T_{Region\ 2}$ is the temperature rise over Region 2 (see Figure 4-8). The parameter γ is

$$\gamma = \frac{J^2}{\sigma_1 k} = 32464\ \mathrm{K/m}^2. \tag{4.30}$$

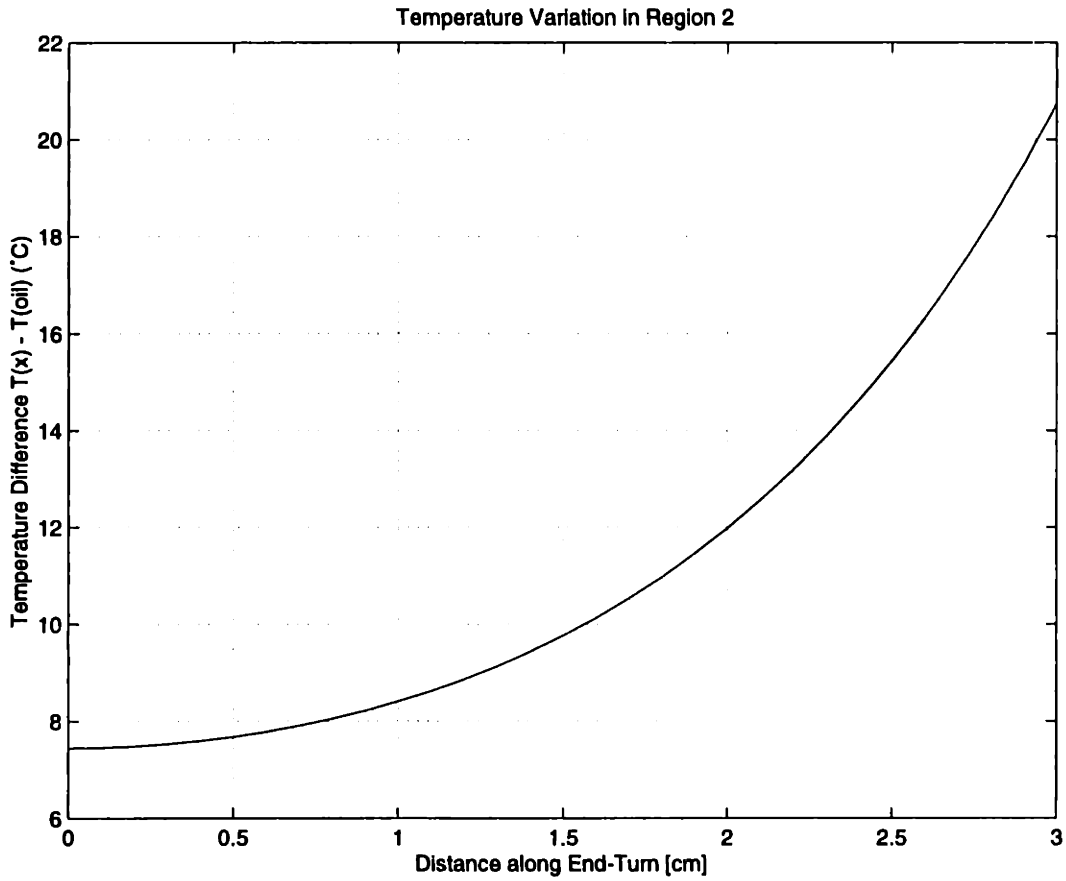

Figure 4-8: The temperature distribution along the outermost cooled end-turn is shown from the middle of the end-turn to the edge of the end-turn. The temperature difference between the coil and the (constant) oil temperature is plotted. This is a graph of equation (4.13) for the parameters developed in section 4.2.

We have the length of Region 1, $L = 0.04$ m, and can calculate $T(L)$, the temperature at the hot side of Region 1, using equation (4.9):

$$T(L) = 71°\text{C}. \tag{4.31}$$

The hot point temperature was found experimentally to be 77°C which is close to our theoretical prediction. In this particular example, we had the added complexity of not knowing the precise Region 1 and Region 2 lengths since, as mentioned earlier, the outermost layer has additional cooling. Changing these lengths can affect the result appreciably. This is not an issue for the other layers since the lengths of the two regions are clearly defined.

4.2.4 Oil Temperature Rise

We now check to see that the power dissipated in the coils is absorbed by the oil. The measured voltage across the two coils for an applied current of $I = 7$ A is $V = 55.2$ V. Thus, the total power, P, generated by the two coils is

$$P = IV = 386 \text{ W}. \tag{4.32}$$

The oil inlet and outlet temperatures are measured to be $T_{oil\ in} = 20.5°\text{C}$ and $T_{oil\ out} = 31.6°\text{C}$. The outlet temperature is measured after the oil has passed all six sets of end-turns. Four end-turns are attached to the two heated coils, and the other two end-turns are attached to the unheated coil. We also know the volume flow rate of oil, $Q = 0.37$ gpm, the oil's specific heat $c = 1892.5$ J/(kg·K), and its density $\rho = 820$ kg/m^3. The heat absorbed by the oil is

$$\dot{Q} = \rho Q c(T_{oil\ out} - T_{oil\ in}) = 401 \text{ W} \tag{4.33}$$

which matches the heat generated by the coils as it should. From a design point of view, these same calculations can be used to predict the oil temperature rise. In this case, the oil rise was $\Delta T_{oil} = 11.1°\text{C}$ overall, or 2.8°C per end-turn. Note that

the oil temperature rise can easily be reduced by increasing the flow rate of oil. In our prototype experiment, a small oil pump was used. A larger oil pump capable of pumping four times the flow rate would reduce the oil rise to less than 3°C.

We have developed the Region 1 and Region 2 thermal models in this chapter and provided a detailed example illustrating their use. In the next chapter we present experimental data which corroborate these models.

Chapter 5

Thermal Measurements

5.1 Single-Sided Water Cooled Coil

Before the prototype motor was built, we did some preliminary experiments to test our thermal analyses. In particular, we wound a coil with only one separated end-turn which has twenty-one thermocouples embedded in it. The thermocouples are arranged along three layers in the coil and in each layer are spread out over half the coil. The positions of the thermocouples along each layer are measured and tabulated. Figure 5-1 shows a picture of this special coil. The coil is water cooled using the plastic housing with water inlet and outlet nozzles shown in Figure 5-2. Tap water is used to cool the coil. Typical flowrates are from one third gallon per minute (gpm) to one gpm. The water temperature from this faucet varied by as much as 10°C over time, so the water temperature is recorded with each measurement. In each experiment ten of the twenty-one thermocouples could be monitored using a ten-way thermocouple switch. The coil is allowed to come to equilibrium before any measurements are taken. This often takes only a few minutes whereas an uncooled coil will heat up slowly for half an hour.

Our goals for these experiments are to check our thermal models and see how well they work. Particularly, we want to check the Region 1 Joule heating temperature distribution along the coil, and the Region 2 fin temperature distribution along the end-turns.

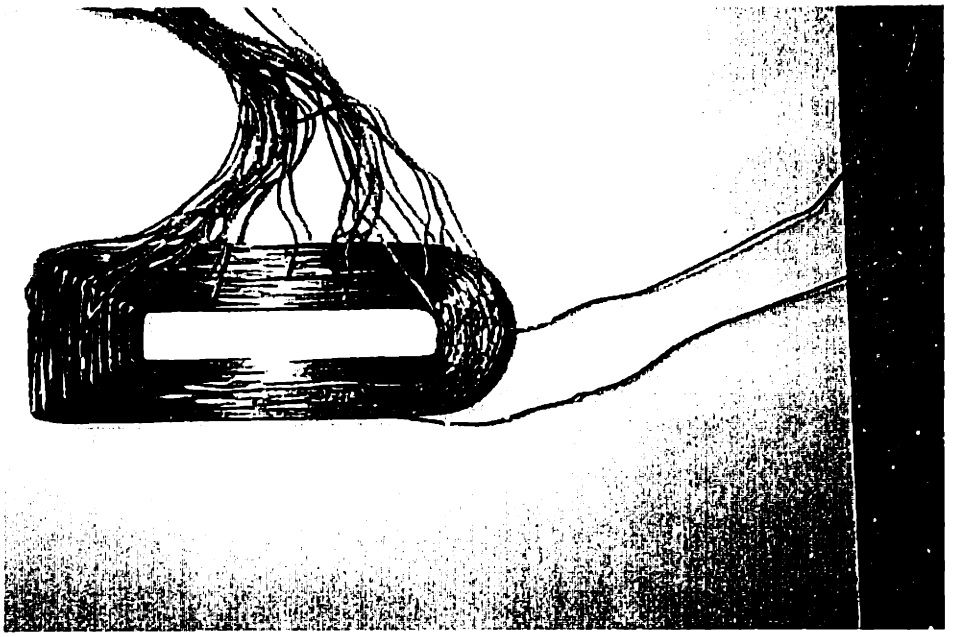

Figure 5-1: Twenty-one thermocouples are imbedded in this coil with one separated end-turn during the winding process. It is used for obtaining experimental temperature distributions.

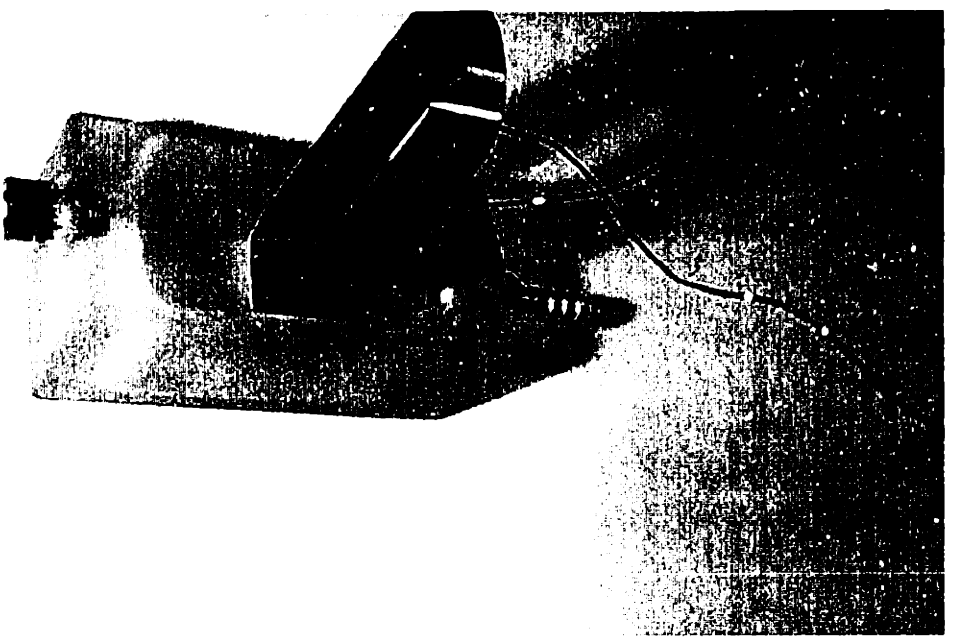

Figure 5-2: The experimental setup for cooling one end-turn with water is shown. During the tests, the uncooled part of the coil is covered in foam so that convection and radiation do not affect our temperature measurements.

5.1.1 Measured Temperature Distribution Along the Coil

In one experiment, we monitor a series of thermocouples in between the outermost two layers of the coil. Five of the thermocouples are located away from the end-turn in the part of the coil we have called Region 1 (section 4.1.2). The boundary conditions for Region 1 are that one end is adiabatic and the other has all the heat flowing out of it. Thus, for comparison purposes, we can choose Region 1 to stretch from the hot point of the coil to the last thermocouple before the cooled end-turn region of the coil. In order to predict the temperature variation we need a temperature for the cool endpoint. We use the actual temperature measured at the fifth thermocouple. We can now use equation (4.9) to predict the temperature distribution. Figure 5-3 shows these predictions and the measured temperature distributions for currents of 2.0, 3.0, and 4.0 A.

The agreement between theory and experiment for Region 1 is seen to be quite good. The slightly high reading of the thermocouple at position 1.3 cm for all three currents is likely a systematic error. It is difficult to measure the position of the thermocouples since they are embedded at various angles in the coil. Also, because so many thermocouples are wound into the coil, it has some imperfections. The hot spot temperatures are also about 2–3 degrees lower than predicted by theory. This is probably not due to position error because the temperature profile is flat near the hot spot. Instead it probably shows the effects of convection and radiation heat losses which are not included in our thermal model. These other modes of heat transfer become more important at hotter temperatures.

5.1.2 Measured Temperature Distribution Along the End-Turns

In another single-sided water cooling experiment, temperature data is collected for thermocouples located along the end-turns. This is the part of the coil called Region 2, and its thermal model is developed in section 4.1.3. It is hard to obtain an accurate, purely theoretical Region 2 temperature distribution. Here, we use equation (4.13)

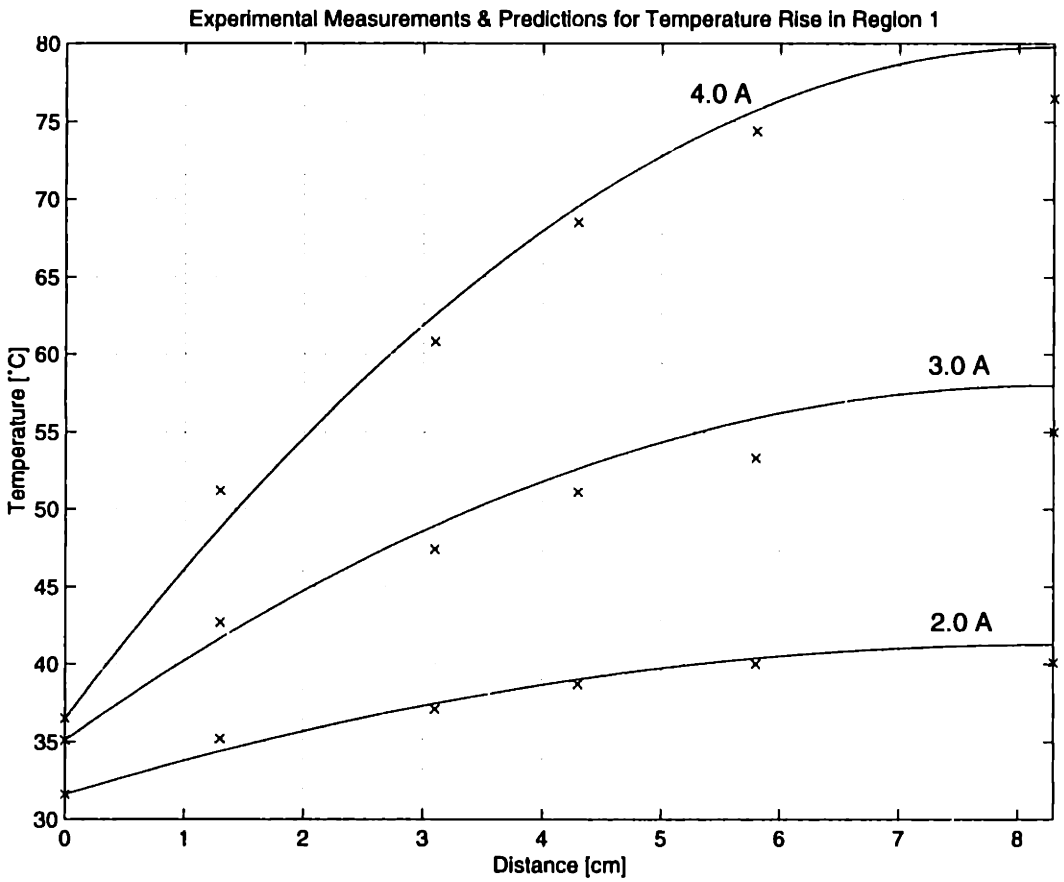

Figure 5-3: Experimental data (x) is compared to theoretical predictions for the temperature distribution along the uncooled part of the coil (Region 1).

but adjust one parameter, the fin parameter m to fit the data. This is justified because once we have determined m for a particular coolant and end-turn geometry it should remain the same for variations in current. Predicting m is equivalent to predicting the heat transfer coefficient h or total thermal resistance between the coolant and end-turns. This is very difficult to do accurately based only on theory, but section 4.2.2 showed how this calculation would be done. It is also difficult to experimentally measure the temperature distribution in the end-turns. In our test coil, the thermocouples inserted into the end-turns caused the gap thickness to narrow in places, disturbing the flow of water through the end-turns. Figure 5-4 shows the measured end-turn temperature distribution and the fin equation prediction where the fin parameter has been chosen to fit the data, $m = 84$.

The shape of the experimental temperature distribution shows that we have been justified in treating the end-turn as a fin. If the end-turn had a constant temperature distribution across it, we could model it as a lumped piece of wire with one temperature.

5.2 Double-Sided Water Cooled Coil

A preliminary double-sided cooling experiment was performed with water. Figure 5-5 shows how water was flowed through both end-turns while the center of the coil remained uncooled. This setup was built by Fred Sommerhalter at Anorad. Thermocouples were placed on the inside and outside layers in the uncooled center section, on the end-turn, and in the water. A water flow of 0.3 gallons per minute was used, and the water temperature varied from 20–24°C. Table 5.1 tabulates the temperature differences measured. When uncooled, our coil has an average temperature rise of 100°C when a current of 1.6 A passes through it for a long time (40 minutes). When subject to double-sided water cooling, the maximum temperature rise for 2.0 A is 3°C. We were able to put as much as 11 A in the cooled coil resulting in a hot point temperature rise of 133°C. This is 6.9 times the uncooled current and 47 times the heat dissipation.

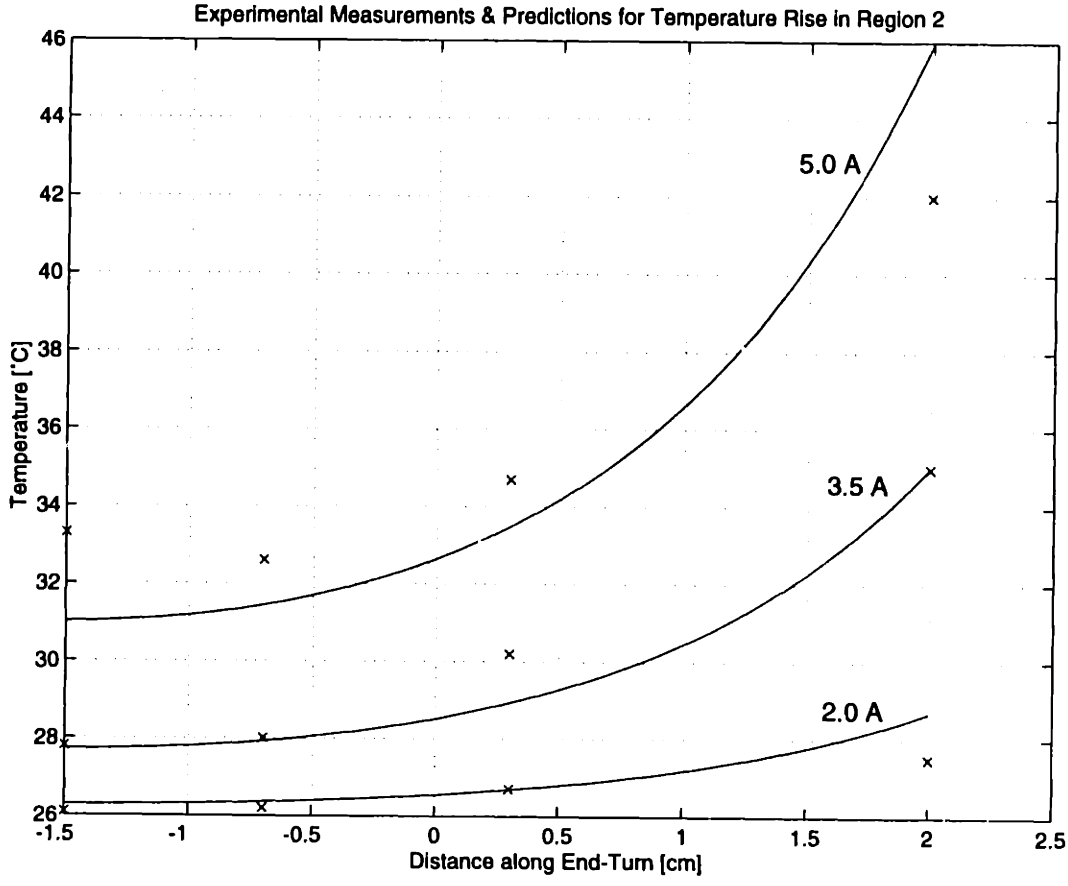

Figure 5-4: Experimental data (x) is compared to theoretical predictions for the temperature distribution along the cooled end-turns of the coil (Region 2). The cool side is the middle of the end-turn, and the hot side is near the corner of the coil where the end-turn joins the rest of the coil. The water flowing by the end-turns had a temperature of 26°C.

I [A]	$\Delta T_{end\ turn}$ [°C]	$\Delta T_{inside\ center}$ [°C]	$\Delta T_{outside\ center}$ [°C]
2	0	3	3
4	2	12	14
6	3	27	32
8	6	55	63
9	8	73	87
10	10	79	109
11	13	87	133

Table 5.1: Experimental data from a double-sided water cooling experiment is given. The temperature rise above the water temperature is tabulated.

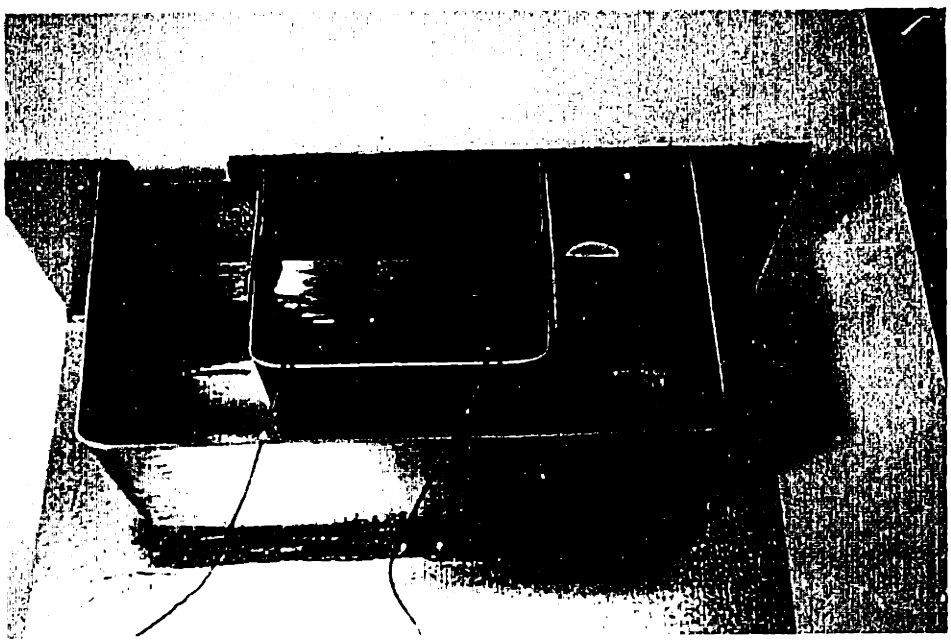

Figure 5-5: The setup for a double-sided cooling test is shown. A water hose is connected at the lower right, and the water flows through both end-turns before spilling out the spout at the top left. The center section of the coil is uncooled.

Once a coil is heated to an average temperature of 125°C, it will remain very hot for a long time (30 minutes) if left uncooled. Even when placed directly on top of a fan, the coil will remain too hot to touch for about 10 minutes. With direct liquid cooling, however, the coil will return to within a few degrees of the coolant temperature in about 45 seconds.

5.3 Oil Cooling of Separated End-Turn Motor

The thermal test data for our prototype oil cooled separated end-turn motor is presented in this section. We applied a DC current across two of the motor phases thus heating only two of the three coils. A small centrifugal pump from Gorman-Rupp Industries [12] was used to pump Mobiltherm 603 oil through the coil housings at a modest flowrate of 0.37 gpm. The oil was cooled with a water reservoir. At the end of the experiment, the oil absorbed a lot of heat so we started a chiller for the water reservoir. Thermocouples were placed at the oil inlet and outlet, on the middle of the

outer layer of the first coil, and in the top end-turn of the first coil.

5.3.1 Experimental Results

Table 5.2 shows the raw data taken, and Table 5.3 shows some analysis of the data. The hot resistance of the two coils is calculated based on the current and voltage supplied. The average temperature in the coil can be calculated from the ratio of the hot resistance to the cold resistance. The power supplied to the coils and the power removed by the oil are calculated and seen to be equal given the uncertainties in the oil temperature measurements. Figure 5-6 plots the average coil temperature as a function of current. The temperature at the middle of the outer layer of the first coil is also shown in the plot. This is seen to be slightly less than the average temperature of the coil. The temperatures at the middle of the inner layers of the coil are expected to be hotter so there is no discrepancy here. Recall that the outermost layer has additional cooling as shown in Figure 4-7. It takes 9 A to get the average temperature of the two coils up to 125°C. When uncooled, these coils will reach the same average temperature with only 1.6 A. We have thus demonstrated a 5.6 times increase in the maximum current and 32 times increase in the amount of heat dissipated over the uncooled case.

5.3.1.1 Fast Time Constant

As mentioned already, our coil takes 30 minutes to cool down from an average temperature of 125°C if left uncooled. In our experiment, the coil was heated up to an average temperature of 125°C with 9 A going through it and oil cooling. The hot spot temperature on the outer layer of the coil was 130°C. We turned off the power and let the oil continue to flow. The temperature dropped very rapidly: After 30 seconds, the hot spot temperature was down to 44°C, and after another 30 seconds it was down to 30°C. This is a consequence of the superior cooling design. The heat

[1]The oil reservoir started to heat up.
[2]The chiller was turned on to cool the oil.
[3]The oil temperature was unreliable as the reservoir started to heat up and the chiller was started.

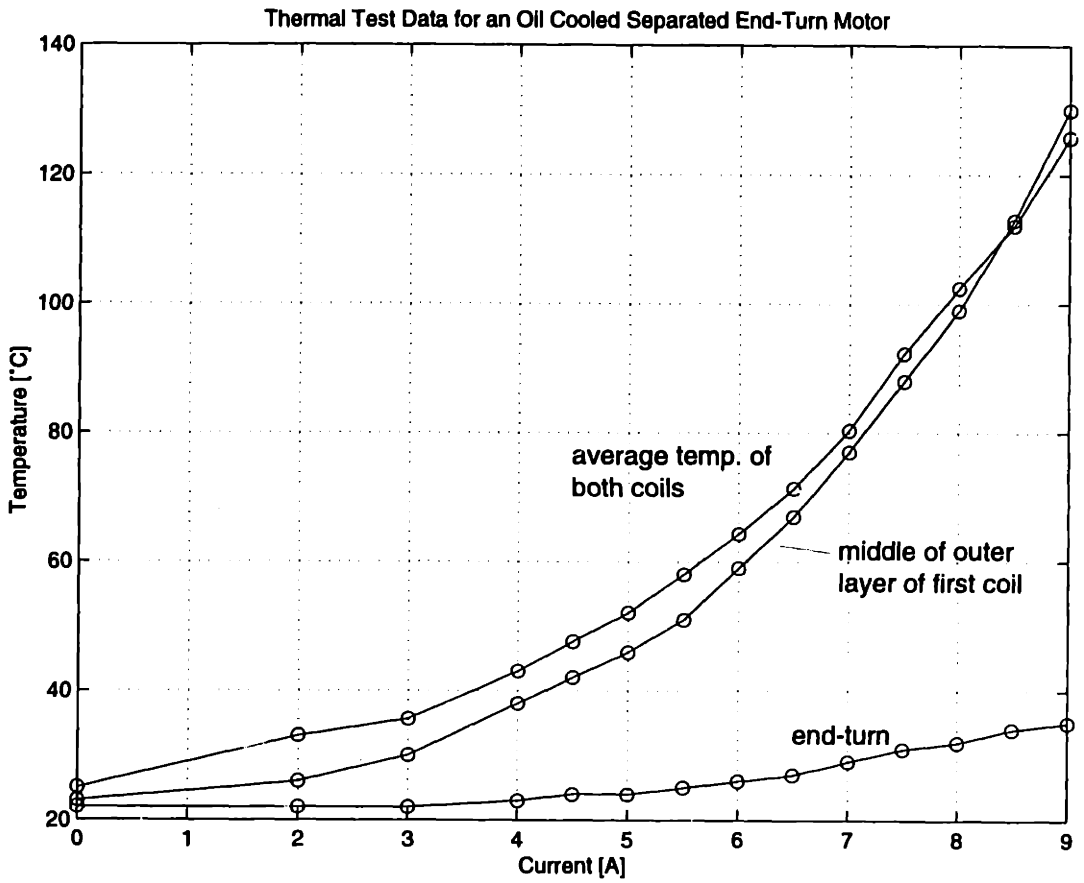

Figure 5-6: The average temperature of the two coils is plotted versus current. Also shown are the temperature at the middle of the outermost layer of the first coil and the temperature at the middle of the end-turn. When uncooled, this same coil heats up to 125°C everywhere with only 1.6 A.

I [A_{DC}]	V [V]	$T_{oil\ out}$ [°C]	$T_{oil\ in}$ [°C]	T_1 [°C]	T_2 [°C]	T_{hot} [°C]
0.00	0.0	20.7	20.6	22	22	23
2.00	13.4	20.6	19.5	21	22	26
3.00	20.3	21.6	18.6	22	22	30
4.00	27.8	23.3	18.4	22	23	38
4.50	31.8	24.2	18.2	23	24	42
5.00	35.9	25.3	18.3	23	24	46
5.50	40.3	26.7	18.5	24	25	51
6.00	44.9	28.5	18.8	25	26	59
6.50	49.8	30.4	20.2	26	27	67
7.00	55.2	31.6	20.5	27	29	77
7.50	61.4	33.3	25.5[1]	29	31	88
8.00	67.5	35.8	22.5[2]	31	32	99
8.50	73.8	38.8	23.4	32	34	113
9.00	81.2	42.0	23.7	34	35	130

Table 5.2: This temperature data was taken for our oil cooled separated end-turn motor at different DC currents, I. T_1 and T_2 are temperature measurements at the middle of two of the end-turns. T_{hot} is measured at the middle of the outer layer of the coil.

has a direct path out of the coil.

5.3.1.2 Oil Flow

The housings sealed the oil very well. After an hour of continuous oil flow, one drop had slowly leaked past the housings where a coil entered them. This joint had only been sealed with epoxy and was subsequently sealed with RTV silicone adhesive sealant.

At 9 A, the temperature of the oil leaving the motor was 18.3°C higher than the oil entering. This temperature difference is easy to eliminate by increasing the oil flowrate. If we tripled the volume flowrate of oil to about 1 gpm, this temperature difference would be one third of its previous value, or only 6°C.

We next examine the fabrication techniques used to wind separated end-turn coils and circulate oil through the end-turns.

I [A_{DC}]	R_{hot} [Ω]	T_{avg} [°C]	$P = IV$ [W]	ΔT_{oil} [°C]	P_{oil} [W]	ΔT_1 [°C]	ΔT_2 [°C]
0.00	6.50	25.0	0.0	0.1		1.4	1.4
2.00	6.70	33.0	26.8	1.1	39.8	1.5	2.5
3.00	6.77	35.6	60.9	3.0	108.7	3.4	3.4
4.00	6.95	43.0	111.2	4.9	177.5	3.6	4.6
4.50	7.07	47.6	143.1	6.0	217.3	4.8	5.8
5.00	7.18	52.1	179.5	7.0	253.5	4.7	5.7
5.50	7.33	58.0	221.7	8.2	297.0	5.5	6.5
6.00	7.48	64.3	269.4	9.7	351.3	6.2	7.2
6.50	7.66	71.4	323.7	10.2	369.4	5.8	6.8
7.00	7.88	80.3	386.4	11.1	402.0	6.5	8.5
7.50	8.19	92.3	460.5	7.8^3	282.5	3.5	5.5
8.00	8.44	102.4	540.0	13.3	481.7	8.5	9.5
8.50	8.68	112.1	627.3	15.4	557.8	8.6	10.6
9.00	9.02	125.7	730.8	18.3	662.8	10.3	11.3

Table 5.3: Some parameters of interest are calculated from the data in Table 5.2. R_{hot} is the hot resistance of the coil. T_{avg} is the average temperature calculated using the ratio of the hot and cold resistances. P is the electrical power supplied. ΔT_{oil} is the temperature difference between oil entering and leaving the motor. P_{oil} is the heat absorbed by the oil leading to ΔT_{oil}. ΔT_1 and ΔT_2 are both temperature differences between the end-turns and the oil inlet temperature.

Chapter 6

Prototype Motor Fabrication

The fabrication of our liquid cooled separated end-turn motor presented several challenges. We had to find practical ways to wind coils with separated end-turns and pot only the long sections of the coils in epoxy. Sealing the end-turn housings so that oil did not leak out was another critical challenge.

Most of the final prototype was made at Anorad Corporation's linear motor facility. My sincere appreciation goes to Fred Sommerhalter of Anorad Corporation who contributed many brilliant fabrication ideas and did a wonderful job machining many of the motor parts.

6.1 Coil Winding

The separated end-turn coil is a key part of our best cooling system designs. It allows each layer of the coil to be directly cooled, and this is what makes cooling techniques based on this type of coil so effective.

The first prototype separated end-turn coil made is shown in Figure 6-1. It was made with the bobbin shown in Figure 6-2 which has slots in one end-turn. These slots were made using a circular saw and cutting in from both sides of the piece. After winding the first layer of the coil, a metal shim was slid into the first slot. As the next layer of the coil was wound, it was separated from the previous layer by this shim. We used bondable polyester-imide magnet wire from MWS [19]. This wire has

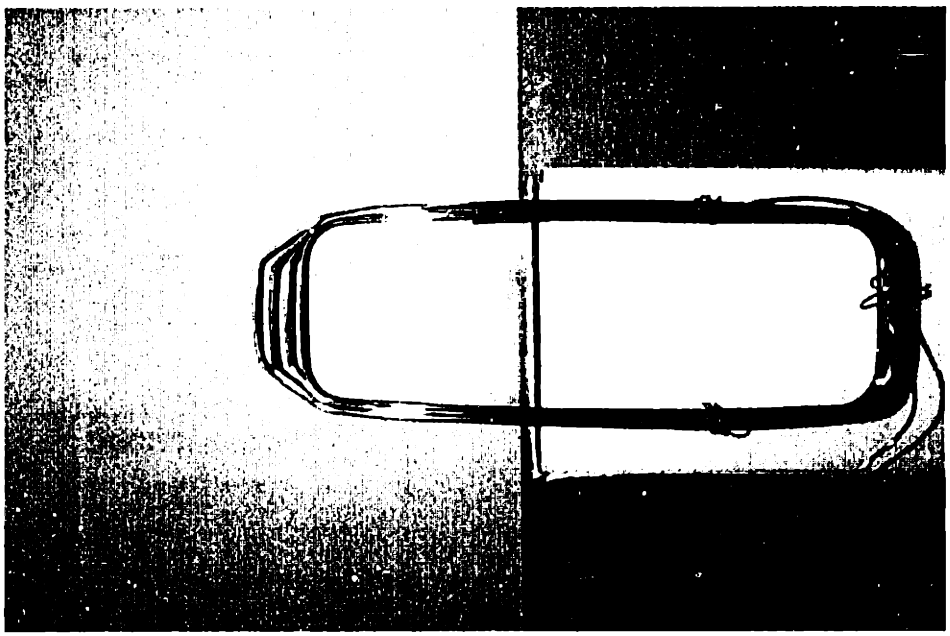

Figure 6-1: This was the first successful separated end-turn coil made in our laboratory. The four layers are separated on one end-turn. It was wound with the bobbin shown in Figure 6-2.

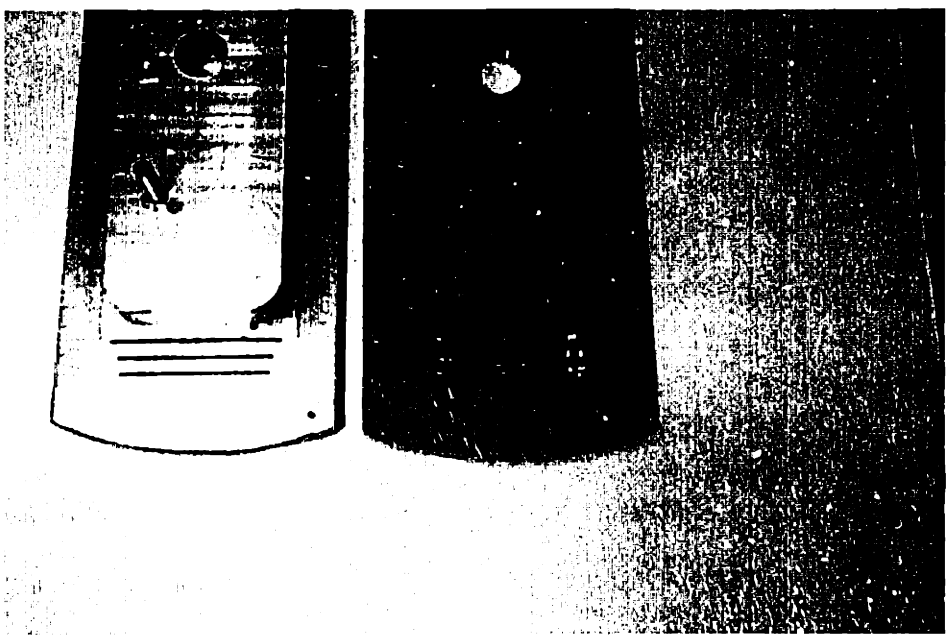

Figure 6-2: The two halves of the bobbin used to wind the coil shown in Figure 6-1 are shown. Note the three slots in the end-turn where shims were inserted during the winding process to separate the layers.

a polyester base insulation with a thermoplastic bond coat. After four layers had been wound, the coil was bonded by passing a current through it.

The fabrication process used on our motor coils was very similar to this. Instead of using a shim to separate each end-turn, we used two small pins—one to hold each corner of the end-turn. The final coil design was more detailed as well. It called for ten separations at both end-turns of the coil, and these separations were about the diameter of one wire. The coils were wound on a small NC winding lathe. It was programmed to wind two layers and then stop while the operator inserted the necessary four pins—two at each end. The pins and bobbin were coated in mold release so that the coil would not stick to them. It was important to make sure that the pins did not nick the previous layer as they were being inserted. When the coil was completely wound, it was clamped on the two long sides and bonded by passing a current through it. The current causes Joule heating which hardens the thermoplastic bond coat and causes the wire to hold its shape. Some of the initial coils looked like dogbones instead of rectangles because the end-turns flaired out too much. This problem was solved by adding another two layers to the coil. After some practice, one of these coils could be wound in about ten minutes. Figure 6-3 shows a separated end-turn coil made in this way. For high-volume production, a partially or completely automatic way of inserting the pins would reduce the winding time significantly.

The three separated end-turn coils were next potted in epoxy using vacuum pressure impregnation. This is commonly done to coils to give them strength, improve heat-transfer, and protect them against vibration, dirt, and nicks [30]. In our case, we had the added challenge of keeping epoxy out of the end-turns while making sure the long sides of the coil were completely filled with epoxy. This was required so that oil could easily flow through the gaps in the end-turn but would not leak out through the coil. The end-turns were coated in mold release and the gaps were filled with Teflon shims during the vacuum pressure impregnation process. After the epoxy had set, the thin film of epoxy which had formed around the end-turns was removed leaving the end-turns free of epoxy.

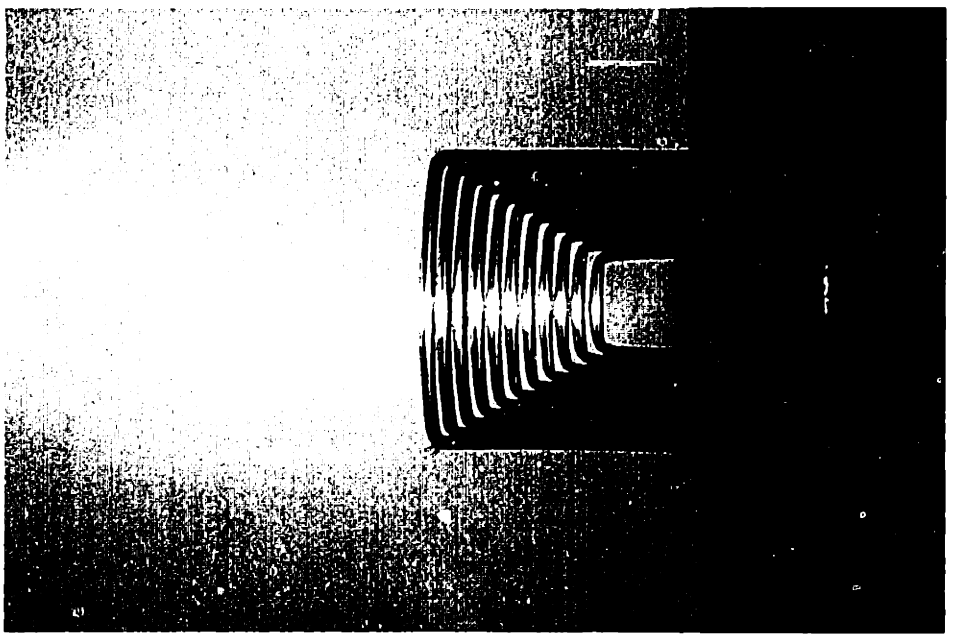

Figure 6-3: One half of our final separated end-turn coil design is shown. The coil consists of 22 layers which are separated into 11 groups of two at both end-turns. Grouping them in twos cut down the end-turn size while still allowing each layer to be directly cooled.

6.2 Coil Housings

The coil housings enclose the coils' end-turns. They must allow oil to flow through the end-turns in succession so that the coils are cooled. Additionally, the housings must form a tight seal around the end-turns so that oil does not leak out. Finally the housings must sustain the force generated in the coils and transfer it to the moving slide.

A baffle design developed by Fred Sommerhalter was used to steer the flow of oil through each end-turn. Aluminum was a natural choice for the housing material since it is easy to machine and would not be attracted to the magnets. The upper housing and oil flow is shown in Figure 6-4. The oil first flows through the end-turns in the top housing. The pockets connecting the end-turns are sized so that their cross-sectional area equals the total area of the gaps in the end-turns thus providing for a smooth fluid flow. When the oil has reached the end of the upper housing, it enters two copper tubes which carry it to the lower housing. Two tubes were used to

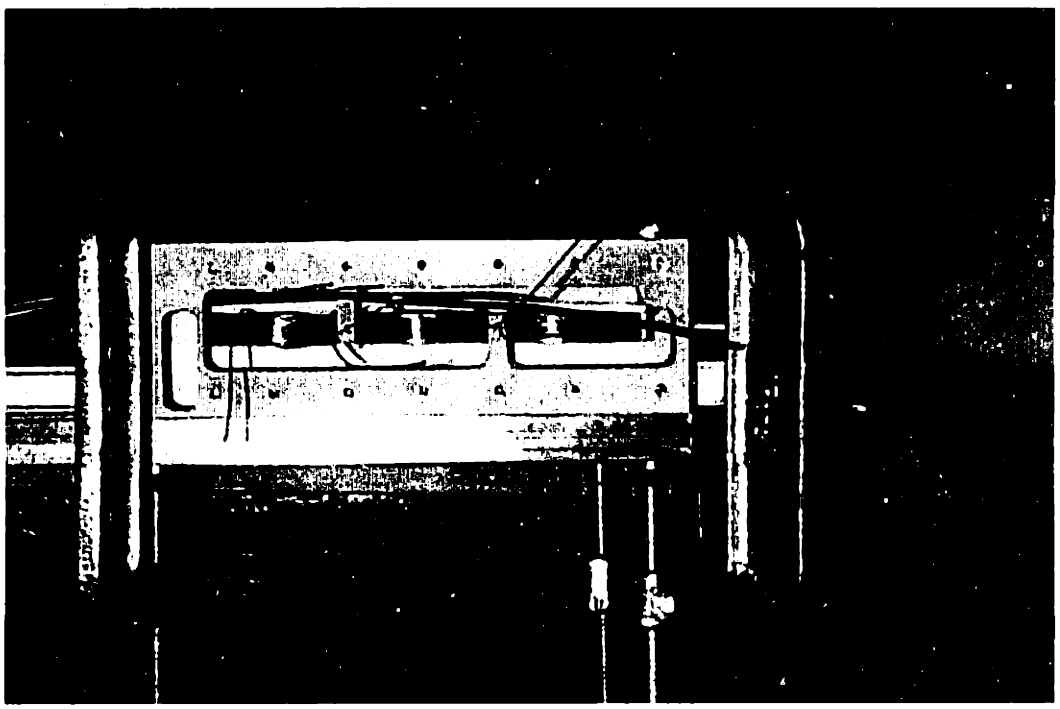

Figure 6-4: The upper housing of the coil assembly is shown holding the top end-turns of the three motor coils. Oil flows into the compartment above the left coil through a passageway inside the housing, not visible here. From there it flows down through the first coil, up through the second, and down through the third being directed by the baffle geometry shown. At the far right are two copper tubes which carry the oil to the lower housing. The rectangular pocket on the far left accepts oil returning from the lower housing via copper tubes on the left, and connects to the oil out nozzle.

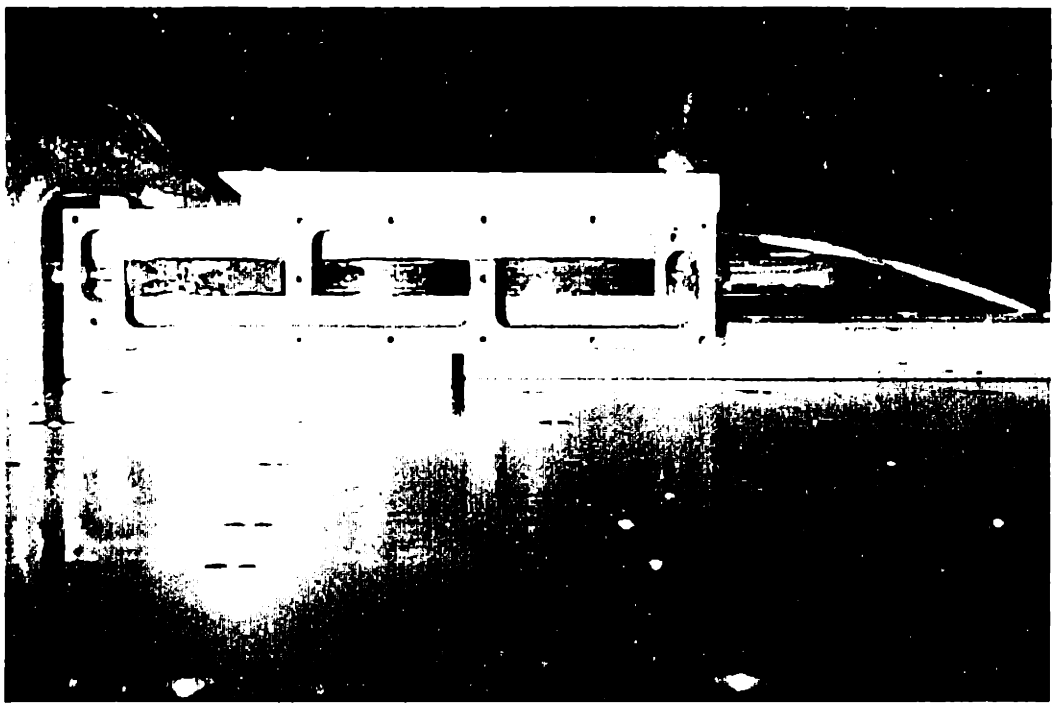

Figure 6-5: The lower housing directs oil through the three lower end-turns. Oil enters on the left coming from the upper housing via copper tubes. After passing through the end-turns it returns to the upper housing via copper tubes on the right. The housing cover is removed in this picture to show the baffles.

approximate the required cross-sectional area of the flow. One larger tube would not fit in the magnet channel. When the oil reaches the lower housing, it flows through the three lower end-turns (Figure 6-5) and returns to the upper housing via copper tubes. From here it leaves the motor via the oil out nozzle. This last set of copper tubes is required because an oil out nozzle mounted on the lower housing would be difficult to connect to since it is covered by the magnet array during motor operation.

6.3 Assembly

6.3.1 Coil Assembly

We put the end-turns of the coils and the copper tubes into the upper and lower coil housings. The housings were clamped down, and the coils and copper tubes rested on a flat piece of metal (Figure 6-6). We applied a structural epoxy to the joints

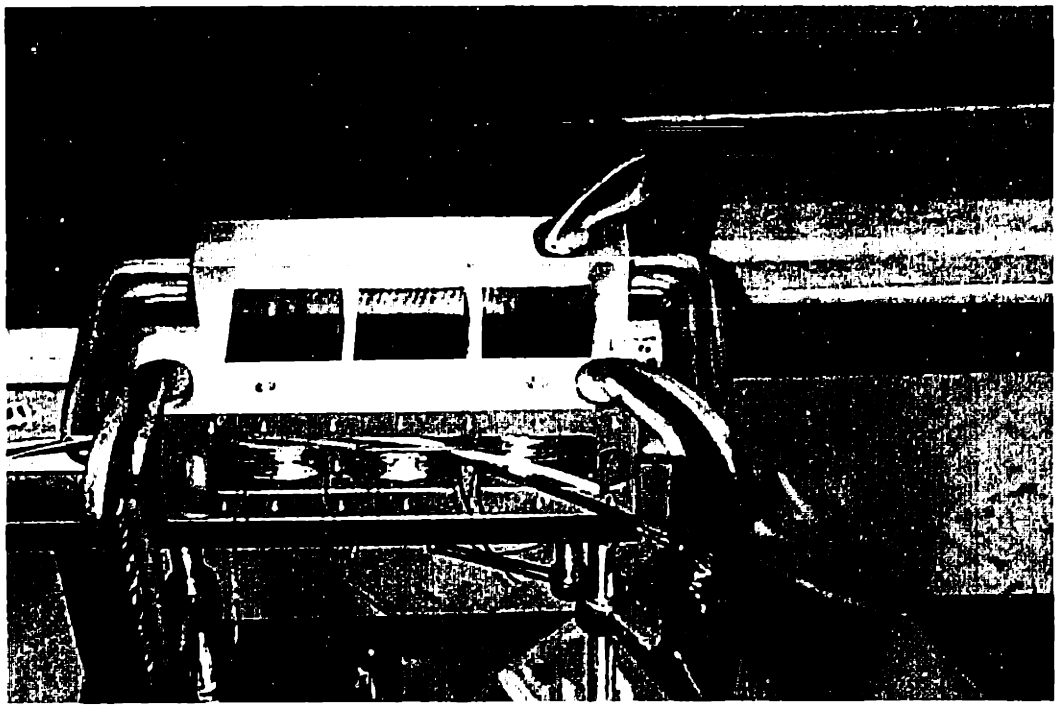

Figure 6-6: The coils, upper and lower housings, and copper tubes are being epoxied together. The wiring of the coils is not yet complete.

between the coils and housings and between the copper tubes and housings. When this had set, we applied epoxy to the other side of the assembly.

We soldered the finish leads of each coil together to form the neutral connection of the wye-connected motor. The three start leads were soldered to red, white, and black wires which leave the motor through a hole in the upper housing. We installed two thermocouples in the top end-turn of the first coil. These are used in the heating tests. When the wiring was complete, we screwed in the inlet and outlet oil hose fittings.

A high voltage (500 V) was placed between each motor lead and ground to make sure there were no shorts to ground. Unfortunately, the red lead was shorted to ground. It turned out the coil shifted in the housing as the epoxy was setting and crunched the start lead. We were able to shift the coil back and insulate the start lead so that the motor was fully insulated from the housings.

Next, we applied RTV silicone rubber adhesive sealant to the top of the upper

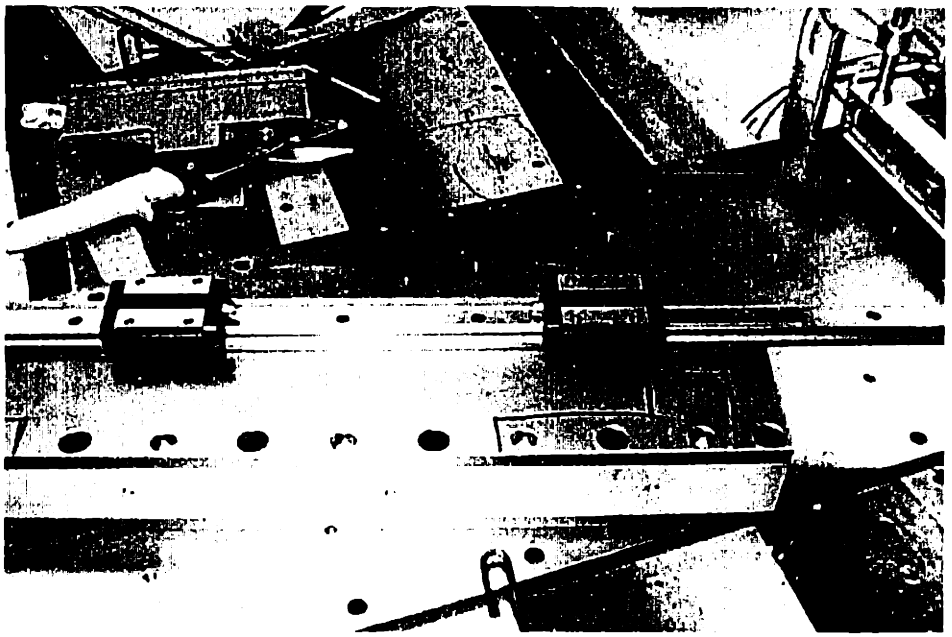

Figure 6-7: The NSK rail is mounted directly to the side of the U-shaped magnet channel.

housing and the bottom of the lower housing. We screwed the housing covers in place squishing the sealant. The top cover was made of Lexan to allow visualization of the oil flow through the baffles. Air at low pressure was blown through the sealed housings to check for leaks. They held the air pressure.

6.3.2 Bearings

The magnetic back iron was thick enough to resist bowing inwards due to the magnetic attraction of the opposing magnets as shown in Figure 6-7. Thus, we were able to mount an NSK bearing rail directly onto one side of the magnet channel. The coil assembly was attached to the ball bearings with a few pieces of aluminum stock. A removable stop was added to the moving coil assembly, and this butted up against hard stops mounted to the magnet array. This is shown in Figure 6-12.

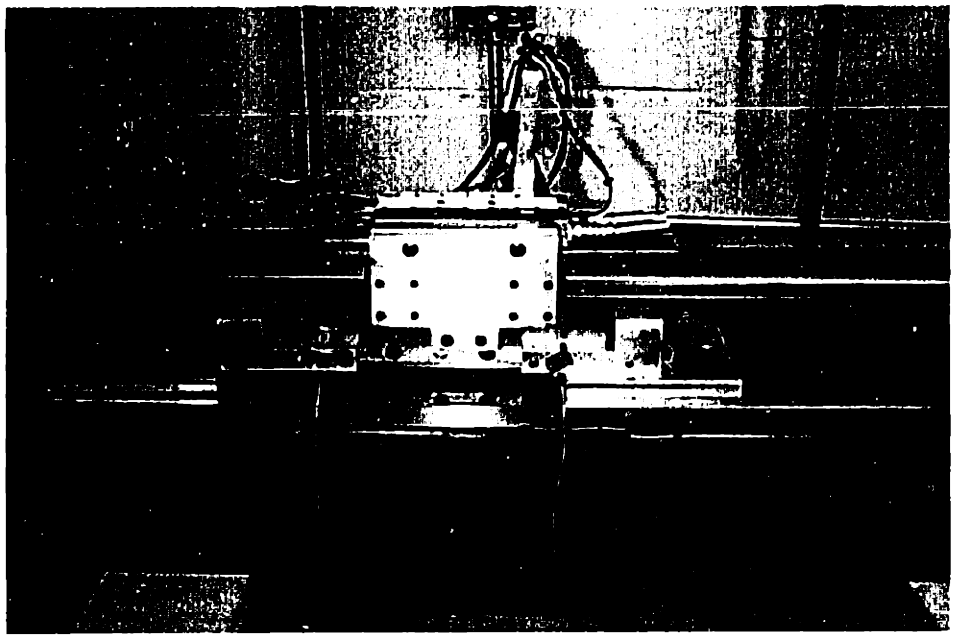

Figure 6-8: The complete motor is shown mounted to a weldment.

6.3.3 Mounting

The motor was mounted onto a 400 pound weldment made of 3 box beams. The top and bottom of the weldment consisted of 0.75 inch thick steel plates which were ground flat. T-slots were machined into the top plate. The motor was mounted in an upright position, and the magnet channel was screwed into two aluminum pieces which were also connected to the T-slots in the weldment. The weldment and entire motor are shown in Figure 6-8.

6.4 Magnet Array

The coils ride in a U-shaped N-S magnet array fabricated by Anorad. It consists of a N-S array of Neodymium-Iron-Boron magnets with a remanence $B_r = 1.25$ T. The period of the magnet array is $l = 60$ mm. Each magnet block is 0.45 inches thick and consists of three 0.15 inch thick magnets stacked on top of each other. The magnets are 1.945 inches long. Enough space is left underneath the magnets to accommodate the lower housing. The iron backing is made of C1018 steel. A portion of the magnet

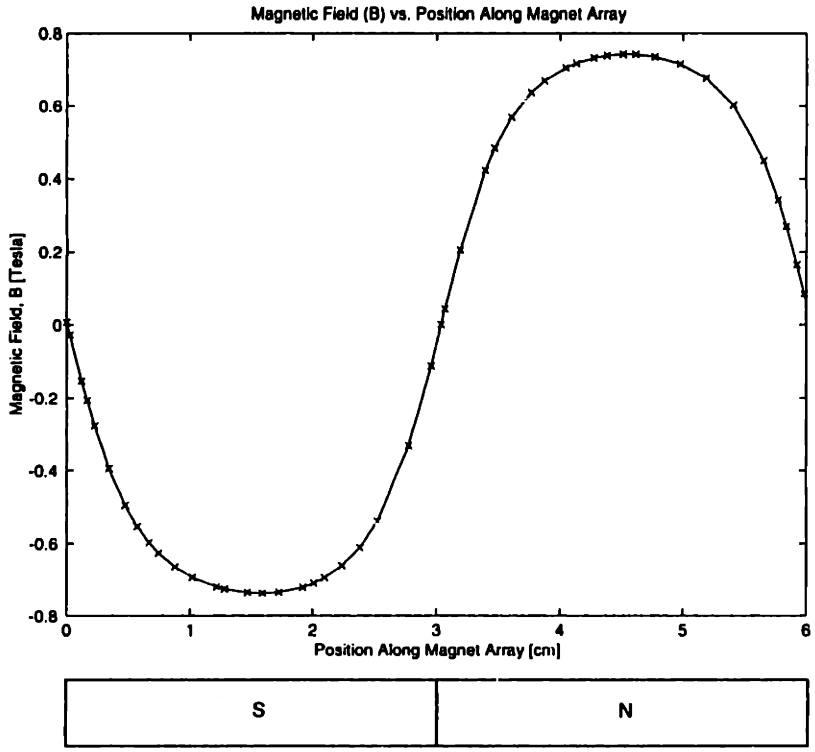

Figure 6-9: We measured the magnetic field B over one magnetic period $l = 6$ cm for the U-shaped magnet array of the linear motor. The gaussmeter probe was centered in the U-shaped magnet channel.

array can be seen in Figure 6-13.

6.4.1 Magnetic Field Measurements

We measured the magnetic flux of the U-shaped magnet array with an F. W. Bell Series 9550 Gauss/Teslameter. This device provides a constant current to a Hall Generator in the probe which produces a voltage proportional to the magnetic field. The 1× transverse hall effect probe was temporarily fixtured to the moving coil assembly. This allowed accurate position measurement via the Renishaw encoder attached to the coil assembly. The tip of the probe was positioned at the mid-height of the magnets and centered in the airgap. Figure 6-9 shows the flux over one magnetic period $l = 60$ mm. As expected it is approximately sinusoidal. Figure 6-10 shows the variation in the amplitude of the sine wave in Figure 6-9 for all the magnets in the array. The variation in the maximum magnetic field ranges from 0.7349 to 0.7740 T.

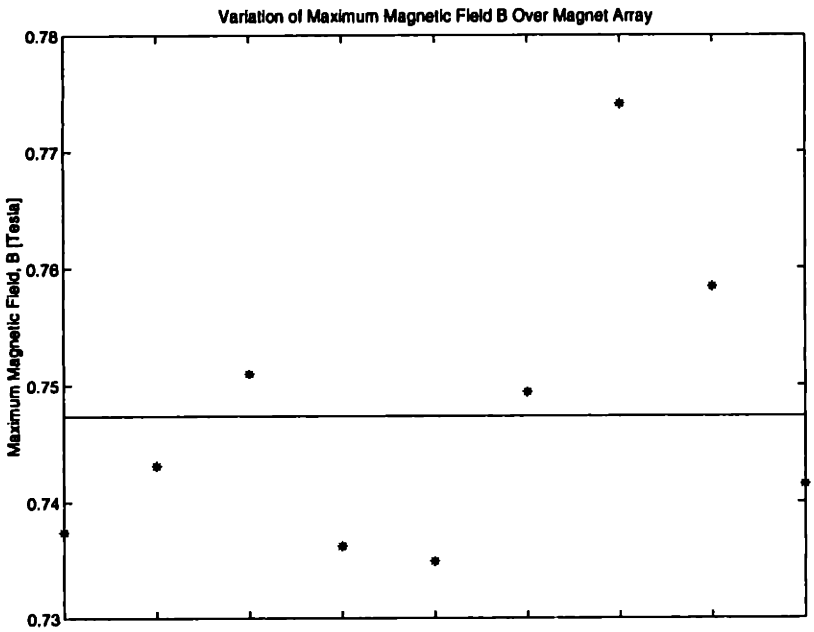

Figure 6-10: The absolute value of the maximum magnet field is plotted for each magnet block in the array. The average peak magnetic field is 0.747 Tesla.

The average maximum magnetic field over the entire array is 0.747 ± 0.013 T. This variation is likely due to the fact that each 0.45 inch thick magnet in the array consists of three stacked 0.15 inch thick magnets. This variation increases the force ripple in the motor.

The tangential magnetic field is significant near the boundary between two magnets with a peak magnetic field of 0.36 T next to the magnets. It is also interesting to note that the magnetic field of the U-shaped magnet array is well-contained. Figure 6-11 shows the fringing field out of one end of the magnet array. It dies down to 0.01 T in 2 cm. The magnetic field on the outside of the magnet channel back iron and under the motor is extremely low and ranges from 0.0006–0.0015 T.

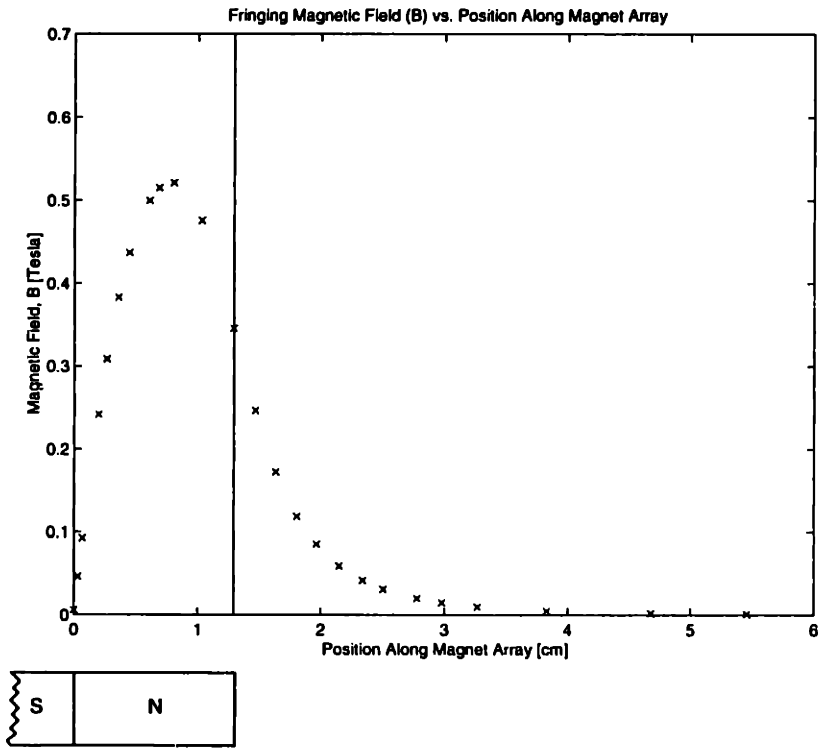

Figure 6-11: The fringing field at the end of the magnet array is shown. The end of the array is marked with a vertical line. Note that the end magnet is less than 1/2 the normal magnet length of 3 cm.

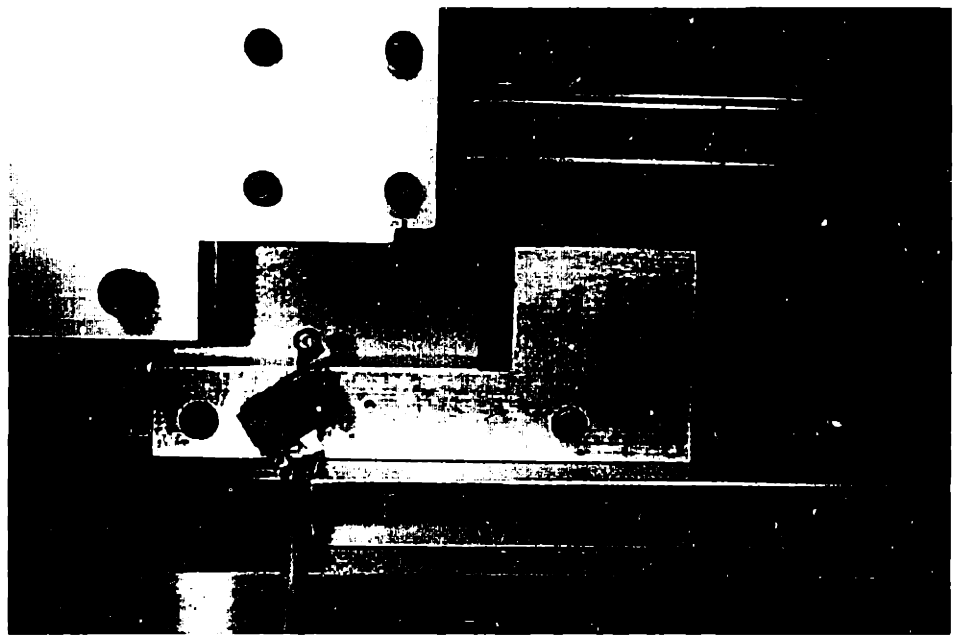

Figure 6-12: In the event that the motor goes unstable, the removable stop at the bottom of the coil assembly (left) will first strike a limit switch and then a hard stop. When activated, the limit switch inhibits the amplifier from commanding further motion in the direction of the hard stop.

6.5 Controller Hardware & Power Electronics

6.5.1 Power Amplifier and Commutation

An Anorad Sine Hall Mode PWM amplifier [2] is used to provide three phase power to the motor. This amplifier is used in current mode: an input voltage commands a constant force from the motor. The amplifier commutates the motor based on feedback from two Hall sensors. These are discussed further in the next section.

Two limit switches were installed on either side of the motor's travel before the hard stops. While triggered, they inhibit the amplifier from supplying force in the direction of the hard stop, but the motor can still be moved in the other direction away from the hard stop. A removable stop screwed into the moving coil assembly hits the limit switches and hard stops. This is shown in Figure 6-12.

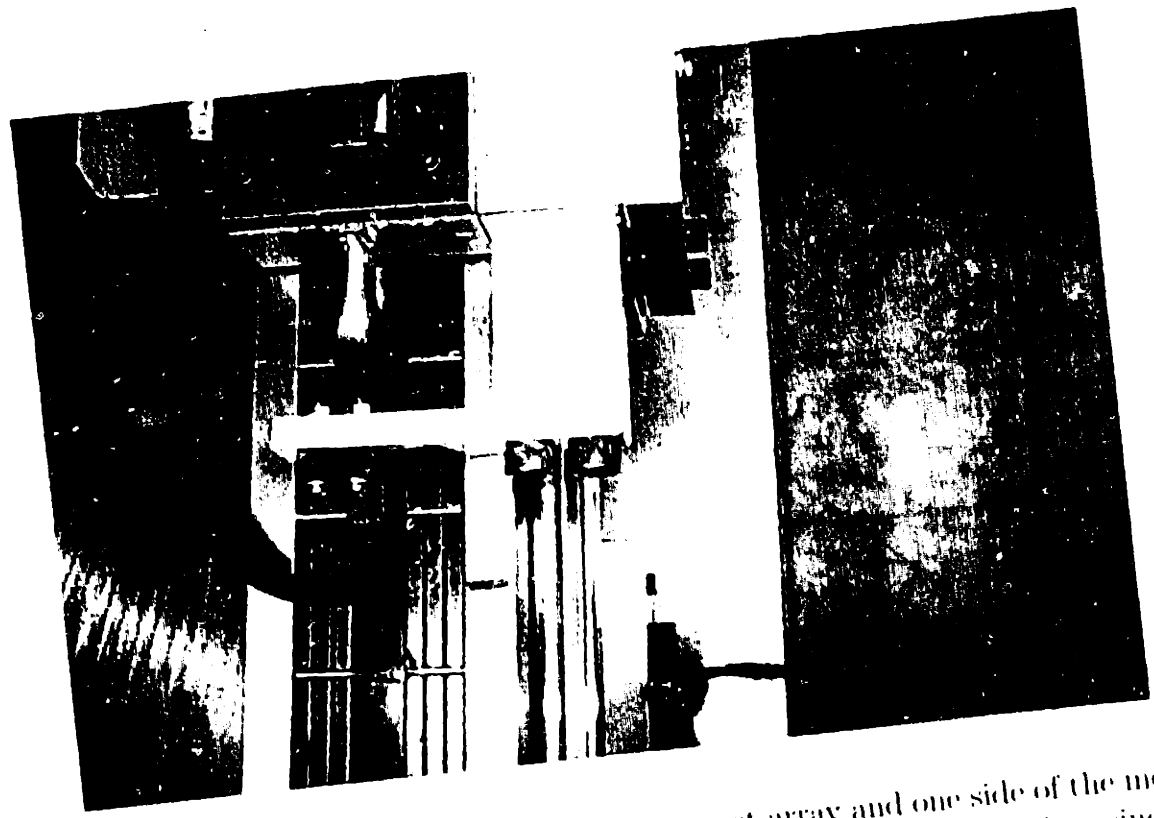

Figure 6-13: This picture looks down on the magnet array and one side of the moving coil assembly. The black hall effect sensor is mounted on an L-shaped piece since the copper tubes prevent mounting it directly onto the upper housing. Note also that each magnet block consists of three thinner magnets stacked on top of each other.

6.5.2 Hall Effect Sensors

Normally, the Hall effect sensors are mounted at the edge of the upper housing. On our motor, however, copper tubing for the oil flow was in the way. This required machining an L-shaped piece to attach the Hall sensor to the coil assembly. A close-up of the Hall sensor is shown in Figure 6-13. Since our magnet array field is stronger than those typically used with this Hall sensor, the Hall voltage generated is too large even when the Hall gain pot on the amplifier is at is minimum value. This problem is solved by placing a 14.99 kΩ resistor along the positive power line to the Hall sensor. This effectively loads the current source and reduces the current to the Hall sensor resulting in a proportionately lower Hall voltage.

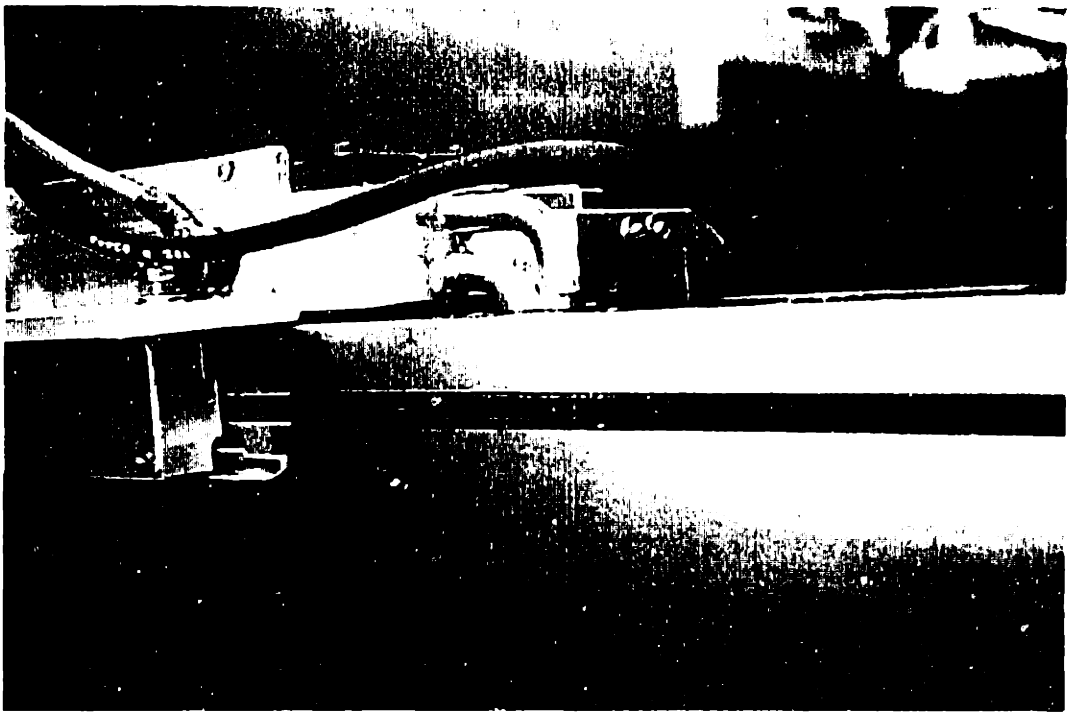

Figure 6-14: The linear encoder tape is stuck to the top of one side of the magnet array. The readhead is attached to the coil assembly.

6.5.3 Linear Encoder

A Renishaw linear encoder was mounted to one side of the magnet array (Figure 6-14). A 1× readhead was used which has a 5 μm resolution and maximum velocity of 5 m/s. It provided a quadrature signal to a Technology 80 5312B encoder card [31] for a PC which provides a position in counts to the control program. The encoder resolution of 5 μm turned out to be coarse for our 100 Hz controller. A change in position of 5 μm led to a noticeable spike in the command voltage to the motor because a 5 μm position error is significant to our controller. This command noise exhibits itself as a growling noise when the motor is moving slowly or reacting to a disturbance force.

Chapter 7

Control

Our linear motor is modeled as a free mass. A Renishaw linear encoder provides a position feedback signal which is counted by a Technology 80 [31] encoder card. The position is then accessible to a digital lead-lag controller implemented in C and running on a 90 MHz Pentium computer under MS-DOS. The controller has a 100 Hz crossover frequency and 2 kHz sample rate. It provides a command voltage to an Anorad sine hall amplifier which is running in current mode. The amplifier commutates the motor based on feedback from Hall effect sensors and drives it to produce a force proportional to the command voltage.

7.1 System Description

We model the linear motor as a free mass, M. This ignores the friction in the bearings and the small amount of eddy current damping due to the copper pipes. To check that this is a good approximation, we measure the frequency response of the open-loop system with an HP dynamic signal analyzer in swept sine mode. Figure 7-1 shows the setup for doing this. It is difficult to measure the open-loop response of a linear motor at low frequencies because the motor tends to wander towards one end of the travel. The Bode plot of the system is shown in Figure 7-1. The system consists of the amplifier gain K_a, the motor force constant K_f, the mass $1/ms^2$, and the position gain K_{vm} which is only needed for this meaurement. The position is measured by an

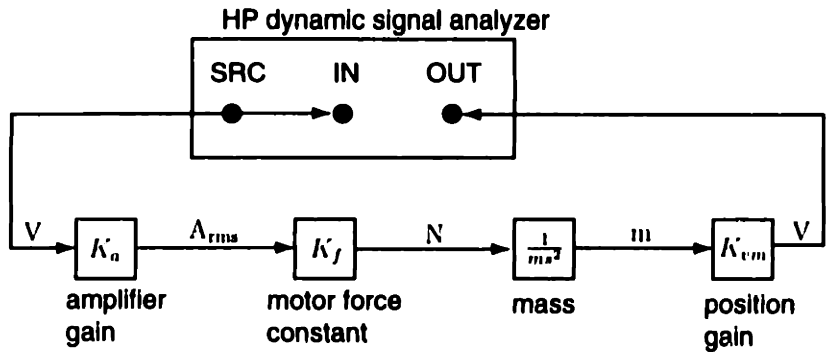

Figure 7-1: An HP dynamic signal analyzer was used as shown to measure the frequency response of the open-loop system. The Bode plot measured is shown in Figure 7-2.

encoder and enters the PC digitally via the encoder card. The software outputs this position as an analog signal with a gain of K_{vm}. This analog signal is then fed to the signal analyzer. As expected, the system Bode plot looks very much like a pure mass. The phase is between -160 and -180 degrees, and the magnitude falls off at approximately a -40 dB per decade slope.

The open-loop system Bode plot crosses 0 dB at $\omega = 49.3$ rad/s. From this information we can find an experimental value for the product of the amplifier gain, motor constant, and $1/m$. After dividing out the effect of the position gain implemented in the software, $K_{vm} = 39.37$ V/m, we are left with

$$\frac{K_a K_f}{ms^2} = \frac{61.73}{s^2} \tag{7.1}$$

which we will use when designing the controller.

7.2 Lead-Lag Controller

We took the emulation approach to designing a digital controller. Specifically, we design a continuous controller and then map it to discrete time. We can be confident that the discrete controller will approximate the continuous controller well since our sampling rate of 2 kHz is twenty times our crossover frequency of 100 Hz. A block

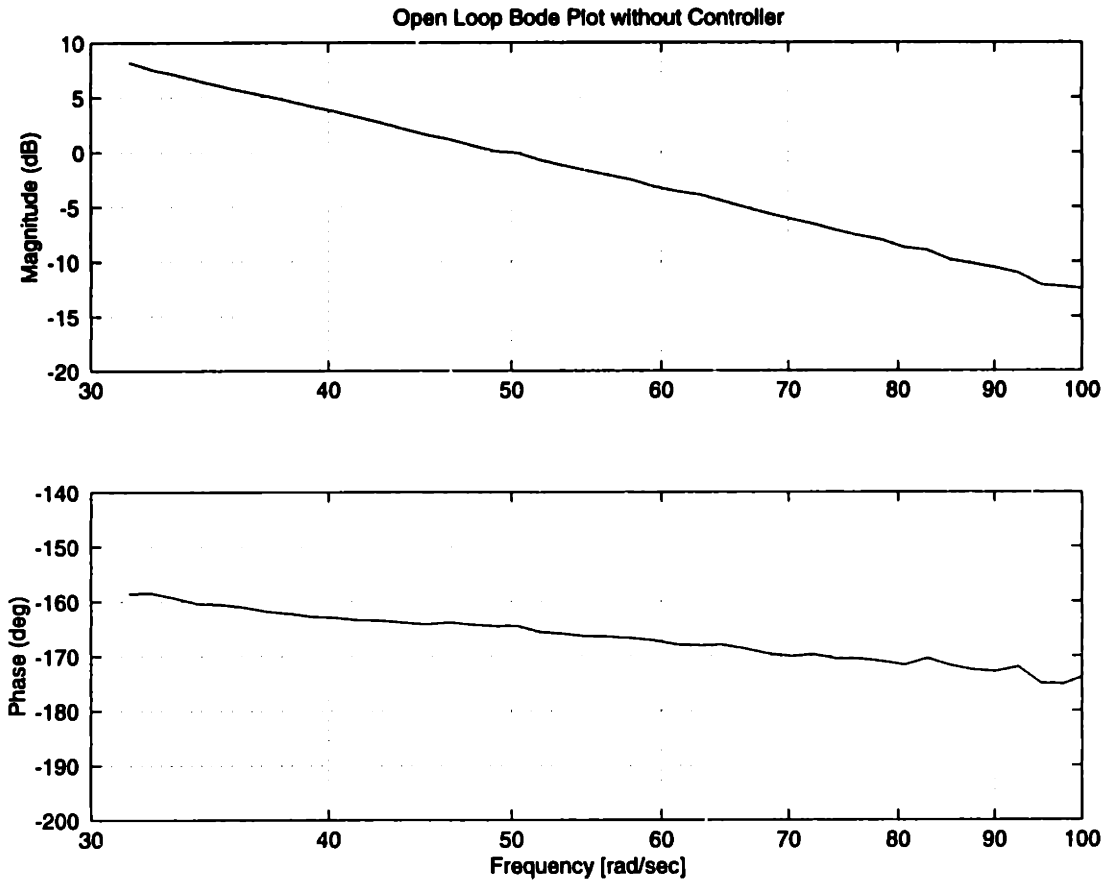

Figure 7-2: The open loop Bode plot measured by an HP dynamic signal analyzer (Figure 7-1) is shown.

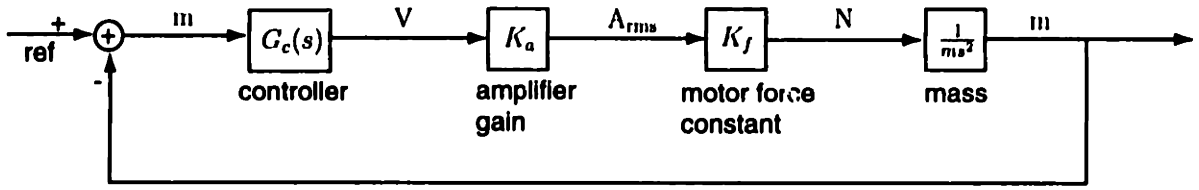

Figure 7-3: This is the block diagram of the closed loop motor control system.

diagram of the closed loop system is shown in Figure 7-3. Since a pure mass is a marginally stable system, we need to add damping with lead control. A lead ratio of 10 is chosen resulting in about 55° of phase lead. The zero and pole are chosen such that their geometric mean coincides with the crossover frequency of 100 Hz since this is where the phase lead is maximum. The lead term of the controller is

$$G_{lead}(s) = \frac{s + 198.7}{s + 1986.9}. \tag{7.2}$$

Lag control is added to improve steady-state response without affecting the phase margin too much. We place an integrating pole at $s = 0$ and put the zero a decade lower than the lead zero (which is conservative) at $s = -10$:

$$G_{lag}(s) = \frac{s + 10}{s}. \tag{7.3}$$

Now, a proportional gain is added so that the Bode plot of the open-loop system and controller crosses through 0 dB at 100 Hz. This is shown in Figure 7-4. The final continuous time controller is:

$$G(s) = 1.9899 \times 10^4 \left(\frac{s + 198.7}{s + 1986.9}\right)\left(\frac{s + 10}{s}\right). \tag{7.4}$$

Its closed-loop Bode plot is shown in Figure 7-5.

The matched pole-zero method [11] was used to convert equation (7.4) into discrete time:

$$G(z) = (1.9899 \times 10^4)\frac{(0.66755)(z - 0.9054257)(z - 0.9950124)}{(z - 1)(z - 0.3702970)}. \tag{7.5}$$

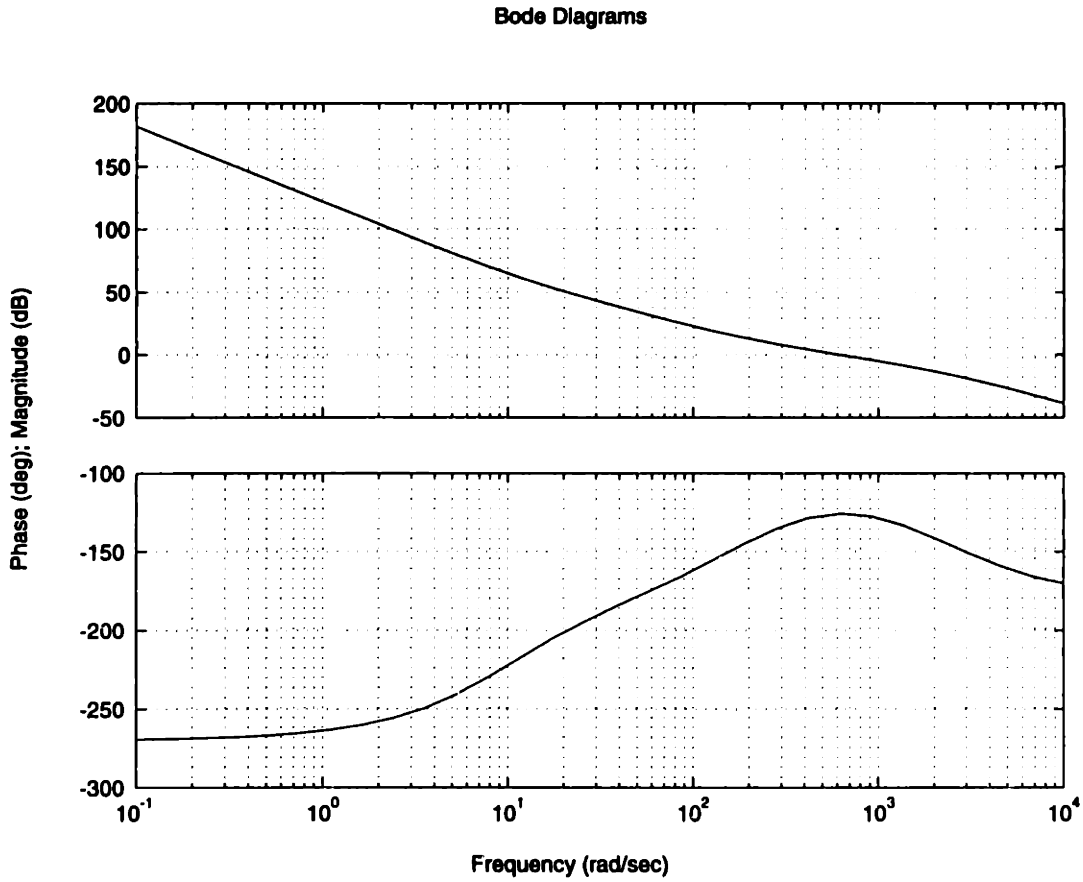

Figure 7-4: Loop Transmission Bode Plot.

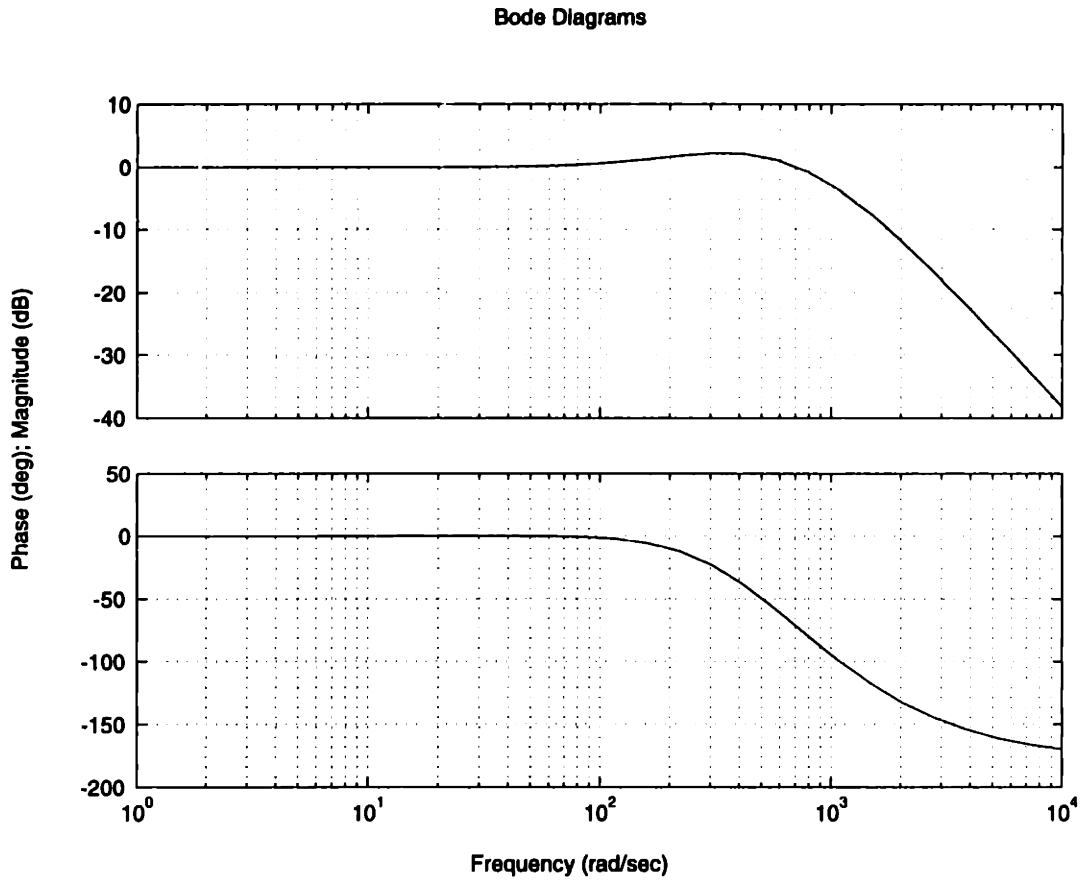

Figure 7-5: Closed-Loop Bode Plot.

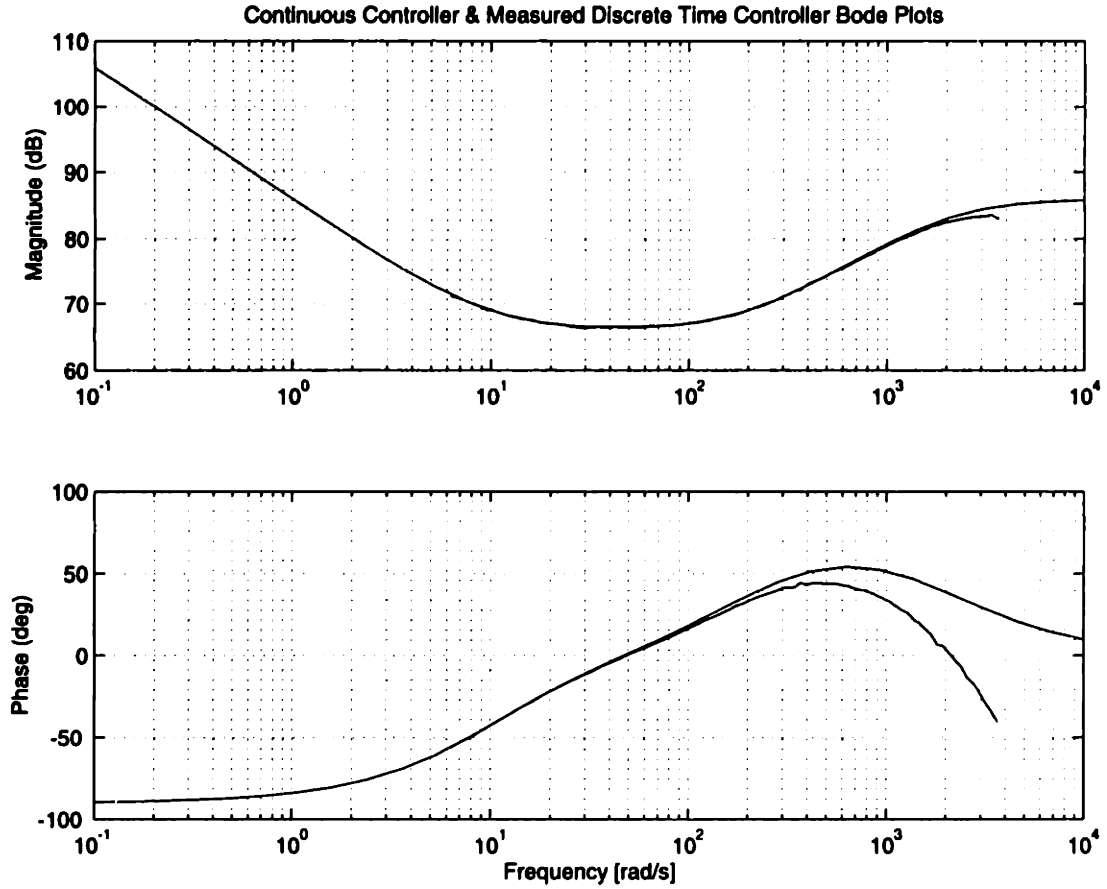

Figure 7-6: The discrete time Bode plot of the controller was measured with an HP dynamic signal analyzer and compared to the continuous time controller Bode plot. The drop in phase at high frequencies is due to the time delay associated with zero-order hold.

Originally, the controller was implemented as a second order difference equation. Figure 7-6 shows a comparison between the continuous time Bode plot and the actual discrete time Bode plot of the controller as measured by an HP dynamic signal analyzer.

Antiwindup was performed on the total control effort. This changed the difference equation resulting in a controller which would not saturate for large steps. Separating out the integral term from the controller so that antiwindup could be implemented only on it fixed this problem. To separate out the integral term, equation (7.5) can

be expanded as follows:

$$G(z) = (1.9899 \times 10^4)\left(\frac{5.0004 \times 10^{-4} z}{z-1} + \frac{0.67705309389807z - 0.60140524599019}{z - 0.37029696024295}\right) \tag{7.6}$$

This equation was implemented as a difference equation in an interrupt service routine which was called every 0.5 milliseconds. Figure 7.2 shows the essential code used to implement the difference equation (7.6).

7.3 Performance

A 100 μm step response is shown in Figure 7-8. The 5 μm quantization levels of the encoder are clearly visible. The delay due to the digital control is also apparent. Next, the motor was commanded to move a large distance of just over 12 cm with a trapezoidal velocity profile. The magnitude of the acceleration and deceleration were 20 m/s^2, or just over 2g's. The acceleration and deceleration occur over the first and last 2 cm of the motion. In the middle range, a constant velocity of 0.89 m/s is maintained. A plot of the reference and actual trajectories is shown in Figure 7-9. The entire move of over 12 cm occurs in approximately 0.17 s. A close-up of the trajectory and reference at the end of the deceleration is shown in Figure 7-10. The overshoot of the actual path beyond the final reference point is less than 150 μm.

In this chapter we have described the design of a digital lead-lag controller for our linear motor. It has a 100 Hz crossover frequency and a rise time of approximately 3 ms.

Our prototype linear motor uses direct oil cooling of separated end-turn coils. We next consider the second coil cooling technique, comb cooling, which, although viable, was not chosen for our prototype linear motor.

```
\\ essential control code from Interrupt Service Routine

ref = INITPOS - 0.01 * 5080;    // step of 0.01 inches from intial position

pos = te5312ReadCntr(AXIS);     // Read encoder position in counts.
                                // 1 count = 5 micrometers

err = ref - pos;                // calculate error
e   = err / 200000.0;           // convert from counts to meters

// difference equation for integral part of controller
u2  = (1.9899e4) * (5.004e-4) * e + u2old1;

// antiwindup only on integral term
if (u2 > INT_LIMIT)  u2 = INT_LIMIT;
if (u2 < -INT_LIMIT)  u2 = -INT_LIMIT;

// difference equation for rest of controller
// many significant digits are required for proper pole and zero placement
u1 = 0.37029696024295 * u1old1 +
     (1.9899e4) * (0.66705309389807 * e  -  0.60140524599019 * eold1);

u = u1 + u2;

// current limit
if (u > CUR_LIMIT)   u = CUR_LIMIT;
if (u < -CUR_LIMIT)  u = -CUR_LIMIT;

daout(0, u * (2047.0/10.0));    // output voltage u on D/A channel 0

u1old1 = u1;
u2old1 = u2;
eold1 = e;
```

Figure 7-7: The essential C control code from the interrupt service routine is displayed. This code is called every 0.5 milliseconds.

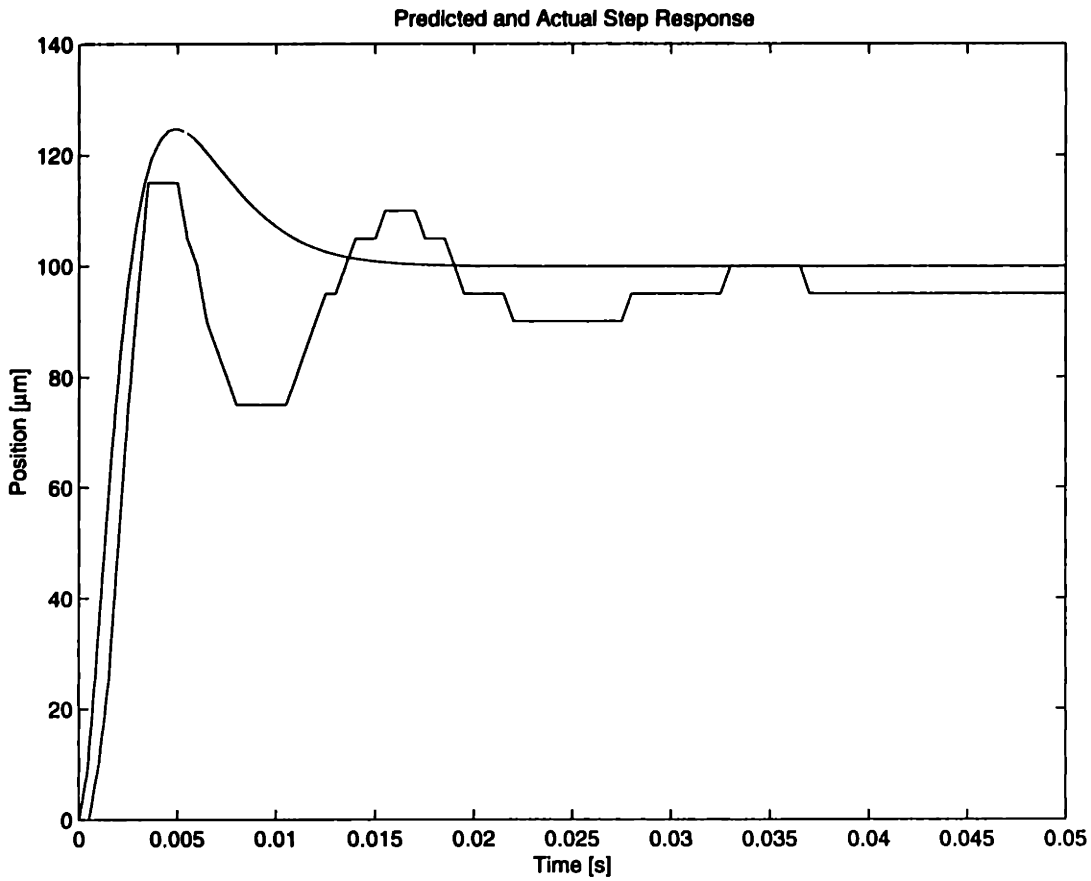

Figure 7-8: A 100 μm step response is shown. The 5 μm quantization levels of the encoder are clearly visible. Also shown is the predicted Matlab continuous time step response. The delay due to the digital control is visible. Also, the response is more lightly damped than predicted due to the extra negative phase from the zero-order hold.

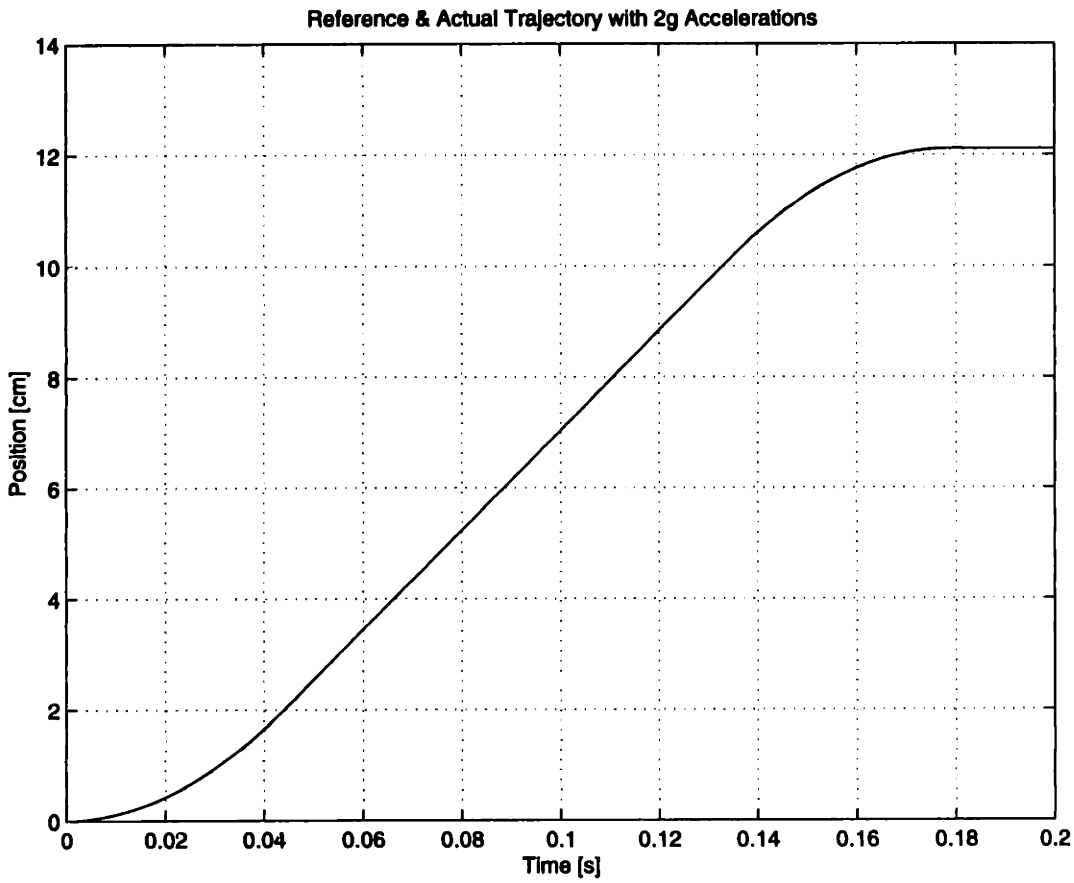

Figure 7-9: A contoured motion with a trapezoidal velocity profile is shown. The reference and actual trajectories lie on top of each other and are difficult to distinguish in this plot. The acceleration and deceleration have a magnitude of approximately 2 g's (20 m/s^2) and occur over the first and last 2 cm of motion. During the middle range of just over 8 cm, a constant velocity of 0.89 m/s is maintained.

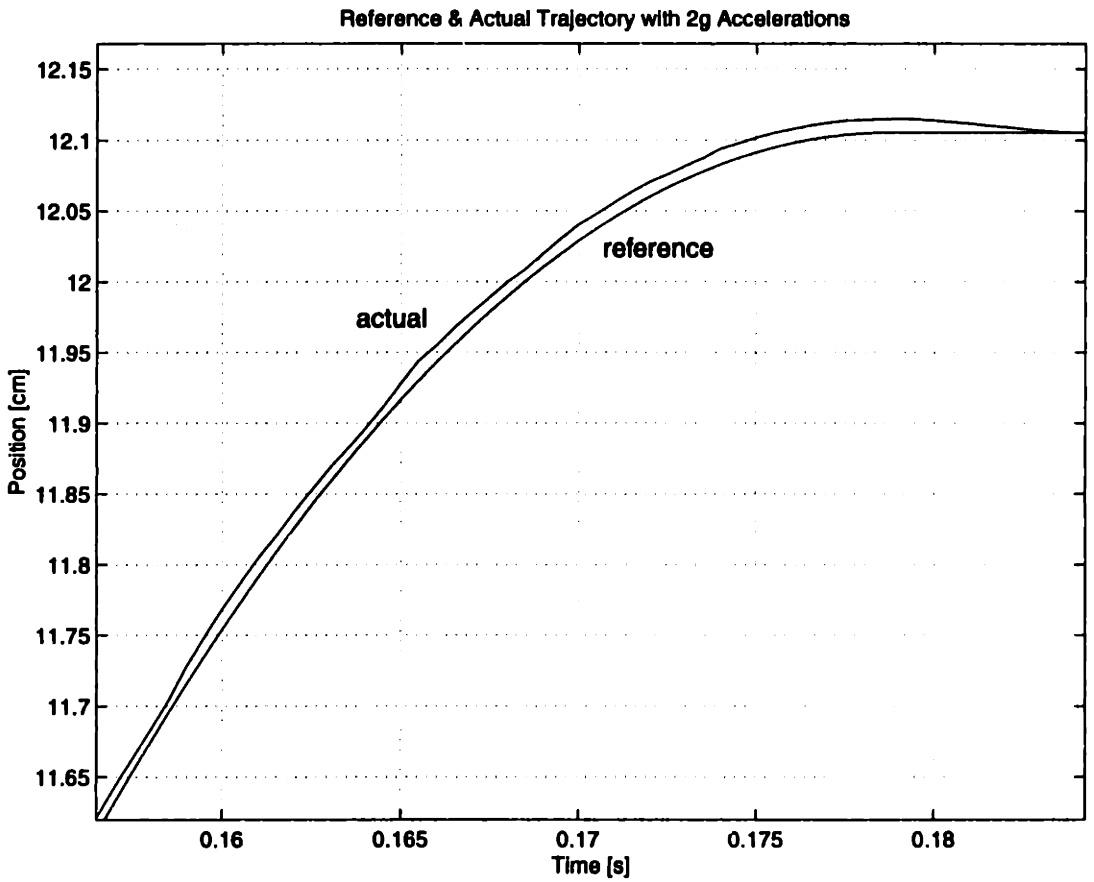

Figure 7-10: A close-up of the reference and actual trajectories at the end of the deceleration (Figure 7-9) is shown.

Chapter 8

Comb Cooling

Previously we have considered direct liquid cooling of a separated end-turn coil. We have looked at this technique in detail and seen that it does offer benefits in terms of maximizing current. However, from a practical point of view there are some concerns about this technique. It requires a closed oil circulation system which is costly and potentially hazardous to the rest of the machine if it leaks. While this cooling technique may be required in some cases, we can achieve a more practical solution without losing too much in performance.

This compromise between performance and practical issues is embodied in the technique of comb cooling. Comb cooling uses the same type of separated end-turn coil as we have already discussed. However, to avoid free flowing liquid contacting the coils, a comblike copper piece is inserted in the separated end-turns and the backbone of the comb is cooled by water. This cooling technique offers the following advantages:

- Comb cooling is effective because the fingers of the comb contact each layer of wire directly. Thus it eliminates the transfer of heat across layers common in conventional cooling schemes.

- Oil is no longer required since the cooling liquid never contacts the end-turns directly. Flowing water through the copper backbone is easy. This is similar to water cooling in many current motors and should not present significant reliability problems.

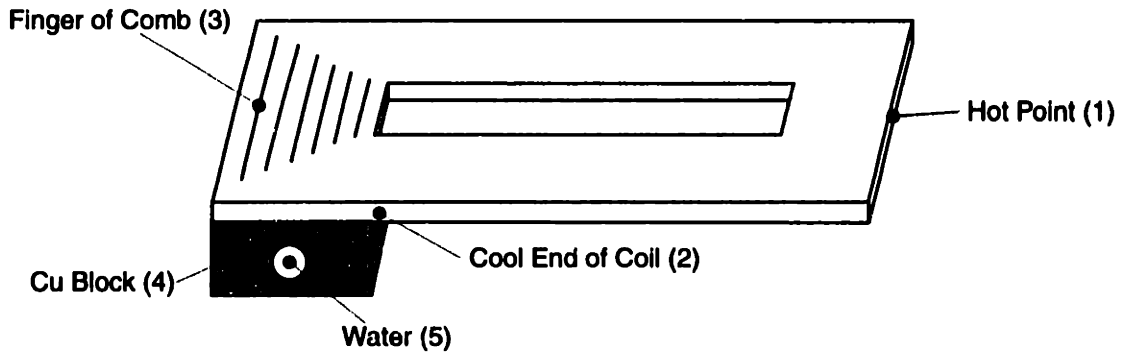

Figure 8-1: Some key points in the thermal model for comb cooling are shown. In experiments, thermocouples were placed at these positions.

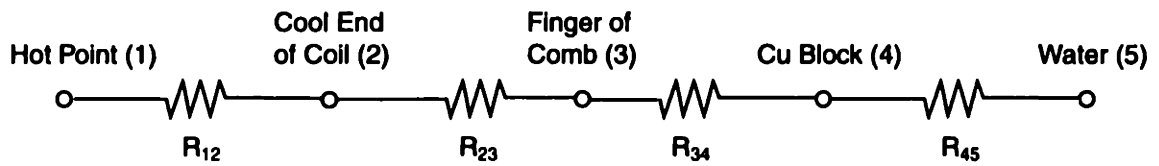

Figure 8-2: The thermal model for comb cooling is a series of thermal resistances between the points shown in Figure 8-1.

8.1 Thermal Model

The comb cooling technique was not used in our prototype motor. Nonetheless, we think it is a promising technique so we have made a prototype (section 8.2) and experimentally tested it (section 8.3). First, we develop its thermal model in this section.

In a comb cooled coil, heat first flows along the coil to the end-turn just as in a direct oil cooled coil. Next, it must flow from the end-turn to the comb's fingers which are copper shim. At this point it flows down the narrow fingers and into the copper block. Finally, it is transferred from the copper block to a flowing stream of water. Figures 8-1 and 8-2 show how we model this process by dividing the comb cooling heat path into four thermal resistances:

R_{12} This corresponds to the thermal resistance along the coil from the hot point to the cold point including the heat generation in the coil. This section of the

model is exactly what we have called "Region 1" in our previous discussions. We can see from equation (4.5) that the temperature difference is proportional to the heat generated (or current squared) just as the temperature difference across a thermal resistance is proportional to the heat flowing through it. This analogy shows that the temperature drop across this region is identical to the temperature drop across an appropriate thermal resistance.

R_{23} The heat must travel from the end-turn to the copper shim. In between these two are several layers of material such as wire insulation and bond, epoxy, and Teflon tape.

R_{34} The heat travels down the narrow copper shim towards the comb backbone (copper block).

R_{45} The heat must be convected away from the copper block by flowing water.

This completes the conceptual thermal model for comb cooling. Next, we present the fabrication technique for our prototype copper comb.

8.2 Fabrication

The first prototype comb was difficult to fabricate and somewhat crude. Nonetheless, it resulted in much better cooling than conventional water cooling. The method used to make the prototype is described here. The fabrication of the next comb is likely to be quite different.

1. We wound a separated end-turn coil just as we have described previously. Next, we milled a copper block, drilled a hole in it, and added pipe threads. During operation, water flows through this hole in the copper block.

2. We cut copper shims to fit inside the gaps in the end-turn. We sanded the edges so that they would not scratch the coil. Each copper shim was bent into a U-shape and filled two gaps. The bottom of the U provided contact area for

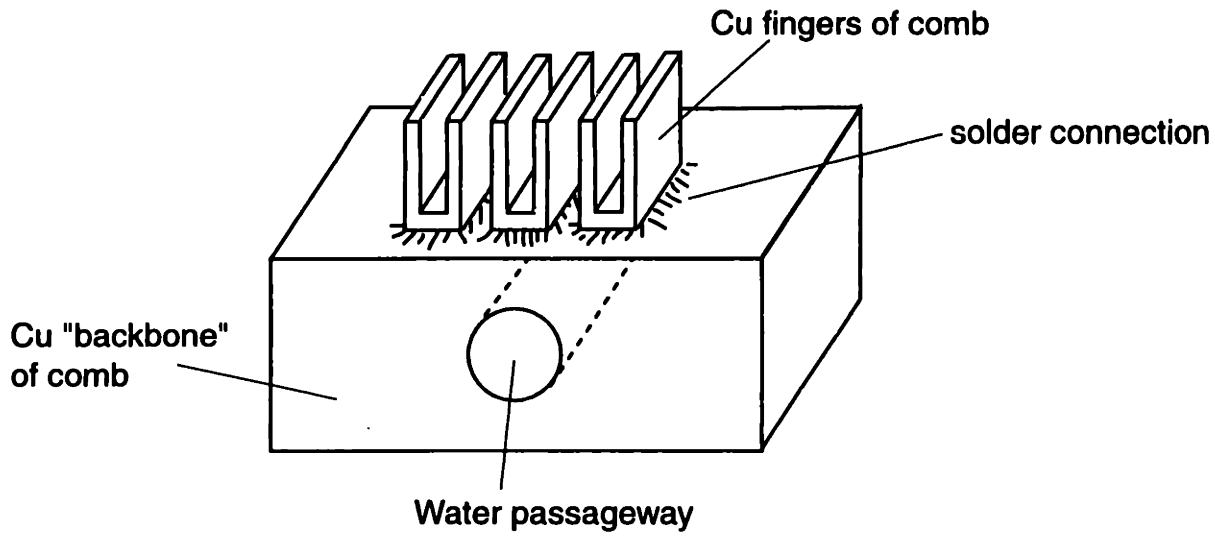

Figure 8-3: A schematic of the prototype comb is shown. The fingers are U-shaped so that there is sufficient area between them and the copper block to form a solder connection. The fingers are inserted into the gaps in the end-turns of a separated end-turn coil.

attaching the shim to the base. We formed the U-shapes by bending the copper shim around another piece of shim stock, placing the ensemble into a vise, and using a hammer to flatten the bottom of the U. Finally, we applied Teflon tape along each shim to insulate the comb fingers from the coil.

3. We polished the bottoms of the U-shaped fingers and the top of the copper block. A hotplate heated the copper block. We placed the U-shaped fingers into the coil's end-turns and rested them on top of the hot copper block. We applied solder to fasten the copper shim to the copper block.

4. We next epoxied the comb into place on the coil end-turn.

A schematic of a comb is shown in Figure 8-3. Figure 8-4 shows a picture of our prototype comb-cooled coil.

There are several improvements which, if implemented, would increase the performance of future combs:

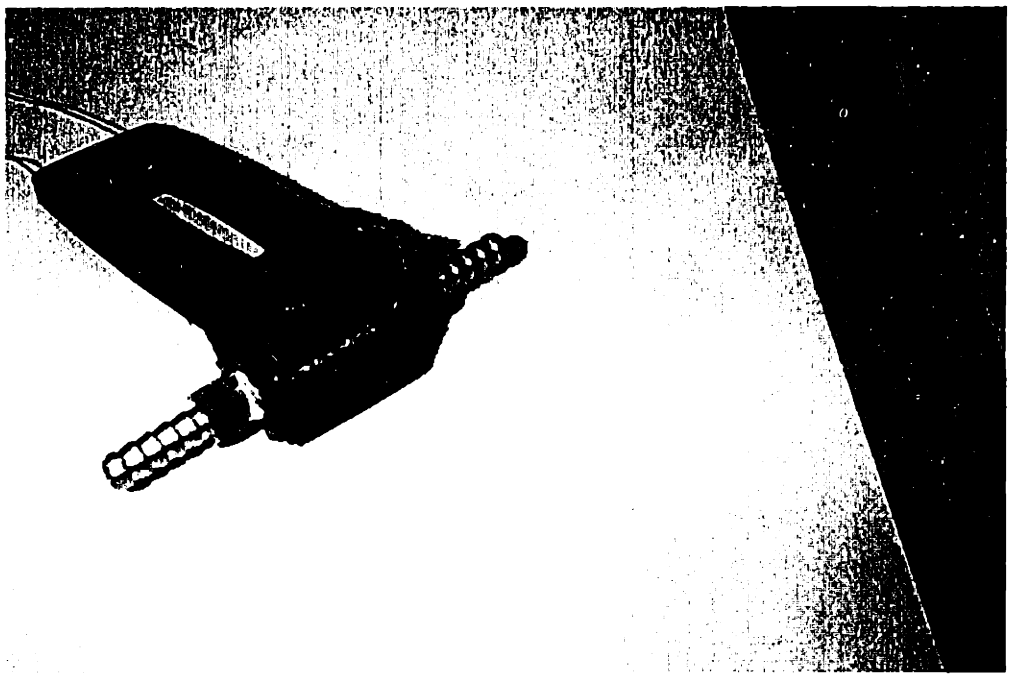

Figure 8-4: The prototype comb carries heat out of a separated end-turn coil via copper shims placed in gaps in the end-turns. The heat is then transferred to the copper block and removed by flowing water.

- Use thermally conductive epoxy instead of the electrical epoxy that was on-hand for this prototype. Epoxies with three times the thermal conductivity of the one we used are readily available.

- Use thicker copper shim. The copper shim used here was only 0.010 inches thick while the gap between end-turns was 0.025 inches. This undersizing made it easier to fabricate without scraping the end-turns. However, it is horrible from a thermal point of view since it adds huge thicknesses of epoxy to the thermal path from the end-turn to the finger, and decreases the cross-sectional area of the finger.

- Put combs on both end-turns of the coil instead of just one.

- On each end-turn there should be two backbones – one on above and one below the end-turn.

Description	Thermal R [K/W]	Prototype Experiment	Prediction for Prototype	Proposed Improved Implementation
Along Coil	R_{12}	0.85	0.83	0.21
End-Turn to Finger	R_{23}	0.61	0.55	0.04
Along Finger	R_{34}	0.14	0.14	0.04
Cu Block to Water	R_{45}	0.07	-	0.07
TOTAL	R	1.67		0.36

Table 8.1: Experiments run with the prototype comb cooling resulted in the thermal resistances listed under the column "Prototype Experiment." The next column over contains theoretical predictions for the conditions in the prototype experiment. The last column shows the thermal resistances after the improvements made in the text are made. It is derived by appropriately scaling the experimental data. All numbers are thermal resistances in units of K/W.

A key idea for future comb manufacturing processes is to wind the separated end-turn coil directly onto the comb fingers. This is attractive because it ensures that there will be no gap between the end-turns and the fingers. Also, there will be much less possibility of scratching the coil since the comb does not have to be inserted into the end-turns.

8.3 Experimental Results

The maximum current that could be passed through the uncooled coil at an average temperature of 125°C was 1.6 A. When water was flowed through the comb, the maximum current at 125°C was 3.8 A or 2.4 times the uncooled current. Conventional water cooling techniques only allow for a current of 2.3 A or 1.4 times the uncooled current.

Comb cooling can offer better performance than that resulting from our prototype. The first prototype was crude in several regards. If the improvements discussed next are made, comb cooling should be able to sustain 7.5 A or 4.7 times the uncooled current. Table 8.1 summarizes the experimental results and predicted improved values for the thermal model. The comb's thermal model broke the comb cooling process into a series of thermal resistances which are listed in the table. Next, we discuss the

improvements that can be made to lower each thermal resistance.

8.4 Improvements to Prototype

R_{12} This temperature drop along the coil is identical to the "Region 1" problem considered in direct liquid cooling. Theory predicts this kind of temperature drop very well (Figure 5-3), and the only way to decrease the temperature drop is to shorten the length of wire over which it occurs. A clear way to do this is to place combs on both sides of the coil. This reduces the effective Region 1 length by slightly more than two. From equation (4.5)[1], we know that the temperature drop goes as the length squared. Thus, we can conservatively estimate a factor of four drop in this thermal resistance which is what is shown in the table.

R_{23} This resistance is far worse in the prototype than it needs to be. In the prototype, the comb fingers are 0.010 inches thick while the gap between end-turns is 0.025 inches thick. Ideally the fingers would be as close as possible to 0.025 inches thick, the gap width, as well. In our case, they were made thinner to make it easy to slide them into the coils on this first prototype. Before the epoxy was applied, the coil with a comb in it was heated up. The coil end-turns got quite hot but the comb fingers were still cold. This was to be expected because the thermal resistance between the two was huge due to large air gaps although it is difficult to know if the fingers were centered in their gaps. The application of epoxy helped somewhat, but on average, 0.005 inches of epoxy still existed between the coil and copper finger. Three improvements are applicable here:

1. Make the finger thicker so that the epoxy layer is as small as possible. In the table we assume we can reduce the thickness of epoxy from 0.005

[1]Note that we have chosen the simpler equation which does not contain the effects of a temperature dependent electrical conductivity. This equation is also more conservative than the one incorporating the temperarture dependence of σ in this application making it the clear choice for scaling laws like this.

inches to 0.001 inches thus improving the thermal resistance by a factor of five.

2. Use thermally conductive epoxy. The epoxy used in the prototype comb had only 1/3 the thermal conductivity of that which was used for the coils in our motor. This would cut the thermal resistance by a factor of three.
3. Use a different, thinner insulator than Teflon tape. A sheet of Nomex-Kapton-Nomex would probably work well.

R_{34} The heat must flow down the fingers to the copper backbone. There are two improvements here:

1. Again, make the fingers thicker (by approximately a factor of two). This will double the cross-sectional area of the finger and halve the thermal resistance.
2. Implement a double-sided comb with two backbones—one above and one below the end-turn. This cuts the length of the heat flow along the finger in half and therefore also halves the thermal resistance.

R_{45} This is already quite efficient as the flowing water is in direct contact with the copper which is an excellent thermal conductor. If we wanted to reduce this further, we could increase the surface area of the hole by either making it bigger or giving it a rectangular shape. We might also slighty improve the heat-transfer by increasing the speed of the flow.[2]

8.4.1 Total Resistance

For the prototype experiment, the total thermal resistance was found to be 1.67 K/W. Assuming a 100 K temperature rise and 5 Ω hot resistance of the coil, this predicts a maximum current of 3.5 A. If we make all of the improvements outlined above, the

[2]This will certainly increase the amount of heat that can be drawn away, but its effect on the thermal resistance is minor.

total thermal resistance decreases to 0.36 K/W. This allows a maximum current of 7.5 A or 4.5 times the uncooled current.

Chapter 9

Conclusions and Suggestions for Future Work

9.1 Conclusions

The goal of this thesis is to push the thermal limit in linear motors. We saw that conventional cooling schemes require heat to flow across coil layers before reaching the cooling medium. The resistance between these layers is significant, and the temperature rise goes as the number of layers squared. To avoid this problem, we formulate a simple design rule: *We must cool each layer of the coil directly.* This leads to a coil design with gaps between successive end-turn layers. These gaps allow us access to each layer so we can cool it directly. Our primary focus has been on direct oil cooling of these separated end-turn coils. We built a prototype linear motor incorporating this cooling technique. Our design allows nearly 6 times higher force in steady state and dissipates 32 times as much heat as a free convection-cooled motor.

We develop a thermal model describing the temperature rises with direct liquid cooling. The model breaks a coil into symmetric quarters. Each quarter is further divided into two regions. Region 2 is the end-turn and models the Joule heating and convective liquid cooling. Region 1 is the long working portion of the coil and only contains Joule heating. This model is corroborated with thermal experiments which use many thermocouples embedded in coils to obtain temperature distributions.

We next describe the fabrication of our prototype motor including the winding of separated end-turn coils and coil housings which contain the oil. The motor has a force constant of 35.3 N/A_{rms} and a peak magnetic field of 0.75 T. At a force of 259 N, it dissipates 730 W with a peak current density of 3.47×10^7 A/m^2 in the wire.

Next, we consider an alternative cooling technique, comb cooling. A prototype comb consisting of a copper base and copper fingers is made and inserted into the gaps in a separated end-turn coil. We achieved 2.4 times the current of a free convection-cooled coil with this device.

We also develop a continuum electromechanical analysis for our motor. It extends the results of previous analyses which were done for ironless motors to our motor with back iron. The power optimal coil thickness is found to be $l/10$ where l is the magnet pitch length for a single-sided motor with magnet and coil back iron. By symmetry, the power optimal thickness of a U-shaped motor is twice that value, or $l/5$, which is also the answer in the single-sided ironless case. The power dissipated vs. coil thickness curve is flat near the minimum, so we have considerable leeway in choosing the coil thickness. In conventional motors we would choose a thin coil to avoid thermal problems; with our end-turn liquid cooling design it now makes sense to choose a thick coil since we do not pay any thermal penalty for thicker coils, and can achieve a higher thermally-limited force with the thicker coils. The designs presented in this thesis allow a dramatic increase in the power density of linear motors and thus may open new application areas for these devices.

9.2 Suggestions for Future Work

9.2.1 Direct Liquid Cooling of Separated End-turns

We have demonstrated a sixfold increase in the thermally-limited current with our direct oil-cooled prototype motor. Now that the basic research is complete, it would be exciting to start the development process so that this technique could make it out of the laboratory and into high-end commercial linear motors. It is likely some

users of linear motors would be happy to pay a significantly higher price for a motor that can produce the same force as a cheaper motor but in one sixth the volume. This would cover the extra cost associated with winding separated end-turn coils and making sure the oil circulation system is leakproof. Next we list some further incremental improvements that should be considered for any future prototype:

- We chose the coil thickness of our prototype motor to match other motors and ease the fabrication process. In the future, we should choose a much thicker coil. The power dissipation vs. coil thickness curve is relatively flat near the optimal coil thickness (Figure 2-5). Our cooling scheme works independently of the coil thickness unlike conventional coils. We are free to choose a thick coil which is advantageous because it requires less current density to produce the same force.

- When the oil-cooled motor reaches 100°C average temperature rise, the temperature rise between the oil entering and leaving the motor is 18°C. This temperature rise can easily be reduced by increasing the flowrate. Since our flowrate is a modest one-third gallon per minute, there is no reason why we can't quadruple it cutting the oil temperature rise to 4.5°C.

- Currently, our coils are spaced apart and encapsulated in epoxy. On some motors, metal bars are placed next to the working part of the coils to aid in the removal of heat. Although this is a conventional cooling technique in the sense that it cools across the coil layers, its addition might help. It will remove heat very well from the outermost couple of layers which have the longest length to the end-turns.

9.2.2 Comb Cooling

Comb cooling offers a nearly fivefold increase in the thermally-limited current. This is slightly less than with direct oil cooling, but comb cooling is a more practical solution since a comb-cooled coil uses water cooling of the comb, and the water does not make

contact with the coils. A coil with combs on the end-turns is packaged well and fits easily into a U-shaped motor. The first prototype we made was crude. Further work needs to be done to develop an improved fabrication process for an integral comb-cooled coil. This will almost certainly require that the fingers of the comb are wound into the coil, not inserted afterwards like in our first prototype. Winding the fingers directly into the coil ensures good contact between the end-turns and the fingers. We also want to have combs on both end-turns and use thermally conductive epoxy to fixture them to the end-turns. Each comb finger should be attached to two copper blocks—one above and one below each end-turn. (Our first prototype comb only had one copper block below the end-turn.) After the fingers are wound into the end-turns, we must have some method of attaching them to the copper blocks. One idea is to cut slots in the copper block so that the fingers fit into them. This would provide a lot of surface area for heat transfer. By sealing the joint between the finger and copper block, we could run water directly between the finger and an over-sized slot in the copper block. If these fabrication issues can be solved, comb cooling certainly promises a practical solution for overcoming the thermal limit in linear motors.

In conclusion, this thesis shows that a new level of power density is possible in linear motors. We present techniques applicable to the analysis of the electromagnetic and thermal performance of these devices, and thus provide a solid foundation for the further development of these devices.

Appendix A

Maple Code for Continuum Electromechanics

We use Maple [35] to do much of the algebra for the continuum electromechanics analysis in Chapter 2. Heck's book *Introduction to Maple* [17] explains how to manipulate expressions and make assumptions about variables so that Maple can properly simplify expressions using them. We do not include the Maple output in this Appendix because many of the intermediate expressions are several pages long. Note that the fields due to the magnet array are solved using the magnetic potential as Trumper, Williams, and Nguyen [34] have done. For variety, the fields due to the coils are solved using the vector potential as in Trumper, Kim, and Williams [33]. In Chapter 2 of this thesis we used the vector potential method for the fields due to both the magnets and coils.

A.1 Field Solutions for Magnets

A.1.1 System of Equations

```
> eq1 := ha = abs(k)*sa;
> eq2 := hc - hd = -mv;
> eq3 := hf = -abs(k)*sf;
> eq4 := hb = k*(-coth(k*Delta) * sb + (1/sinh(k*Delta)) * sc);
> eq5 := hc = k*((-1/sinh(k*Delta))*sb + (coth(k*Delta))*sc);
```

```
> eq6 := hd = k*(-coth(k*g) * sd + (1/sinh(k*g)) * se);
> eq7 := he = k*((-1/sinh(k*g))*sd + (coth(k*g))*se);
> eq8 := sa = 0;
> eq9 := sf = 0;
> eq10 := sa = sb;
> eq11 := sc = sd;
> eq12 := se = sf;

> eqs := eq1, eq2, eq3, eq4, eq5, eq6, eq7, eq8, eq9, eq10, eq11, eq12:
> vars := ha, hb, hc, hd, he, hf, sa, sb, sc, sd, se, sf:
> soln := solve( {eqs}, {vars} );
> assign(soln);

> simplify(expand(hd));
> I * k * simplify(expand(sd));
```

A.1.2 Solutions

```
> alpha := n -> (exp(2*k(n)*(x0+Gamma)) + exp(2*k(n)*Delta)
          -exp(2*k(n)*(Delta+x0+Gamma))-1) /
          (exp(2*k(n)*(Delta+x0+Gamma))-1);

> mhxnd := n -> (-1/2) * coth(k(n)*(x0+Gamma)) * mv(n) * alpha(n);
> mhznd := n -> (1/2) * I * mv(n) * alpha(n);

> mhxnd(-1);
```

A.2 Field Solutions for Coils

A.2.1 System of Equations

```
> equ1 := Ha = 0;
> equ2 := Hb = (k/mu0) * ( coth(k*Delta)*Ab + (-1/sinh(k*Delta))*Ac );
> equ3 := Hc = (k/mu0) * ( (1/sinh(k*Delta))*Ab + (-coth(k*Delta))*Ac );
> equ4 := Hd = (k/mu0) * ( coth(k*x0)*Ad + (-1/sinh(k*x0))*Ae );
> equ5 := He = (k/mu0) * ( (1/sinh(k*x0))*Ad + (-coth(k*x0))*Ae );
> equ6 := Hf = (k/mu0) * ( coth(k*Gamma)*Af + (-1/sinh(k*Gamma))*Ag )
               - (1/k)*((cosh(k*Gamma)-1)/sinh(k*Gamma))*Jy;
> equ7 := Hg = (k/mu0) * ( (1/sinh(k*Gamma))*Af + (-coth(k*Gamma))*Ag )
               + (1/k)*((cosh(k*Gamma)-1)/sinh(k*Gamma))*Jy;
> equ8 := Hh = 0;

> equ9 := Ha = Hb;
> equ10 := Hc = Hd;
```

```
> equ11 := He = Hf;
> equ12 := Hg = Hh;

> equ13 := Aa = Ab;
> equ14 := Ac = Ad;
> equ15 := Ae = Af;
> equ16 := Ag = Ah;

> equs := equ1, equ2, equ3, equ4, equ5, equ6, equ7, equ8, equ9, equ10,
          equ11, equ12, equ13, equ14, equ15, equ16:
> varus := Ha, Hb, Hc, Hd, He, Hf, Hg, Hh, Aa, Ab, Ac, Ad, Ae, Af, Ag, Ah:
> solnu := solve( {equs}, {varus});
> assign(solnu);

> simplify(Hd);
> (I * k / mu0) * simplify(Ad);
> expand(");
> normal(");
> map(simplify,");
> convert(",exp);
> map(simplify,");
```

A.2.2 Solutions

```
> beta := n -> (exp(2*k(n)*Gamma)-1)/(exp(2*k(n)*(Gamma+Delta+x0))-1);
> shznd := n -> (-1/2)*beta(n)*Jy(n)*exp(k(n)*x0)/k(n)
            *(exp(2*k(n)*Delta)-1)*exp(-I*k(n)*z0);
> shxnd := n -> (1/2)*I*beta(n)*Jy(n)*exp(k(n)*x0)/k(n)
            *(exp(2*k(n)*Delta)+1)*exp(-I*k(n)*z0);
```

A.3 Stress Tensor Force Calculation

A.3.1 Tangential Force

```
> assume(n, integer);
> assume(l>0);
> assume(Ja,real);
> assume(Jb,real);
> assume(x0, real);
> assume(z0, real);
> assume(Gamma, real);
> assume(M0, real);
> assume(Delta, real);
> assume(zeta,real);
```

```
> tothxd := n -> shxnd(n) + mhxnd(n);
> tothzd := n -> shznd(n) + mhznd(n);

> tothxd(1);

> k := n -> piecewise( n=1, zeta, n = -1, -zeta,0);
> Jy := n -> piecewise( n=1, Ja + I*Jb, n=-1, Ja - I*Jb, 0);
> mv := n -> piecewise( n=1, 2*M0/Pi, n=-1, 2*M0/Pi, 0);

> k(-1);

> tothxd(-1);

> F := -A * mu0 * ( tothxd(-1) * conjugate(tothzd(-1))
      + tothxd(1) * conjugate(tothzd(1)) );
> simplify(F);
> n1 := collect(",[Ja,Jb,M0,mu0,A]);
> n2 := Re(n1);
> n3 := evalc(n2);
> z1 :=collect(",[Ja,Jb,M0,mu0,A,cos(zeta*z0),sin(zeta*z0)]);
> z2 :=factor(z1);

> nz3 := numer(z2):
> dz3 := denom(z2):
> expand(dz3);
> factor(");
> simplify(");
> coeff(nz3,Ja);
> expand(");
> factor(");
> map(simplify,");
> z3 := evalc(z2);
> map(factor,");
> collect(",[exp(zeta*x0),exp(-zeta*x0)]);

> yeah := factor(z2);
> z3 := coeff(yeah,cos(zeta*z0));
> op(z3);
> z4 := op(7,z3);
> z5 := convert(z4,exp);
> z6 := simplify(z5);

> alphat := (exp(2*zeta*(x0+Gamma))+exp(2*zeta*Delta)-
            exp(2*zeta*(Delta+x0+Gamma))-1)/(exp(2*zeta*(Delta+x0+Gamma))-1);
```

```
> betat :=  (exp(2*zeta*Gamma)-1)/(exp(2*zeta*(Gamma+Delta+x0))-1);

> z7 := alphat * betat * z6;
> simplify(");
```

A.3.2 Normal Force

```
> Fx := -A * mu0 /2 * ( tothxd(-1) * conjugate(tothxd(-1)) +
        tothxd(1) * conjugate(tothxd(1)) - tothzd(-1) * conjugate(tothzd(-1))
        - tothzd(1) * conjugate(tothzd(1)) );
> frontend(expand,[Fx]);
> z1a :=collect(",[Ja, Jb]);
> z2a := evalc(Re(z1a));
```

Bibliography

[1] British Patent No. 12364, Jacquard and Electric Shuttle Company, 1895.

[2] Anorad Corporation, Hauppauge, NY. *Sine Hall Mode D.C. Servo Amplifier Model No. SMA8415-OC54-001-1A-1-00*, July 1997.

[3] Frank J. Bartos. 'Smart' motors: Ultimate motor-to-controller matching. *Control Engineering*, pages 36–44, December 1997.

[4] Michael Tekletsion Berhan. Implementation of a halbach array in a tubular linear motor. Master's thesis, Mechanical Engineering Dept., Massachusetts Institute of Technology, June 1996.

[5] Ben H. Carlisle. Simplifying gantry control with linear motors. *Machine Design*, pages 99–102, September 1988.

[6] Anwar Chitayat. Linear motor with non-magnetic armature. U. S. Pat. No. 4749921, 1988.

[7] Stephen Czajkowski, Gerhard Heinemann, Boaz Eidelberg, and Chris Stollberger. Linear motors: The future of high-performance machine tools. *American Machinist*, pages 44–48, September 1996.

[8] D. K. Edwards, V. E. Denny, and Anthony F. Mills. *Transfer Processes*. Hemisphere, Washington, DC, second edition, 1979.

[9] Boaz Eidelberg. Linear motors pass the ruggedness test. *Machine Design*, pages 69–71, August 1996.

[10] A. E. Fitzgerald, Jr. Charles Kingsley, and Stephen D. Umans. *Electric Machinery.* McGraw-Hill, Inc., New York, 1990.

[11] Gene F. Franklin, J. David Powell, and Michael Workman. *Digital Control of Dynamic Systems.* Addison-Wesley, Reading, Massachusetts, 1998.

[12] Gorman-Rupp Industries, Bellville, OH. *Magnetic Drive Centrifugal Pump 15650.*

[13] Klaus Halbach. Design of permanent multipole magnets with oriented rare earth cobalt material. *Nuclear Instruments and Methods*, 169:1–10, 1980.

[14] Klaus Halbach. Physical and optical properties of rare earth cobalt magnets. *Nuclear Instruments and Methods*, 187:109–117, 1981.

[15] Klaus Halbach. Application of permanent magnets in accelerators and electron storage rings. *Journal of Applied Physics*, 57(1):3605–3608, April 1985.

[16] Hermann A. Haus and James R. Melcher. *Electromagnetic Fields and Energy.* Prentice-Hall, Englewood Cliffs, New Jersey, 1989.

[17] André Heck. *Introduction to Maple.* Springer, New York, 1996.

[18] F. C. Incropera and D. P. DeWitt. *Fundamentals of Heat and Mass Transfer.* John Wiley & Sons, New York, third edition, 1990.

[19] MWS Wire Industries. Mws wire catalog, September 1996.

[20] Won jong Kim. *High-Precision Planar Magnetic Levitation.* PhD thesis, Electrical Engineering and Computer Science Dept., Massachusetts Institute of Technology, June 1997.

[21] O. N. Kostikov, E. I. Malykhin, Z. P. Us, and A. I. Yakovlev. Influence of internal heat transfer on the thermal state of totally enclosed low-power electric motors. *Soviet Electrical Engineering*, 50(9), 1979.

[22] Eric R. Laithwaite. *A History of Linear Electric Motors.* Macmillan, London, 1987.

[23] J. D. Livingston. *Driving Force—The Natural Magic of Magnets.* Harvard University Press, 1996.

[24] Robert M. McCoy. Environmental considerations. In Richard H. Engelmann and William M. Middendorf, editors, *Handbook of Electric Motors*, chapter 12. Marcel Dekker, Inc., New York, 1995.

[25] James R. Melcher. *Continuum Electromechanics.* The MIT Press, Cambridge, Massachusetts, 1981.

[26] Anthony F. Mills. *Basic Heat and Mass Transfer.* Irwin, Boston, Massachusetts, 1995.

[27] John Ofori-Tenkorang. *Permanent-Magnet Synchronous Motors and Associated Power Electronics for Direct-Drive Vehicle Propulsion.* PhD thesis, Electrical Engineering and Computer Science Dept., Massachusetts Institute of Technology, September 1996.

[28] Jose Americo Dias Pinto, Carlos F. Lemos Antunes, and A. Paulo Breda Coimbra. Transient heating and cooling analysis in an electromagnetic device. *IEEE Transactions of Magnetics*, 30(5), September 1994.

[29] Patrick Ponticel. A major machining breakthrough. *Automotive Engineering*, 105(5), May 1997.

[30] L. J. Rejda and Kris Neville. *Industrial Motor Users' Handbook of Insulation for Rewinds.* Elsevier Scientific Publishing Company, New York, 1977.

[31] Technology 80, Inc., Minneapolis, MN. *Model 5312B 4-Axis Quadrature Encoder—PC Technical Reference V1.1*, December 1995.

[32] S. Torquato and F. Lado. Bounds on the conductivity of a random array of cylinders. In *Proceedings of the Royal Society of London, Series A (Mathematical and Physical Sciences)*, volume 417, pages 59–80, May 1988.

[33] David L. Trumper, Won-jong Kim, and Mark E. Williams. Design and analysis framework for linear permanent-magnet machines. *IEEE Transactions on Industry Applications*, 32(2):371–379, March/April 1996.

[34] David L. Trumper, Mark E. Williams, and Tiep H. Nguyen. Magnet arrays for synchronous machines. In *Proceedings of the IEEE IAS 28th Annual Meeting*, pages 216–223, Toronto, Canada, October 1993.

[35] Waterloo Maple Inc. *Maple V Release 4*, 1996.

[36] Richard Waters. Linear motors no longer stuff of science fiction. *The Financial Post*, January 1997.

[37] Mark E. Williams. *Precision Six Degree of Freedom Magnetically-Levitated Photolithography Stage.* PhD thesis, Mechanical Engineering Dept., Massachusetts Institute of Technology, October 1997.